12-2006

A Kinetic Study of Indentation Pop-out in Si

Songqing Wen
University of Tennessee - Knoxville

To the Graduate Council:

I am submitting herewith a dissertation written by Songqing Wen entitled "A Kinetic Study of Indentation Pop-out in Si." I have examined the final electronic copy of this dissertation for form and content and recommend that it be accepted in partial fulfillment of the requirements for the degree of Doctor of Philosophy, with a major in Materials Science and Engineering.

George M. Pharr, Major Professor

We have read this dissertation and recommend its acceptance:

Hann Choo, David C. Joy, Claudia J. Rawn

Accepted for the Council:

Carolyn R. Hodges

Vice Provost and Dean of the Graduate School

(Original signatures are on file with official student records.)

To the Graduate Council:

I am submitting herewith a dissertation written by Songqing Wen entitled “A Kinetic Study of Indentation Pop-out in Si.” I have examined the final electronic copy of this dissertation for form and content and recommend that it be accepted in partial fulfillment of the requirements for the degree of Doctor of Philosophy, with a major in Materials Science and Engineering.

George M. Pharr
Major Professor

We have read this dissertation
and recommend its acceptance:

Hann Choo

David C. Joy

Claudia J Rawn

Accepted for the Council:

Linda Painter
Interim Dean of Graduate Studies

(Original signatures are on file with official student records.)

A KINETIC STUDY OF INDENTATION POP-OUT IN SI

A Dissertation

Presented for the

Doctor of Philosophy Degree

The University of Tennessee, Knoxville

Songqing Wen

December 2006

DEDICATION

To my parents, Jinlin Wen and Peiqin Yuan, for their unconditional love and support.

ACKNOWLEDGMENT

I would like to thank my advisor Prof. George M. Pharr, who I am so grateful to be able to study under his guidance, for given me this opportunity and his patience over the years. I would like to thank my committee (Prof. Hann Choo, Prof. David Joy, and Prof. Claudia Rawn). I am greatly indebted to the many people that I have worked with and benefited from through out the study. Foremost of them are, Dr. James Bentley at Oak Ridge National Laboratory who provided me with countless hours of help and advice on the cross-sectional TEM study, Dr. Jae-il Jang who had contributed significant amount of effort in this program during his postdoctoral research in our group, Dr. Ting Tusi at Texas Instruments for his generous help on the preparation of TEM cross-sections. I would also like to thank Dr. Warren Oliver at MTS Nano Instrument Inc, Dr. Michael Lance, Dr. Neal Evens, Dr. David Hoelzer, Dr. Andri Rar and Dr. Sohnhoon Shim at Oak Ridge National Lab. I am grateful to the faculty and staff in the Materials Science and Engineering Department at the University of Tennessee and my lab-mates Mike West, Jeremy Strader, James Lamanna, Caijun Su and Sangjoon Sohn for their help and friendship. Special gratitude goes to my best friends at the University of Tennessee, Gang Zuo, Haitao Xu and his wife Liang Ma, whose friendship made my studying life filled with joy. Finally, I would like to thank my sister Songyan Wen, and husband Jun Xu, for their love and support over the years.

This research was sponsored by the National Science Foundation under grant number DMR-0203552, and at the ORNL SHaRE User Facility by Office of Basic

Energy Sciences, U.S. Department of Energy, under Contract DE-AC05-00OR22725 with UT-Battelle, LLC.

ABSTRACT

The kinetics of the phenomenon of pop-out during nanoindentation of silicon were studied by a variety of mechanical and structural characterization techniques. Pop-out is commonly viewed to result from the reversal of a unique pressure-induced, volume reducing phase transformation that occurs in silicon and germanium.

The mechanical characteristics were examined by standard nanoindentation methods using a number of triangular pyramidal indenters with centerline-to-face angles varying in the range 35°-85°. The load at which pop-out occurs was systematically measured as a function of indenter angle, loading/unloading rate, and maximum load. Nanoindentation tests were conducted both at a constant loading rate and by step unloading to fixed percentages of the maximum load. In the step unload tests, the pop-out occurred after a delay time that was measured for periods up to 30 minutes. A limited number of elevated temperature tests were performed at 45°C to establish the temperature dependence of the rate controlling mechanism.

The phases that form during indentation were investigated by micro-Raman spectroscopy, cross-sectional transmission electron microscopy, and high resolution electron microscopy. It was found that the primary transformed phase after unloading at fast rates and low maximum loads is amorphous, with occasional observations of some Si-I (diamond cubic) embedded in the amorphous matrix. These structures correspond to no pop-out during unloading. At slower unloading rates and higher maximum loads, pop-out is observed, and the structure of the transformed material is a mixture of nanocrystalline phases including Si-XII (rhombohedral), Si-III (body centered cubic), and

Si-I (diamond cubic), along with some amorphous silicon. The volume of the transformed zone depends on the indenter angle, with the sharper indenters tending to produce smaller transformed volumes and extruded material.

A kinetic model was developed that accounts for most of the experimental observations based on the assumption that pop-out is a thermally activated process corresponding to the homogeneous nucleation of Si-XII from the high pressure Si-II phase (β-tin structure) followed by rapid growth of metastable nano-crystalline material. If the unloading rate is so fast that there is not enough time for the formation of a nucleus during the unloading period, the material transforms to amorphous via a structural frustration process. Comparison to experimental data shows that the model has reasonable qualitative and semi-quantitative predictive capabilities.

TABLE OF CONTENTS

I INTRODUCTION 1

1.1 PRESSURE INDUCED PHASE TRANSFORMATION IN SI UNDER HYDROSTATIC CONDITION 1

1.2 INDENTATION-INDUCED PHASE TRANSFORMATIONS IN SI BY NANOINDENTATION .. 6

1.2.1....Initial Evidence of Indentation-induced Phase Transformation in Si..... 6

1.2.2....Factors Affecting Indentation-induced Phase Transformation Behavior. 11

1.3 TEM OF INDENTATION-INDUCED PHASE TRANSFORMATIONS IN SI 15

1.3.1....TEM of Micro-hardness Indentations in Si..... 15

1.3.2....Plan-view TEM of Nanoidentations in Si..... 18

1.3.3....Cross-sectional TEM of Nanoindentations in Si..... 19

1.4 OBJECTIVES OF STUDY 31

II EXPERIMENTAL TECHNIQUES 34

2.1 NANOINDENTATION 34

2.2 SCANNING ELECTRON MICROSCOPY 37

2.3 RAMAN MICROSCOPY 37

2.4 TRANSMISSION ELECTRON MICROSCOPY (TEM) CHARACTERIZATION 38

2.4.1....TEM Sample Preparation – Focus Ion Beam (FIB) Milling 38

2.4.2....High Resolution Electron Microscopy (HREM) 39

III EXPERIMENTAL RESULTS AND DISCUSSIONS 42

3.1 GENERAL STUDY OF INDENTATION-INDUCED PHASE TRANSFORMATION IN SI 42

3.1.1....Indentation Load/Size Effects for the Berkovich Indenter 42

3.1.2....Indenter Angle Effects 43

3.1.2.1 Indenter Angle Effects at Low Peak Load 45

3.1.2.1.1 Cube-corner (35.3°) Indentation 49

3.1.2.1.2 45° Indentation 51

3.1.2.1.3 55° Indentation 53

3.1.2.1.4 Berkovich (65.3°) Indentation 53

3.1.2.1.5 75° Indentation 59

3.1.1.2 Indenter Angle Effects at High Load 59

3.1.2.2.1 Berkovich (65.3°) Indentation 64

3.1.2.2.2 Cube-corner (35.3°) Indentation 68

3.1.2.2.3 Extrusion by Sharp Indenters 70

3.1.3....Rate Effects at Low Load 73

3.2 A KINETIC STUDY OF INDENTATION POP-OUT USING THE BERKOVICH INDENTER. 80

3.2.1....Systematic Indentation Pop-out Study using the Berkovich Indenter 80

3.3.2....Temperature Effects on Indentation Pop-out using the Berkovich Indenter 84

3.2.3....Step Unload Indentation Using the Berkovich Indenter 86

IV INDENTATION POP-OUT MODELING 94

4.1 INDENTATION POP-OUT MODEL 94

4.1.1....Proposed Mechanism 94

4.1.2....Volume of the Transformed Zone 98

4.1.3....Critical Free Energy *100*

4.1.4....Rate of Attachment *102*

4.1.5....Nucleation Rate *105*

4.1.6....Pop-out at Underpressurization Δp *106*

4.2 INTERFACIAL ENERGY AND ACTIVATION ENERGY 109

4.2.1....Estimating Interfacial Energy and Activation Energy γ and Q *109*

4.2.2....Sensitivity of the Estimated Interfacial Energy and Activation Energy γ and Q to the Equilibrium Pressure p_e *111*

4.2.3....Sensitivity of the Estimated Interfacial Energy and Activation Energy γ and Q vs. Unloading Rate *111*

4.3 MODEL EVALUATION 113

4.3.1....Modeling the Influences of Indentation Rate and Peak Load *113*

4.3.2....Modeling Temperature Effects *113*

4.3.3....Modeling the Step Unload Tests *117*

4.3.4.... Modeling the Indenter Angle Effect *120*

V CONCLUSIONS 123

REFERENCES 125

VITA 130

LIST OF TABLES

TABLE 1- 1 STRUCTURAL DATA FOR SOME CRYSTALLINE PHASES OF SI[14]..... 3
TABLE 1- 2 SUMMARY OF TEM OBSERVATIONS BY SAKA ET AL.[49]. 32
TABLE 2- 1 GEOMETRY CONVERSION DATA FOR THE PYRAMIDAL INDENTERS USED IN THE STUDY. 36
TABLE 3- 1 SUMMARY OF RESULTS OF SYSTEMATIC INDENTATION TEST WITH THE BERKOVICH INDENTER. 81
TABLE 3- 2 MEAN POP-LOAD FOR VARIOUS UNLOADING RATE AT 25°C AND 45°C. 85
TABLE 3- 3 SUMMARY OF THE 30 MN PEAK LOAD STEP UNLOAD TESTS. 93
TABLE 3- 4 SUMMARY OF THE 100 MN PEAK LOAD STEP UNLOAD TESTS. 93
TABLE 4- 1 ESTIMATED INTERFACIAL ENERGY AND ACTIVATION ENERGY γ AND Q FOR VARIOUS P_E..... 112
TABLE 4- 2 ESTIMATED INTERFACIAL ENERGY AND ACTIVATION ENERGY γ AND Q USING DATA OF VARIOUS LOADING RATES. 112
TABLE 4- 3 AMOUNT OF UNDERPRESSURIZATION ΔP CORRESPONDING TO UNLOAD PERCENTAGE FROM 100 MN AND 30 MN PEAK LOADS..... 118
TABLE 4- 4 MODEL PREDICTION OF INDENTER ANGLE EFFECTS AT 10 MN PEAK LOAD. 122

LIST OF FIGURES

Figure 1. 1 Free energy of Si in the relaxed *r*8, *bc8*, *st*12, cubic diamond, and ß-tin phases as a function of reduced volume. The dashed common tangent line shows that the stable phases are Si-I and Si-II; Si-XII, Si-III, and Si-IX have a slightly higher enthalpy and are thus metastable.[7]..... 4

Figure 1. 2 Relative volume in units of the experimental zero-pressure volume of the cubic diamond Si-I of the high-pressure Si phases as a function of pressure. Experimental points are from Reference [26] (Si-I and Si-II) and Reference [20] (Si-III and Si-XII). Filled and open circles correspond to increasing and decreasing pressure, respectively. The solid lines are fits to the 3rd order Birch equation of state [28; 29] with the values of bulk modulus B0 = 108 GPa and its first pressure derivative B0' = 4 for Si-I; B0 = 117 GPa for Si-III, and B0 = 108 GPa for Si-XII with B0' fixed at 5. Dashed line serves as a guide to the eye. [8]..... 5

Figure 1. 3 Simulated unit cells of various Si structures: (a) cubic diamond Si-I; (b) hexagonal diamond Si-IV; (c) body-centered cubic Si-III and (d) rhombohedral Si-XII. 7

Figure 1. 4 Cyclic indentation Load - Displacement (P-h) curves for (a) high load condition and (b) low load condition[23]. 9

Figure 1. 5 Acoustic emission and electrical resistance measurement during nanoindentation with a Berkovich indenter showing no acoustic emission detected upon discontinuity (pop-out) [27]..... 10

Figure 1. 6 SEM observation of extrusion around hardness imprint[24]. 12

Figure 1. 7 Scheme of the phase transformations that occur during hardness indentations and post-treatment in Si. During the indentation experiment Si transforms from the original diamond cubic Si-I structure to the hexagonal diamond Si-IV or the metallic b-Sn phase Si-II depending on local stress conditions. Upon unloading other polymorphs form, including the amorphous phase, Si-XII and Si-III. During annealing there is a transition to Si-IV or, and at higher temperatures, to Si-I.[28]..... 12

Figure 1. 8 Typical nanoindentation P-h curves at 50 mN peak load[30]..... 13

Figure 1. 9 Corresponding Raman spectra of the nanoidentations in Figure 1. 8 showing the correlation between pop-out event and phases presentation[30]. 14

Figure 1. 10 (a) BF TEM image of an indentation impression in an ion-thinned sample, (b) SAD of the interface between [110] Si and a-Si, (c) A typical HRTEM image of part A marked in (a), showing the uneven interface, the microtwins at the interface, and the clusters which consist of distorted lattice in the a-Si region [37]..... 17

Figure 1. 11 Dark field TEM images from the boxed reflections [200] of Si-III and [010] of Si-XII and the selected area electron diffraction patterns of (a) Si-III (bc8) and (b) Si-XII (r8) in the nanoindentation on a (001) Si wafer [40]. 20

Figure 1. 12 (a) DF XTEM of a spherical indentation in Si made at P_{max} of 20 mN, (b) SAD pattern of the polycrystalline region. All the unboxed reflections are from the Si-XII. Note that the DF image was taken with the indicated spot in (b)[42]. 22
Figure 1. 13 (a) BF XTEM of a spherical indentation (4.2 μm radius) in Si made at Pmax of 80 mN, (b) SAD pattern of the a-Si taken from region 1 in (a) (directly under the residual imprint), (c) SAD taken from region 2[42]..... 23
Figure 1. 14 XTEM bright-field images of indentations in Si made using a Berkovich indenter with a maximum load of 250 mN and a continuous load–unload cycle. Indents were made using (a) a single step and (b) 25 steps[42]. 25
Figure 1. 15 Cross-sectional views of indentation-induced deformation in the subsurfaces of Si specimens after complete unloading. (a) 30 mN, (b) 70 mN, and(c) 90 mN. Note the Si-III particles with lighter colors, highlighted by the dotted white curves in (b) [45]. 26
Figure 1. 16 Crystalline phase in the transformed zone after indentation with a spherical indenter, (a) P_{max} = 90 mN, (b) P_{max} = 50 mN, (c) P_{max} = 30 mN [44]. 27
Figure 1. 17 Microstructure of the transformation zone with different *P*max and average loading rate of 3 mN/s (diffraction patterns of the transformation zones are inserted), (a) a dark-field TEM image taken from the P_{max} = 30 mN specimen, (b) a bright-field TEM image taken from the P_{max} = 90 mN specimen [47]. 29
Figure 1. 18 Indent in Si: (a) bright-field image, (b) selected-area diffraction pattern from the transformed zone, (c) bright-field image showing the region around the base of the transformed zone (arrows indicate the slip bands), (d) 111 dark-field image showing a dislocation network associated with the crack [48]. 30

Figure 2. 1 Schematic of Nanoindenter. 35
Figure 2. 2 Geometry of Nanoindenters. 35
Figure 2. 3 TEM sample preparation procedure. 40
Figure 2. 4 TEM cross-section preparation. 41

Figure 3. 1 Berkovich indentations at 10, 30, 50 and 100 mN at 5 mN/s. 44
Figure 3. 2 Typical indentation P-h curves for Pmax of 13 mN at 5 mN/s. 46
Figure 3. 3 SEM plan-view and TEM cross-sectional images of low load indentations (10 mN) made with various triangular pyramidal indenters. 47
Figure 3. 4 The transformed zone shape schematic outlined approximately in the shape of an apex of 90° for 65° to 35° indentations. 48
Figure 3. 5 (a) BF image of the cube-corner indentation, (b) SAD taken from bottom of the indentation cross-section. Pmax = 10 mN, rate = 5 mN/s. Note the circle in the BF image indicated the position of the aperture at where the SAD is obtained. 50
Figure 3. 6 (a) BF image of the 45° indentation made at Pmax = 10 mN, rate = 5 mN/s, ... 52

Figure 3. 7 BF (a) and DF (b) image of the 45° indentation made at Pmax = 10 mN at rate of 5 mN/s. Note that the DF image is taken with the boxed reflection in the SAD insert in (b). 52
Figure 3. 8 (a) BF image of the 55° indentation made to peak load of Pmax = 10 mN at 5 mN/s, (b) SAD insert taken from the outlined circle in (a)..... 54
Figure 3. 9 HREM images taken in the transformed zone of the 55° indentation made at peak load of 10 mN at 5 mN/s. 55
Figure 3. 10 Cross-sectional TEM of the low load (10 mN, 5 mN/s) Berkovich indent: (a) bright field image, (b) dark field image from a Si-I (111) reflection, (c) SAD from the transformed zone. 56
Figure 3. 11 High resolution TEM of a low-load (10 mN) Berkovich indent: (a) bright field TEM image, (b) microtwins at the crystalline-to-amorphous boundary, (c) crystallization in the amorphous transformed zone induced by the electron beam. 58
Figure 3. 12 BF image of the 75° indentation made to peak load of Pmax = 10 mN at 5 mN/s, and SAD insert taken over the transformed zone. 60
Figure 3. 13 WBDF image of the 75° indentation made to peak load of Pmax = 10 mN at 5 mN/s that produces the diffraction contrast of the dislocations that reside outside the transformed zone. 60
Figure 3. 14 (a) Typical P-h curves and, (b) Raman spectra, of high peak load (80 mN) indentations made with various indenters at the fixed 5 mN/s rate 61
Figure 3. 15 SEM plan-view and TEM cross-sectional images of high load (80 mN) indentations (80 mN): (a) and (b) Berkovich indentation, (c) and (d) cube-corner indentation. 63
Figure 3. 16 BF TEM image of the 80 mN Berkovich with inserted SAD obtained from the transformed region. 65
Figure 3. 17 BF TEM image (a) of the left side of the Berkovich 80 mN sample with SAD over the transformed zone inserted, (b) ~ (d) DF TEM images obtained from the labeled reflections in the SAD in Figure 3. 16. 66
Figure 3. 18 Cube-corner indentation made at 80 mN and 5 mN/s. (a) BF TEM image serves as map for the cross-section, (b) Boxed A in (a), the extrusion on the left side of the cross-section and SADs taken from the circled areas, (c) Box B in (a), BF and DF formed by Si-I reflection of the median crack, (d) Box C in (a), extruded material on the right side of the cross-section. 69
Figure 3. 19 Cube-corner (35°) indentation made at 80 mN at 5 mN/s (a). Plan-view SEM showing the extruded material, (b). Ramam spectrum indicates the presence of a-Si, Si-III and Si-XII in the indented region. Note that the Si-I peak is mostly from the pristine Si, (c). Ramam map constructed using a-Si peak showing the a-Si resides at where the extrusion being observed (light area around the indentation), (d). Ramam map constructed using Si-III and Si-XII peaks showing Si-III and Si-XII mostly exist within the indentation (high lighted area in the center). 71
Figure 3. 20 Schematic of extrusion by cube-corner indenter..... 72
Figure 3. 21 Typical P-h curves of 10 mN peak load indentations made with varies indenters at the fixed 0.5 mN/s rate 74

Figure 3. 22 Typical P-h curves of 10 mN peak load indentations made with varies indenters at the fixed 0.05 mN/s rate 74
Figure 3. 23 BF, DF and SAD of the 10 mN Berkovich indentation made at 0.05 mN/s did not show pop-out. 76
Figure 3. 24 BF, DF and SAD of the 10 mN Berkovich indentation made at 0.05 mN/s show pop-out. 77
Figure 3. 25 Indentation P-h curve, BF and DF TEM images for (a) 10 mN Berkovich indentation made at 5 mN/s, (b) 10 mN Berkovich indentation made at 0.05 mN/s and did not show pop-out, (c) 10 mN Berkovich indentation made at 0.05 mN/s and did show pop-out. 79
Figure 3. 26 Maximum pop-out load vs. indentation peak load. 82
Figure 3. 27 Mean Pop-out load as vs. indentation unloading rate. 83
Figure 3. 28 Schematic of the loading history during step unload indentation. 87
Figure 3. 29 Displacement change over waiting time during step unload tests from 30 mN peak loads at various percentage unload: (a) 25%, (b) 50%, (c) 75% and (d) 90% 88
Figure 3. 30 Displacement change over waiting time during step unload test from 100 mN peak loads at various percentage unload: (a) 30%, (b) 50%, (c) 75% and (d) 85%. 90

Figure 4. 1 Proposed mechanism for modeling indentation pop-out in Si. 95
Figure 4. 2 Illustration of critical nucleation within the transformed zone. 97
Figure 4. 3 Schematic of the geometry of transformed zone relative to the indenter tip angle. 99
Figure 4. 4 Volume free energy as a function of pressure for Si-II and Si-XII system. 101
Figure 4. 5 Illustration of atoms attaching to the critical nucleus. 103
Figure 4. 6 Schematic of proportionality assumption for (a) load and (b) pressure as a function of time during indentation. 108
Figure 4. 7 Comparison the predicted pop-out load vs. peak load (Pmax) using the mechanistically-based model and experimental indentation data. 114
Figure 4. 8 Model predicted pop-out vs. loading/unloading rate ($\dot{P}$) using the mechanistically-based model and experimental indentation data. 115
Figure 4. 9 Model predicted pop-out loads as a function of temperature and the experimental indentation data at 25°C and 45°C. 116
Figure 4. 10 Nucleation rates for 100 mN and 30 mN peak loads at different percentage step unload. The dots represent data point of all the pop-out indentations from the step unload tests and dashed and solid lines represent predictions using the model for 100 mN and 30 mN peak load. The number on the plot designated the number of indentations that pop-out instantaneously followed the step unload. 119
Figure 4. 11 Model prediction of the indenter angle effects on pop-out loads for peak loads ranging from 5 mN to 100 mN. 121

I Introduction

Si is an important structural semiconductor used extensively in the microelectronic and laser optics. It is well known that under pressure, Si undergoes a transformation from the normal diamond cubic structure to the denser beta-tin metallic phase under hydrostatic (and shear) stress, and that a subsequent reverse transformation to other phases can occur during the release of the pressure.

Nanoindentation has been shown to be a simple and effective tool for studying the pressure-induced phase transformation phenomena in Si. During indentation, the high stresses and strains can cause not only dislocation activity but also phase transformation. Following indentation, several experimental methods have been applied to characterize the microstructure of the transformed zone as well as the deformation behavior. Such methods include analyses of indentation load-displacement (P-h) curves, electrical conductivity measurement, acoustic measurement, and direct observation of the indentations using SEM, Raman spectroscopy, plan-view TEM and cross-sectional TEM. The purpose of studying the indentation-induced phase transformations is both to resolve scientific curiosity and to facilitate precision machining of these important semiconductors during fabrication.

1.1 Pressure Induced Phase Transformation in Si under Hydrostatic Condition

By coupling diamond anvil cell (DAC) experiments with diffraction, the transformation sequence of Si under hydrostatic pressure has been well defined. At

atmospheric pressure and temperature, Si has the cubic diamond structure, called Si-I (space group Fd3m), up to the melting temperature [1]. Pressurization experiments indicate that under hydrostatic conditions, Si-I transforms to Si-II (β-tin structure, space group I41 /amd) in the pressure range of 9 to 16 GPa [2-5]. This is a non-reversible transition, i.e., releasing pressure from the β-tin Si-II will not result in recovery of the diamond cubic Si-I. Instead, during pressure release, Si-II transforms to several other denser metastable phases depending on pressure release rate. For slow decompression, the first phase to form is Si-XII (rhombohedral structure with 8 atoms per unit cell, r8, space group R3) at pressure range of 12-9.4 GPa [6-8]. Further pressure release gradually diminishes the degree of rhombohedral distortion, producing a mixture of Si-XII and Si-III (body-centered cubic structure with 8 atoms per unit cell, space group Ia3) at about 2 GPa [6]. The Si-XII can persist to ambient pressure, although it will be only a minor component. The Si-XII to Si-III transition is fully reversible; repeating compression to 2.5 GPa results in complete Si-III transformation to Si-XII [6]. The structural forms for these crystalline phases of Si are tabulated in Table 1- 1, and the free energy of the relaxed form of the phases as a function of reduced volume is depicted in Figure 1. 1.

The relative volumes of the crystalline phases of Si as functions of pressure are summarized in Figure 1. 2. Note that the volume shown in the Figure 1. 2 is in units of the experimental zero-pressure volume of the cubic diamond Si-I. Si- II is approximately 20% denser than Si-I [3,4,9]. The equilibrium bc8 Si-III structure is determined to be ~9% denser than Si-I [10-12], and ~2% less dense than the r8 Si-XII [7,13]. Therefore, during slow

Table 1- 1 Structural data for some crystalline phases of Si[14].

Designation	Structure	Space group	Pressure region(GPa)	Lattice parameter(Å)
Si-I	Diamond cubic	Fd3m (227)	0-12.5	a=5.42
Si-II	Body centered Tetragonal (β-Sn)	I41/amd (141)	8.8-16	a=4.690 c=2.578
Si-III	Body centered cubic (bc8)	Ia 3 (206)	2.1-0	a=6.64
Si-XII	Rhombohedral/trigonal (r8)	R 3 (148)	12-2.0	a=5.712 α=109.99°

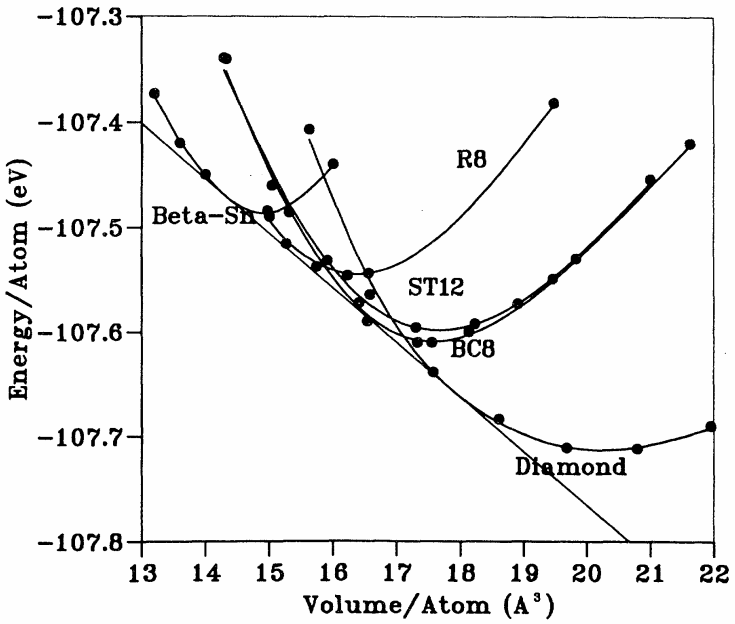

Figure 1. 1 Free energy of Si in the relaxed *r*8, *bc8*, *st*12, cubic diamond, and ß-tin phases as a function of reduced volume. The dashed common tangent line shows that the stable phases are Si-I and Si-II; Si-XII, Si-III, and Si-IX have a slightly higher enthalpy and are thus metastable.[7].

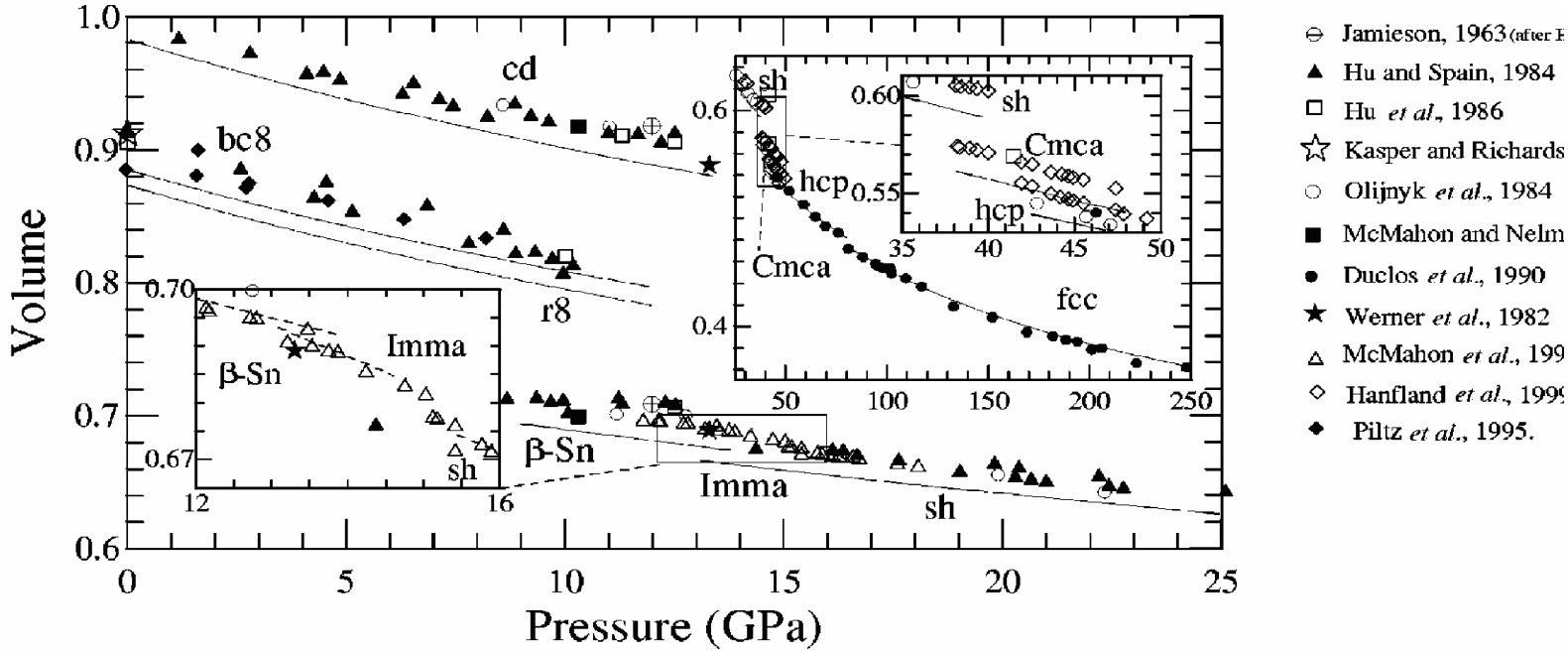

Figure 1. 2 Relative volume in units of the experimental zero-pressure volume of the cubic diamond Si-I of the high-pressure Si phases as a function of pressure. Experimental points are from Reference [26] (Si-I and Si-II) and Reference [20] (Si-III and Si-XII). Filled and open circles correspond to increasing and decreasing pressure, respectively. The solid lines are fits to the 3rd order Birch equation of state [28; 29] with the values of bulk modulus B0 = 108 GPa and its first pressure derivative B0' = 4 for Si-I; B0 = 117 GPa for Si-III, and B0 = 108 GPa for Si-XII with B0' fixed at 5. Dashed line serves as a guide to the eye. [8]

.

decompression, Si-II will transform to Si-XII with a volume expansion of ~9%, and then a further ~2% volume recovery occurs during the gradual Si- XII to Si-III transformation at lower pressure. A three dimensional (3D) representation of the unit cells of the Si-I, Si-III and Si-XII is shown in Figure 1. 3.

Compared to the understanding of pressure-induced behavior of the crystalline Si phases, the high-pressure properties of amorphous Si are far less understood. Measured with Raman spectroscopy, it is reported that there is a direct transition from cubic diamond Si-I to a high density amorphous (HDA) at pressure of 7~8 GPa in porous Si, and the HDA structure can transform to a low-density amorphous (LDA) upon decompression [15]. Such an amorphous-amorphous transition is related to a new concept of polyamorphism (the possibility of many distinct amorphous conformations for a given material). Durandurdu and Drabold calculated that pressure induced crystallization of amorphous Si (a-Si) initiates at 2.5 GPa and there is a first order amorphous to amorphous phase transition, at 9 GPa [16]. In addition, pressure-induced high density amorphization may take place in cubic diamond Si at approximately 15 GPa according to theoretical estimates by Durandursu and Drabold [16].

1.2 Indentation-induced Phase Transformations in Si by Nanoindentation

1.2.1 Initial Evidence of Indentation-induced Phase Transformation in Si

The possibility of indentation-induced phase transitions in Si was first suggested by Gridneva *et al.* in 1972 [17], and later by Gerk and Tabor [18], who pointed out the

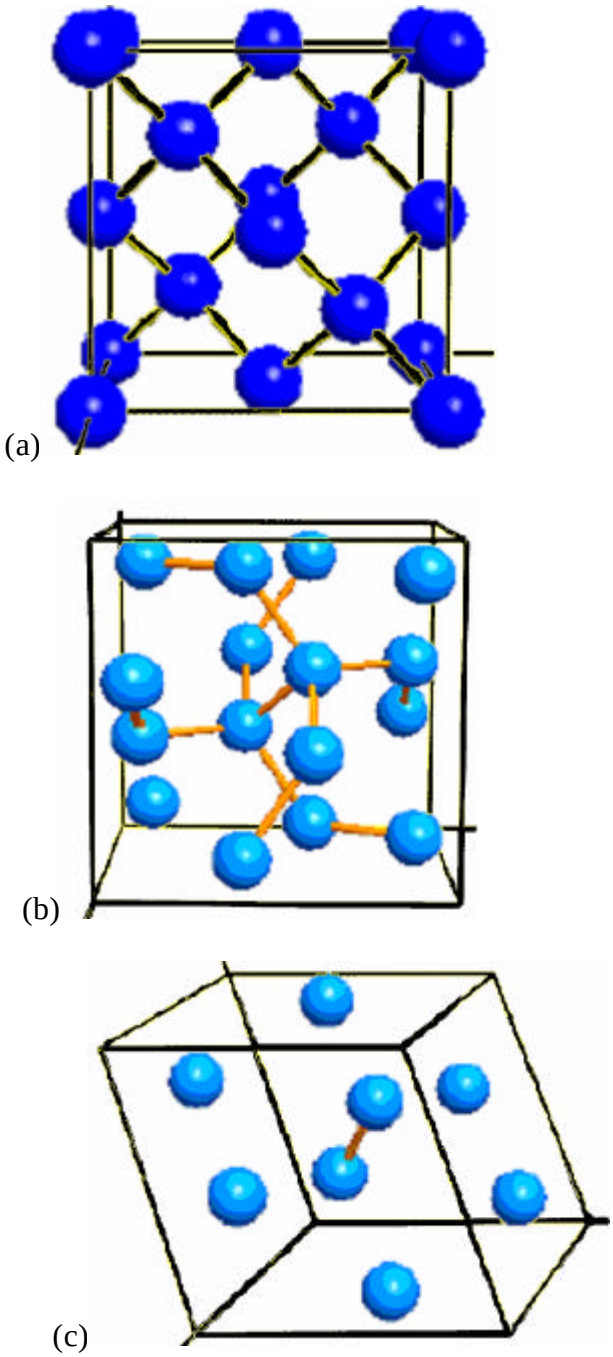

Figure 1. 3 Simulated unit cells of various Si structures: (a) cubic diamond Si-I; (b) body-centered cubic Si-III and (c) rhombohedral Si-XII.

similarity between the room-temperature Si hardness and the transformation pressure from Si-I to Si-II acquired in high-pressure cell experiments. They suggested that a pressure-induced metallization occurs in semiconductors with the diamond cubic structure during indentation tests, and that the phase transformation pressure determines the indentation hardness. Electrical conductivity measurements on Si wafers subjected to Vickers indentation showed a decrease in electrical resistance of the material beneath the indenter, which was attributed to the formation of a thin metallic layer between the indenter and the specimen [17]. Similar work conducted by other groups yielded a range of pressure from 8 to 12 GPa for the Si-I to Si-II transformation [19,20]. The variation in pressure in indentation tests could be attributed to the higher degree of deviatoric loading when uniaxial pressure is applied along the [111] direction, which according to Gilman facilitates the transformation [21]. After the pioneering work of Pethica [22], Pharr *et al.* first utilized the depth sensing indentation (nanoindentation) to study Si, which made it possible to investigate the mechanical response during the entire sequence of loading and unloading. They showed that the transformation to the electrically conductive form of Si occurs instantaneously during loading and unloading. A unique discontinuity in the load-displacement (P-h) curve which is commonly referred to as the pop-out event occurs when the peak load level is high (Figure 1. 4a), but the event is absent at low peak loads (Figure 1. 4b) [23-26]. From in-situ resistance measurements, the pop-out event was found to correspond to the drop in electrical conductivity during unloading, which was confirmed by Mann et al., who also found that there is no acoustic emission upon pop-out (discontinuity) during unloading (Figure 1. 5) [27]. Pharr et al. also observed extrusion of

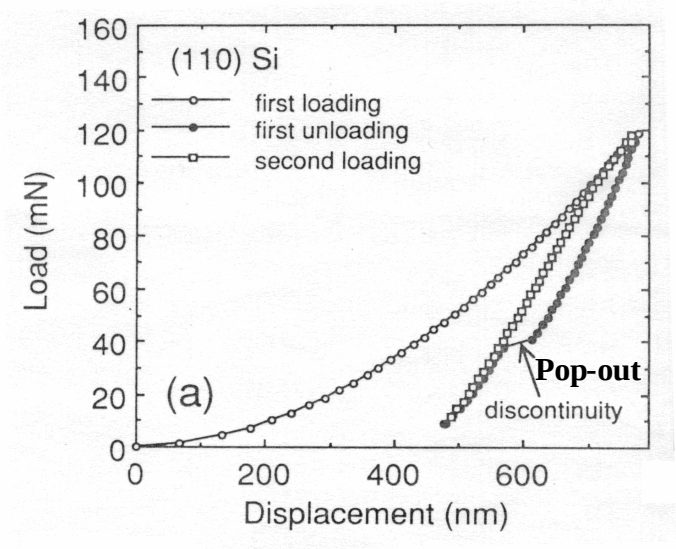

(a)

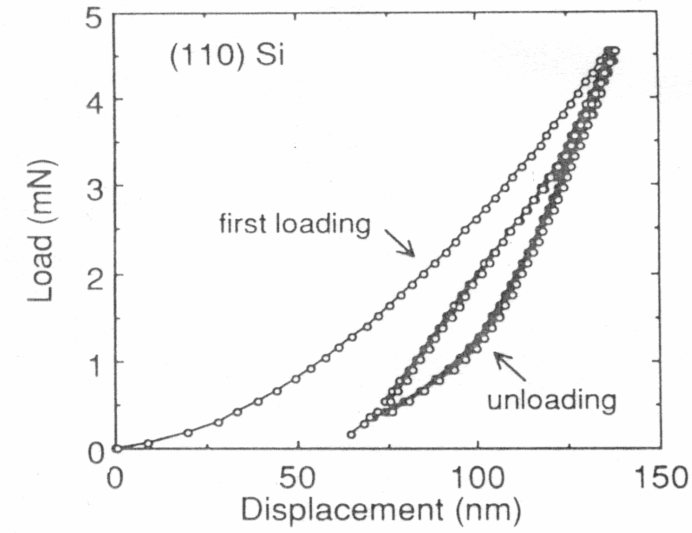

(b)

Figure 1. 4 Cyclic indentation Load - Displacement (P-h) curves for (a) high load condition and (b) low load condition[23].

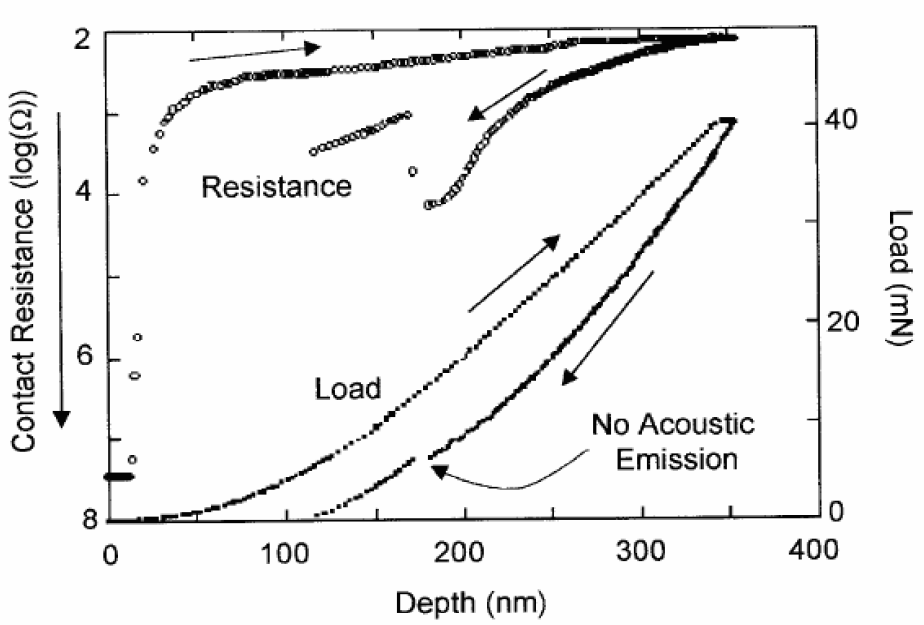

Figure 1. 5 Acoustic emission and electrical resistance measurement during nanoindentation with a Berkovich indenter showing no acoustic emission detected upon discontinuity (pop-out) [27].

material around the hardness imprint by SEM observation in Figure 1. 6, which is other evidence of the ductile nature of the transformed material [24].

In addition, indentations made with Vickers and Rockwell indentations were also studied by post-indentation Raman spectroscopy and TEM. The results, which provides evidence of Si phase transformations, will be discussed in detail in later sections.

1.2.2 Factors Affecting Indentation-induced Phase Transformation Behavior

Using Raman spectroscopy to study Vickers and Rockwell indentations, Kailer *et al.* indented a single crystal Si (100) wafer at unloading rates ranging from 0.001 mm/min to 100 mm/min [28]. They summarized the rate effects on indentation-induced phase transformation as shown in Figure 1. 7. Fast unloading rates promote the transformation from Si-II to the amorphous state, whereas slow unloading rates produce a mixture of the r8 high pressure polymorph Si-XII and the bc8 phase Si-III, in agreement with Mann [27,29]. The proposed phase transformation sequence is generally accepted, and it is similar to that of the DAC results.

Later, Domnich and Gogotsi successfully took advantage of nanoindentation and micro-Raman spectroscopy to show the strong correlation between the shape of the load-displacement (P-h) curve and the phase transformations occurring during nanoindentations made by Berkovich indenters. They categorized the P-h curves into three types: pop-out (discontinuity), elbow, and elbow plus pop-out [30-32]. The typical indentation P-h curves and the correlated Raman spectra are shown in Figure 1. 8 and Figure 1. 9. Figure 1. 8a depicts the characteristics of a typical pop-out on the unloading

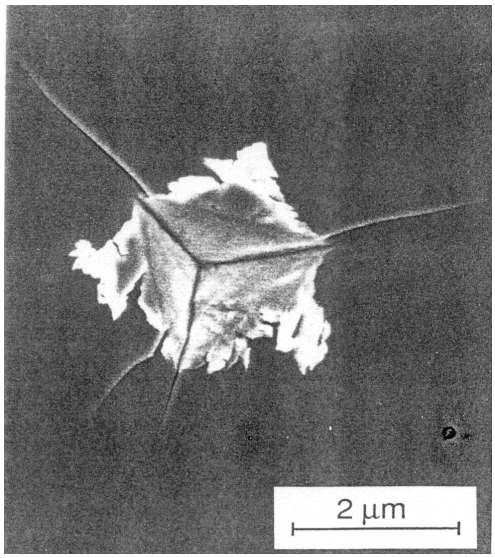

Figure 1. 6 SEM observation of extrusion around hardness imprint[24].

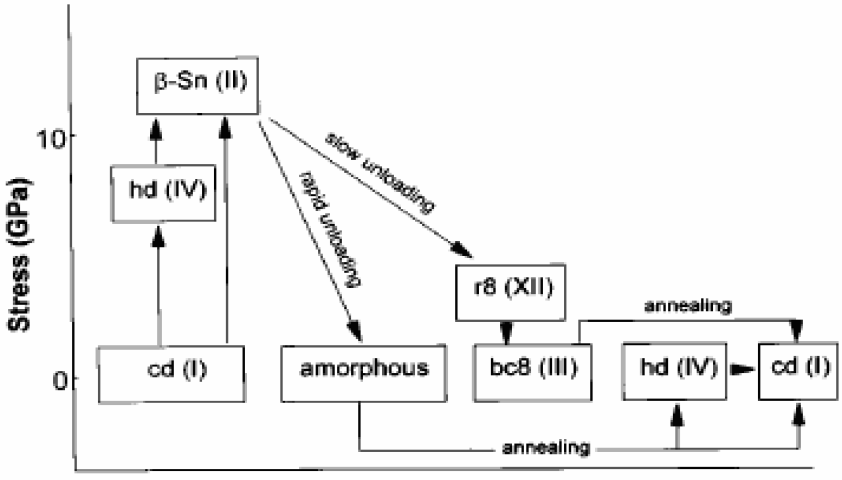

Figure 1. 7 Scheme of the phase transformations that occur during hardness indentations and post-treatment in Si. During the indentation experiment Si transforms from the original diamond cubic Si-I structure to the hexagonal diamond Si-IV or the metallic ь-Sn phase Si-II depending on local stress conditions. Upon unloading other polymorphs form, including the amorphous phase, Si-XII and Si-III. During annealing there is a transition to Si-IV or, and at higher temperatures, to Si-I.[28].

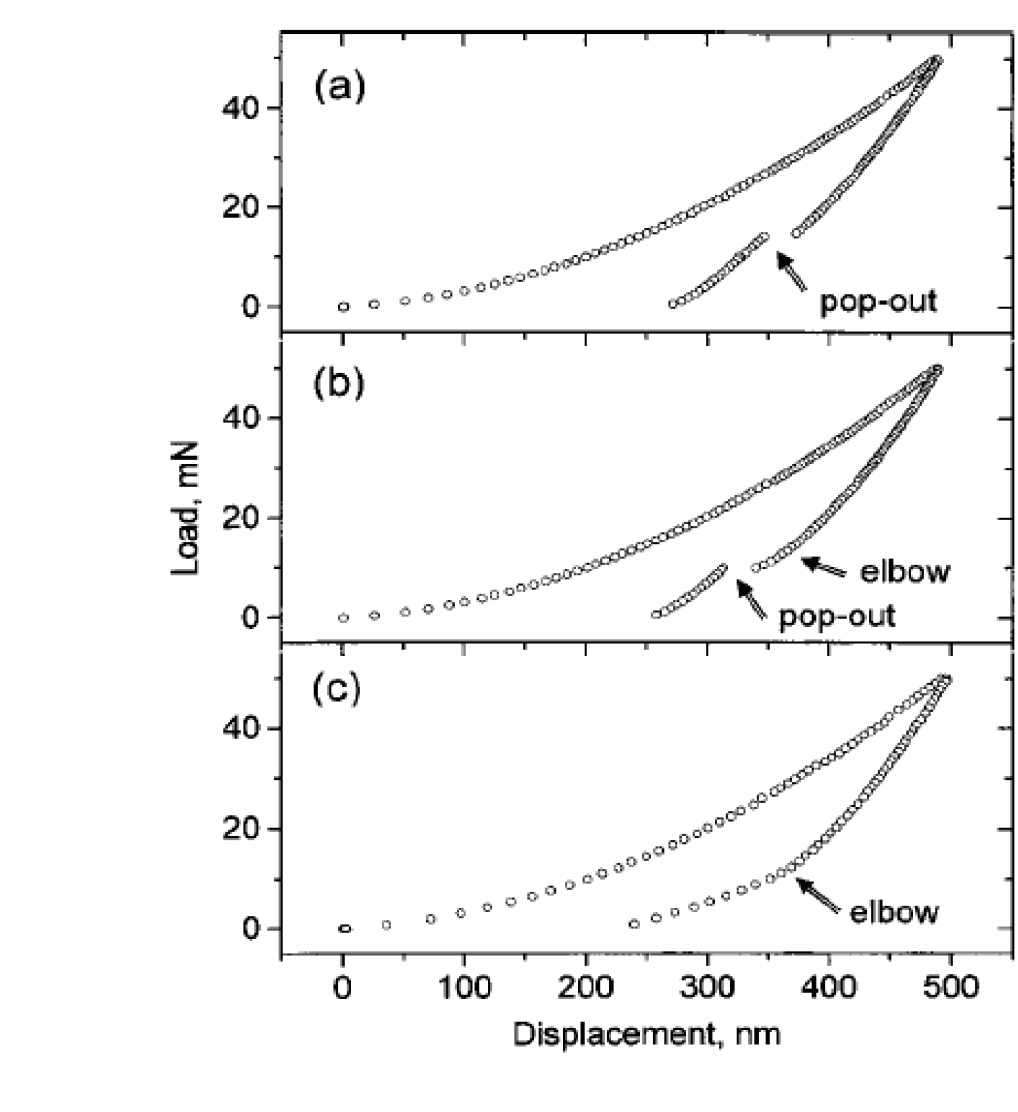

Figure 1. 8 Typical nanoindentation P-h curves at 50 mN peak load[30].

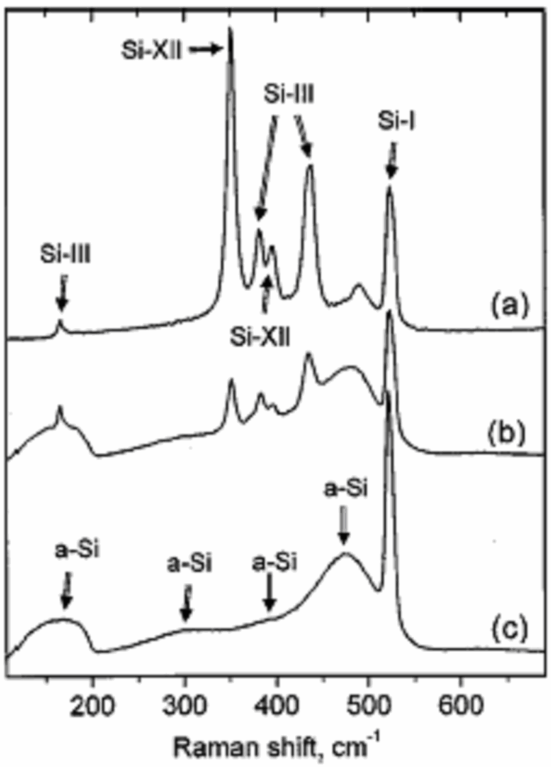

Figure 1. 9 Corresponding Raman spectra of the nanoidentations in Figure 1. 8 showing the correlation between pop-out event and phases presentation[30].

portion, which is believed to indicate a large volume change that occurs during the transformation from Si-II to the less dense metastable phases, Si-XII and Si-III.

The spectrum corresponding to this kind of indentation behavior is shown in Figure 1. 9a. The signature peaks of crystalline Si-III and Si-XII are labeled on the spectrum. In some cases, the curve showed a mixed response during unloading, producing Raman spectra of both a-Si and the metastable Si-III and Si-XII (Figure 1. 8b). A spectrum from indentation showing only the elbow behavior (Figure 1. 8c) on the unloading portion reveals only amorphous Si. Domnich and Gogotsi also reported that high peak loads (50 mN) lead to pop-out (crystalline formation) and low loads (30 mN) produce elbow (amorphization) at unloading rates of 1-3m N/s. This same trend was pointed out by Mann [27,29] and Busher *et al.* [33]. All these authors only characterized Berkovich indentations at a limited unloading rate range. A more intensive indentation study involving various indenter geometries and wider range of indentation testing parameters like that reported in this dissertation, can lead to a better understanding of indentation-induced phase transformation in Si.

1.3 TEM of Indentation-induced Phase Transformations in Si

1.3.1 TEM of Micro-hardness Indentations in Si

TEM of Si indentation dates back to Hill and Rowcliffe [34], who reported plastic deformation in indentations and some dislocation loops and slip bands but not phase transformation. After that, observations regarding phase transformations were made on micro hardness impressions in the late 1980's and early 1990's.

Clarke *et al.* observed Vickers and Knoop microindentations in Si with plan-view TEM samples [35]. They noted that regardless of different crystalline orientations, variation of maximum load, or use of two different tip shapes adopted in the indentation tests, there was little difference behavior observations. In general, a characteristic halo ring pattern of a-Si was always formed at the center of the hardness imprints. The authors suggested two possible ways in which the amorphous Si might have formed. One is a structural frustration kinetic argument, which applies to the case of a relatively rapid unloading rate and non-hydrostatic constraint of shear stress. The basic idea is that under these conditions, the high-pressure tetragonal phase (Si-II) does not have enough time to transform back to cubic diamond Si-I, and it instead transforms to a amorphous Si form. The other argument is based on direct pressure induced equilibrium amorphization during loading. This is facilitated by the fact that during indentation, the local pressure exceeds the metastable extension of the liquidus on the P-T diagram and, therefore, Si-I can transform directly to an amorphous (liquid-like) form which can persist during unloading due to insufficient activation energy to recover back to the diamond cubic structure. We note here that the shear stress component within the indented area is reportedly capable of facilitating amorphization by producing a high degree of local shear strain [21].

Wu et al. extracted cross-sections of Vickers indentations and founda-Si. They proposed that lattice distortion induces amorphization of Si under the stress, especially at highly stressed locations. They observed amorphous-crystalline (a-c) boundaries with uneven interfaces, microtwins at the interface, and the clusters which consist of distorted lattice in the *a*-Si region. These regions are depicted in Figure 1. 10 [36,37]. The authors did not report on how indenter shape, indentation rate and peak load affect the transformation.

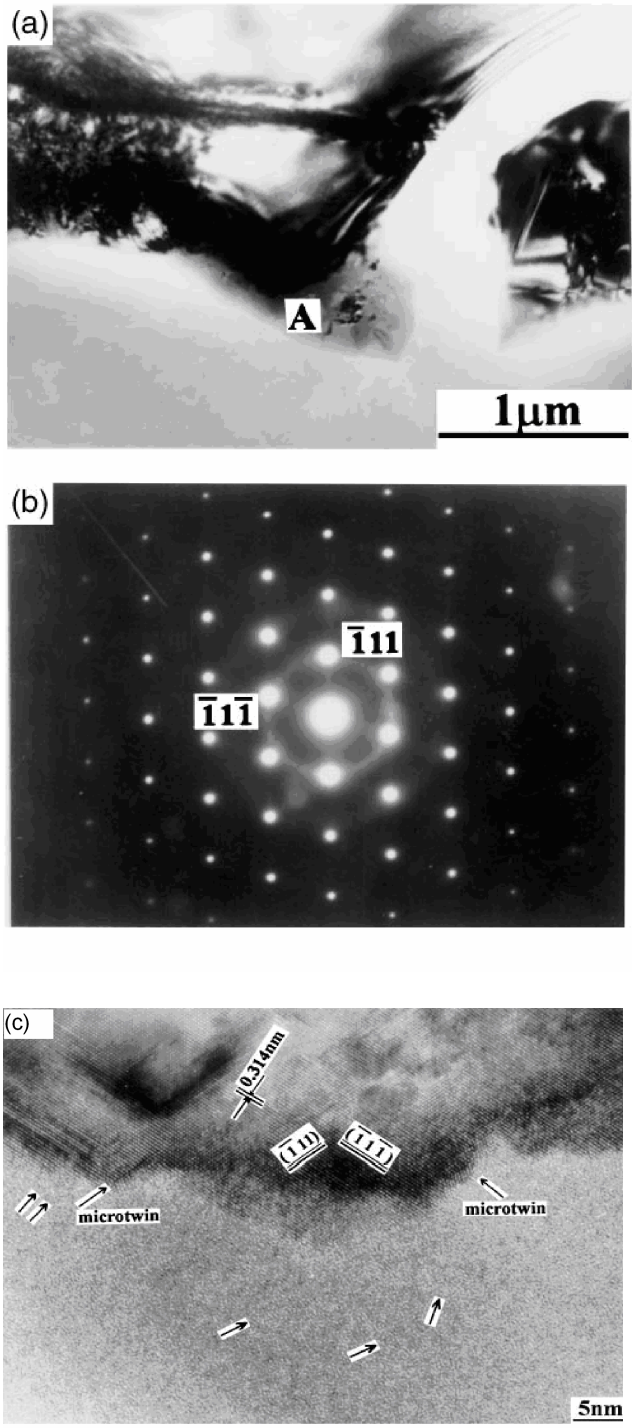

Figure 1. 10 (a) BF TEM image of an indentation impression in an ion-thinned sample, (b) SAD of the interface between [110] Si and a-Si, (c) A typical HRTEM image of part A marked in (a), showing the uneven interface, the microtwins at the interface, and the clusters which consist of distorted lattice in the a-Si region [37].

1.3.2 Plan-view TEM of Nanoidentations in Si

Page *et al.* conducted the first extensive TEM plan-view study on nanoindentations made in semiconductors and ceramics [38]. Their TEM observations were on indentations made with a Berkovich indenter so that a correlation between the indentation P-h curve and the microscopy analysis could be established. The authors confirmed the previous observations that: (i) Si becomes amorphous in response to high contact stresses under a hardness indenter; and (ii) dislocation arrays are observed around the deformed indentation where contact loads exceed a threshold value. They also argued that the dislocation arrays they observed might accommodate displacements from the densification transformation from Si-I to Si-II, rather than being the primary plastic deformation mechanism. Furthermore, they pointed out there is an extra reflection observed from a 250 nm indentation and showed the dark field (DF) images acquired from the extra reflection. However, the crystal structure from which the extra reflection came from was not clarified.

TEM observations by Callahan and Morris revealed plastic extrusions in indentations made with a Berkovich indenter in (100) Si at loads of ~10 mN [39]. Polycrystalline Si-I was revealed by the electron diffraction pattern; however, there was no evidence of dislocation activity or other mechanisms of plastic deformation operating outside the clearly demarcated transformation zone. As for the origin of the polycrystalline layer, the authors suggested a possible shear fragmentation mechanism or interface recrystallization.

A more recent plan-view TEM study conducted by Ge et al. identified Si-XII and Si-III within the transformed zone [40]. These authors considered two possible paths for the phase transformations: (1) direct amorphization of Si-I under load, (fast unloading retains the a-Si structure, while slow unloading induces formation of Si-XII and Si-III); (2) Si-I transforms to Si-II at about 12-13GPa and produces metastable Si-XII and Si-III during unloading, similar to the DAC results. Figure 1. 11 shows the dark field (DF) TEM images acquired from a bc8 reflection (Figure 1. 11a) and a r8 reflection (Figure 1. 11b) which identifies the distribution of the two phases. The bc8 Si-III resides mainly at the center and on the edges, while the r8 Si-XII is mostly found at the sides of the indentation.

Although plan-view TEM can profile the microstructure of the entire indentation at a certain depth, a more complete TEM study would include a cross-sectional study to reveal the residual imprint, the microstructure and sub-surface deformation as a function of depth, and the interface between the transformed zone and untransformed matrix. Furthermore, the volume of the transformed zone could be determined and correlated to the indentation conditions, e.g. peak load and indenter geometry.

1.3.3 Cross-sectional TEM of Nanoindentations in Si

Two Australian groups studied the cross-sections of spherical indentations in Si [41-47]. Bradby *et al.* investigated the mechanical deformation of Si induced by spherical

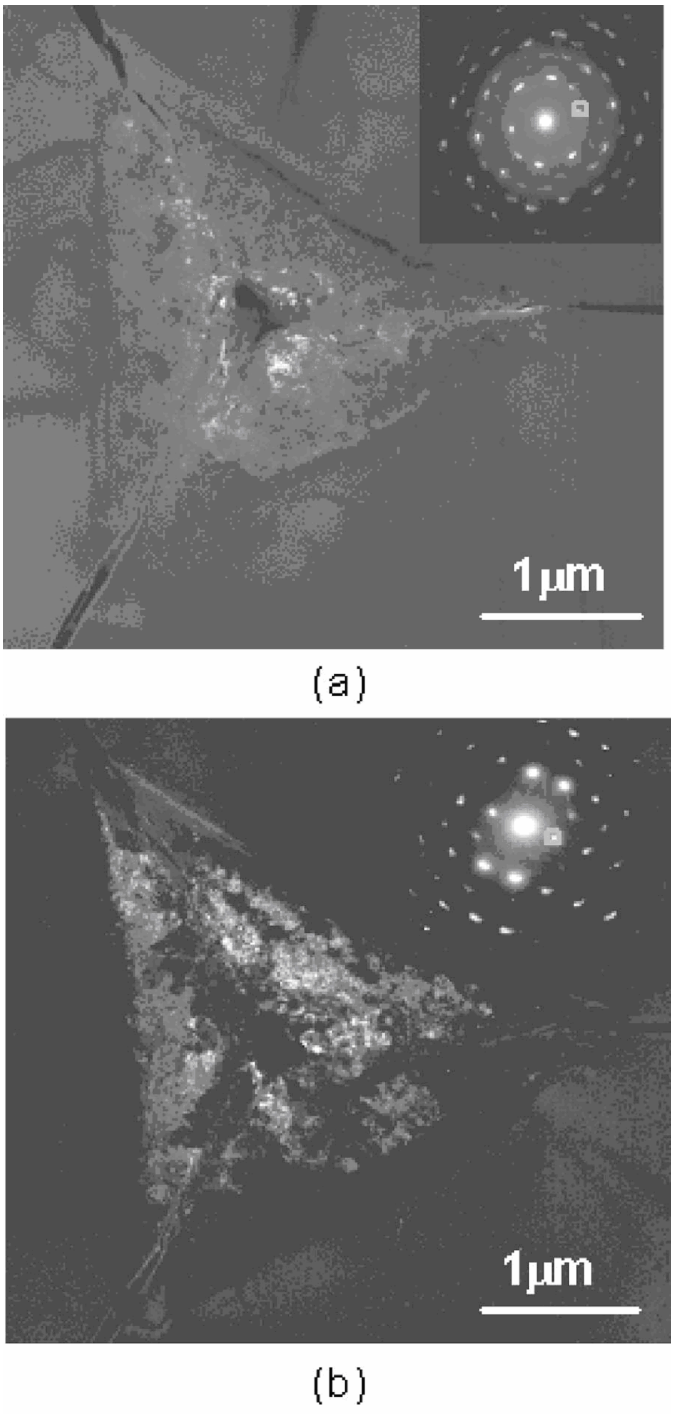

Figure 1. 11 Dark field TEM images from the boxed reflections [200] of Si-III and [010] of Si-XII and the selected area electron diffraction patterns of (a) Si-III (bc8) and (b) Si-XII (r8) in the nanoindentation on a (001) Si wafer [40].

indentation at two different maximum loads: 20 mN and 80 mN with no clearly defined loading/unloading rate[41,42]. The radius of the indenter tip used was calibrated to be 4.2 μm. The subsurface deformation was examined for the 20 mN indentations, although the corresponding load-penetration curve showed almost perfectly elastic behavior. In the cross-sectional TEM observations, slip bands were observed on the {111} planes, as shown in Figure 1. 12. At 20 mN, the phase transformed was limited to a thin region on the surface (region 1 in Figure 1. 12). Only a few particles of the crystalline metastable phase Si-XII were detected at the very surface of the indentation. The 80 mN indent shown in Figure 1. 13 also generated slip bands to a similar depth as that of 20 mN indent (0.8 μ m from the surface). The authors suggested that deformation initiated as slip with small amount of phase transformation. At the load of 80 mN, the surface layer of the indentation was identified to have an amorphous structure, which was related to the sudden, final unloading to ambient pressure [41]. In a deeper region between the slip bands (region 3 in Figure 10(a)), the crystalline Si-I phase was found. The reason the authors proposed for such a phase distribution is that the surface layer is less constrained than the deeper region and has no time to rearrange into another crystalline phase from the high pressure phase Si-II during pressure release. They also addressed loading/unloading rate effects by indenting at one step and 25 steps to a peak load of 250 mN using a Berkovich indenter; however, the total unloading time was not provided, so the actual unloading rates applied were not clear. The results showed that the transformed zone of the 25 step

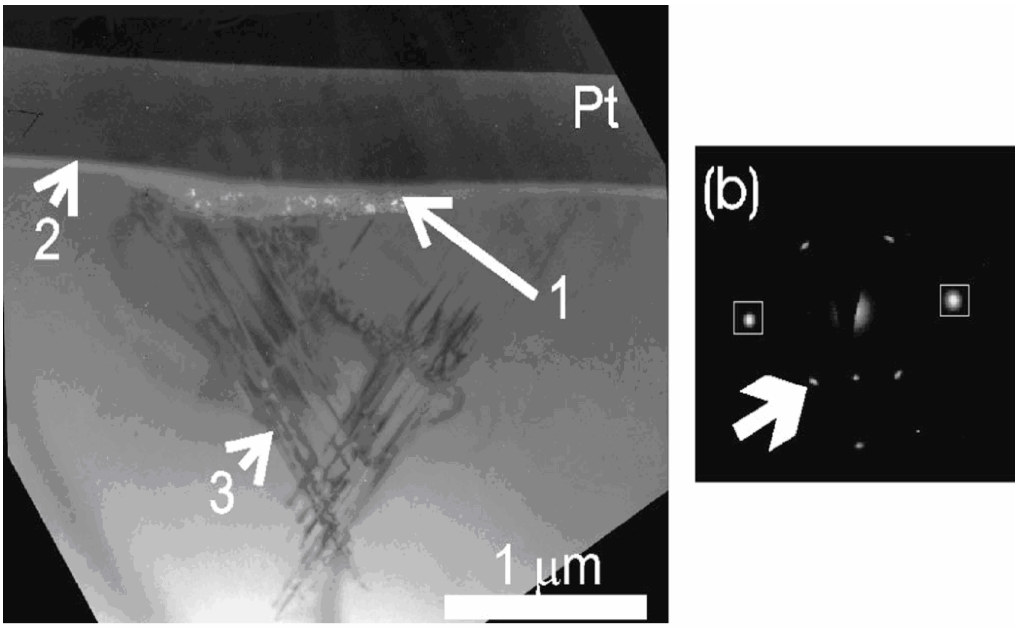

Figure 1. 12 (a) DF XTEM of a spherical indentation in Si made at P_{max} of 20 mN, (b) SAD pattern of the polycrystalline region. All the unboxed reflections are from the Si-XII. Note that the DF image was taken with the indicated spot in (b)[42].

.

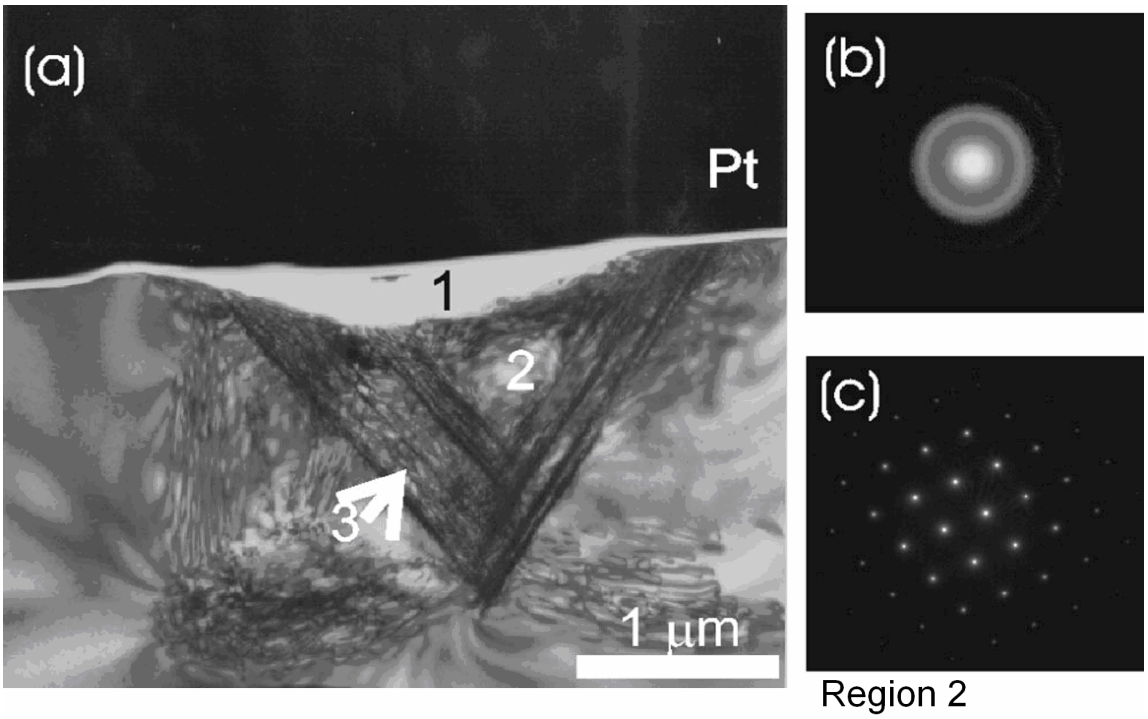

Figure 1. 13 (a) BF XTEM of a spherical indentation (4.2 μm radius) in Si made at Pmax of 80 mN, (b) SAD pattern of the a-Si taken from region 1 in (a) (directly under the residual imprint), (c) SAD taken from region 2[42].

indentation contained only small amount of crystalline Si-I; the one step indentation showed a relative featureless transformed zone [42]. Cross-sectional TEM images of the two indentations are shown in Figure 1. 14. However, the authors did not address the microstructure of these indentations, and simply claimed that the Berkovich (pointed indenter) behaves the same as the spherical indenter.

Zarudi and Zhang performed cross-sectional TEM studies of spherical nanoindentations with peak loads ranging from 30 to 100 mN [43-47]. Figure 1. 15 presents cross-sections of spherical nanoindentations made at loads of 30, 70 and 90 mN, respectively [45]. Planar defects, such as stacking faults, on the (111) planes that developed from the bottom of the transformation zone into the untransformed Si are common features at all the loads. The depth of penetration of the defects increased with indentation load. The authors demonstrated the effects of maximum load by indenting to peak load of 30, 50 and 90 mN at a fixed loading/unloading rate of 0.6 mN/s with a spherical indenter with a nominal radius of 5 μm [44]. The 90 mN indentation showed a purely crystalline transformed zone with elongated grains of size up to 200nm in length located the center of the transformed zone and small fragmented crystals in the peripheral region of the transformed zone (Figure 1. 16a). The large crystals in the central region were identified to be bc8 Si-III by nanodiffraction, and the fragmented crystals were mainly r8 Si-XII. The cross-section of the 50 mN indentation shown in Figure 1. 16b demonstrates a transformed zone of mixed crystalline and amorphous Si. Again the crystals in the central region are relatively large, up to 90nm. These large crystals are identified to be Si-III. The small crystals in the peripheral region of the 50 mN

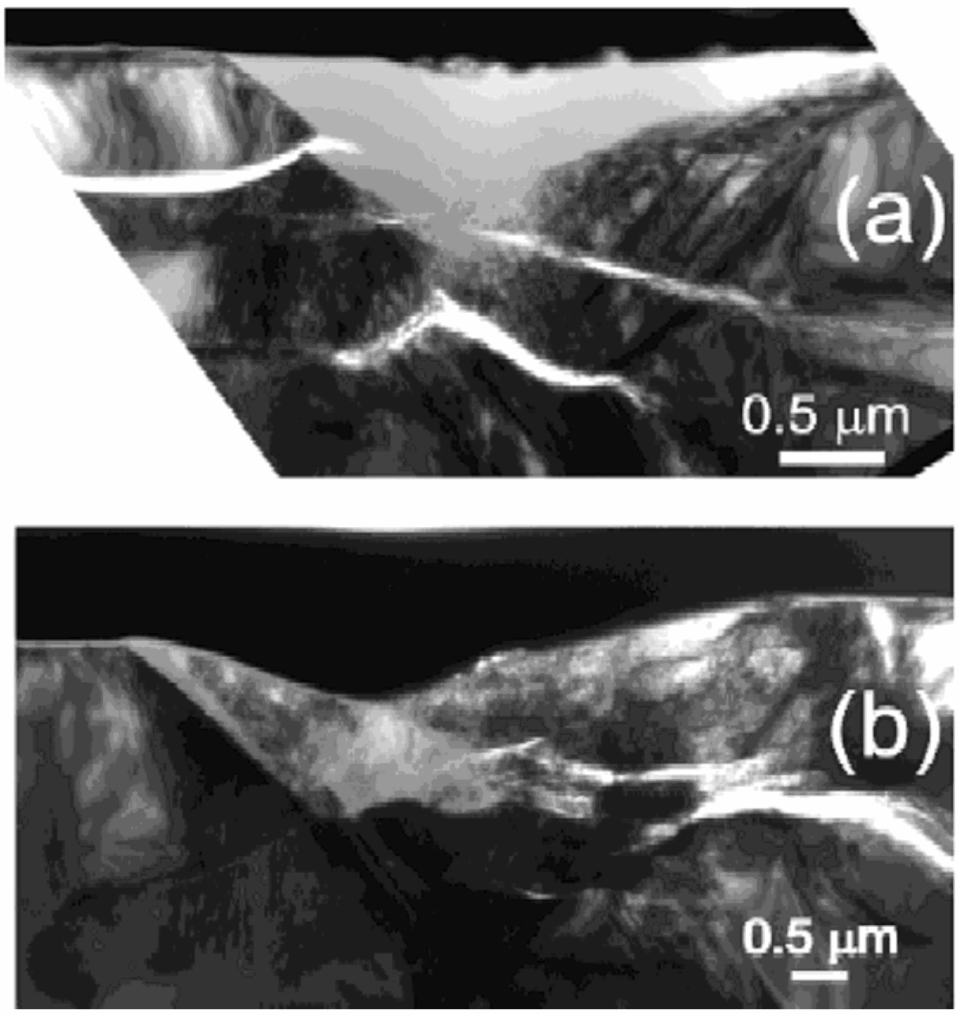

Figure 1. 14 XTEM bright-field images of indentations in Si made using a Berkovich indenter with a maximum load of 250 mN and a continuous load–unload cycle. Indents were made using (a) a single step and (b) 25 steps[42].

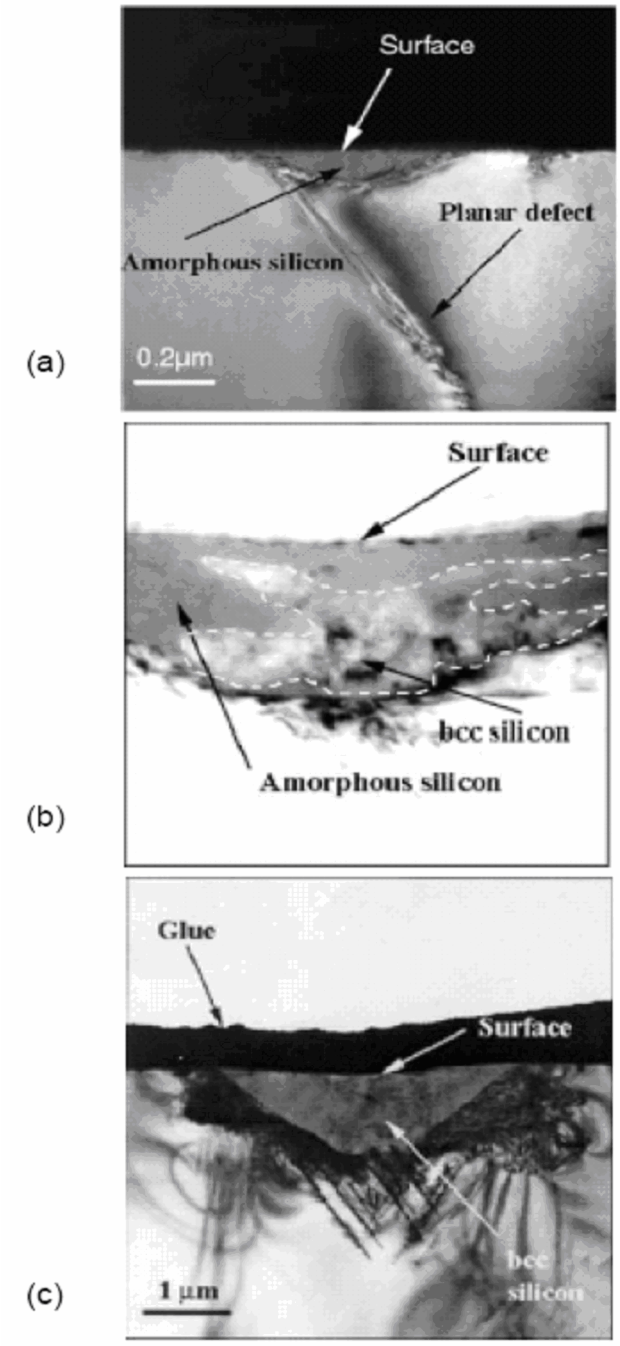

Figure 1. 15 Cross-sectional views of indentation-induced deformation in the subsurfaces of Si specimens after complete unloading. (a) 30 mN, (b) 70 mN, and(c) 90 mN. Note the Si-III particles with lighter colors, highlighted by the dotted white curves in (b) [45].

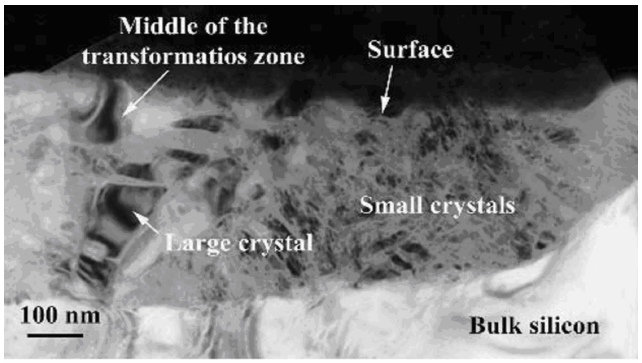

(a)

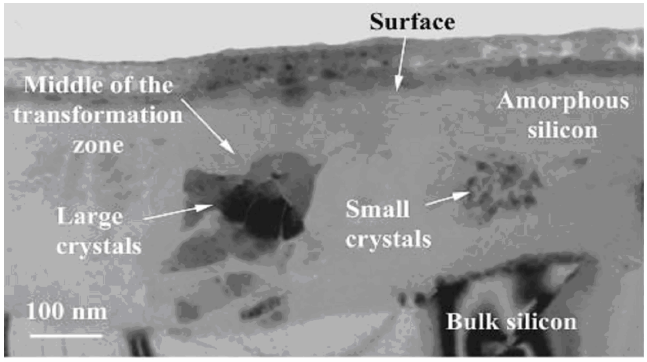

(b)

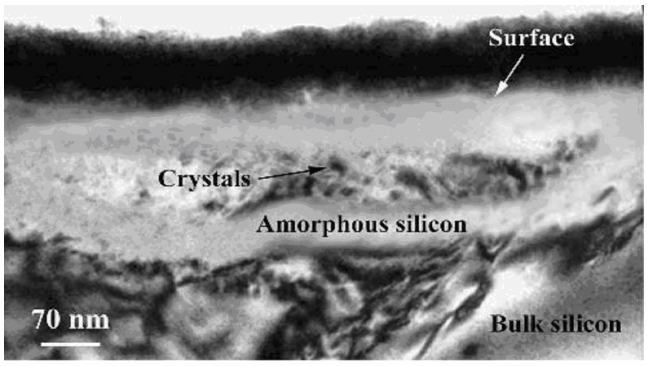

(c)

Figure 1. 16 Crystalline phase in the transformed zone after indentation with a spherical indenter, (a) P_{max} = 90 mN, (b) P_{max} = 50 mN, (c) P_{max} = 30 mN [44].

indentation are so small (30-50nm) that they are beyond the instrument resolution. The transformed zone of the 30 mN indentation is mainly amorphous with a very small amount of crystalline Si-III initiated in the central part of the indentation; the size of the Si-III grain is around 40nm (Figure 1. 16c). In summary, bc8 Si-III crystals are formed in the central region of the transformed zone, whereas the majority of the r8 is in the margin area. Therefore, the author suggested that the Si-III crystals were developed in the areas with a low level of hydrostatic stresses and the r8 Si-XII crystals were likely to form in the regions of high hydrostatic stress. In another study by the same group, selected area diffraction (SAD) and dark field imaging (Figure 1. 17) were used to profile the transformation zone for spherical indentations made at 30 mN and 90 mN at a much faster rate of 3 mN/s, and it was found that the 30 mN indentation resulted in amorphous Si and the 90 mN indentation resulted in crystalline phases Si-III/Si-XII (r8/bc8) [47].

Lloyd et al. used a Berkovich indenter to indent Si, Ge and GaAs to 50 mN at 1 mN/s and concluded that: (1) the transformed zone in Si is a mixture of a-Si and crystalline Si, mostly diamond cubic Si-I and small amount of bc8 Si-III; (2) a median crack exists at the apex of the transformed zone with material extruded into the crack from the transformed zone as shown in Figure 1. 18 [48].

Realizing that the indenter geometry does affect the indentation-induced phase transformations in Si, Saka et al. conducted a systematic cross-sectional TEM study with spherical, Vickers and Berkovich indenters for peak loads ranging from 10 to 500 mN [49]. Loading/unloading was done in 40 steps within 90 seconds for all peak loads; therefore, the loading/unloading rate ranged from 0.25 mN to12.5 mN/s depending on the

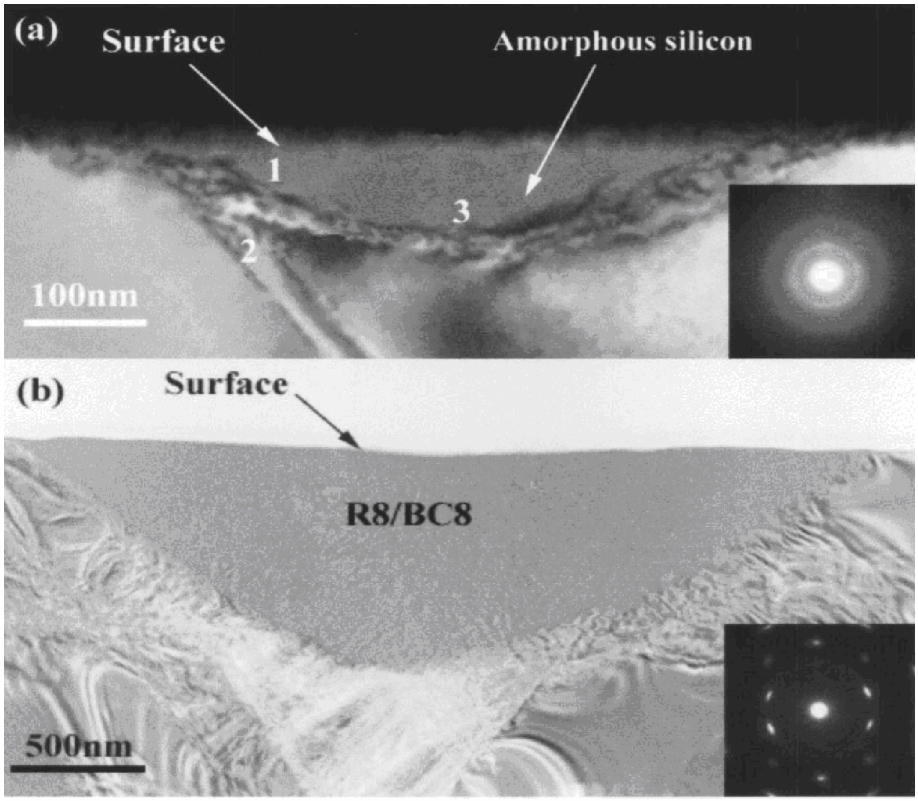

Figure 1. 17 Microstructure of the transformation zone with different *P*max and average loading rate of 3 mN/s (diffraction patterns of the transformation zones are inserted), (a) a dark-field TEM image taken from the P_{max} = 30 mN specimen, (b) a bright-field TEM image taken from the P_{max} = 90 mN specimen [47].

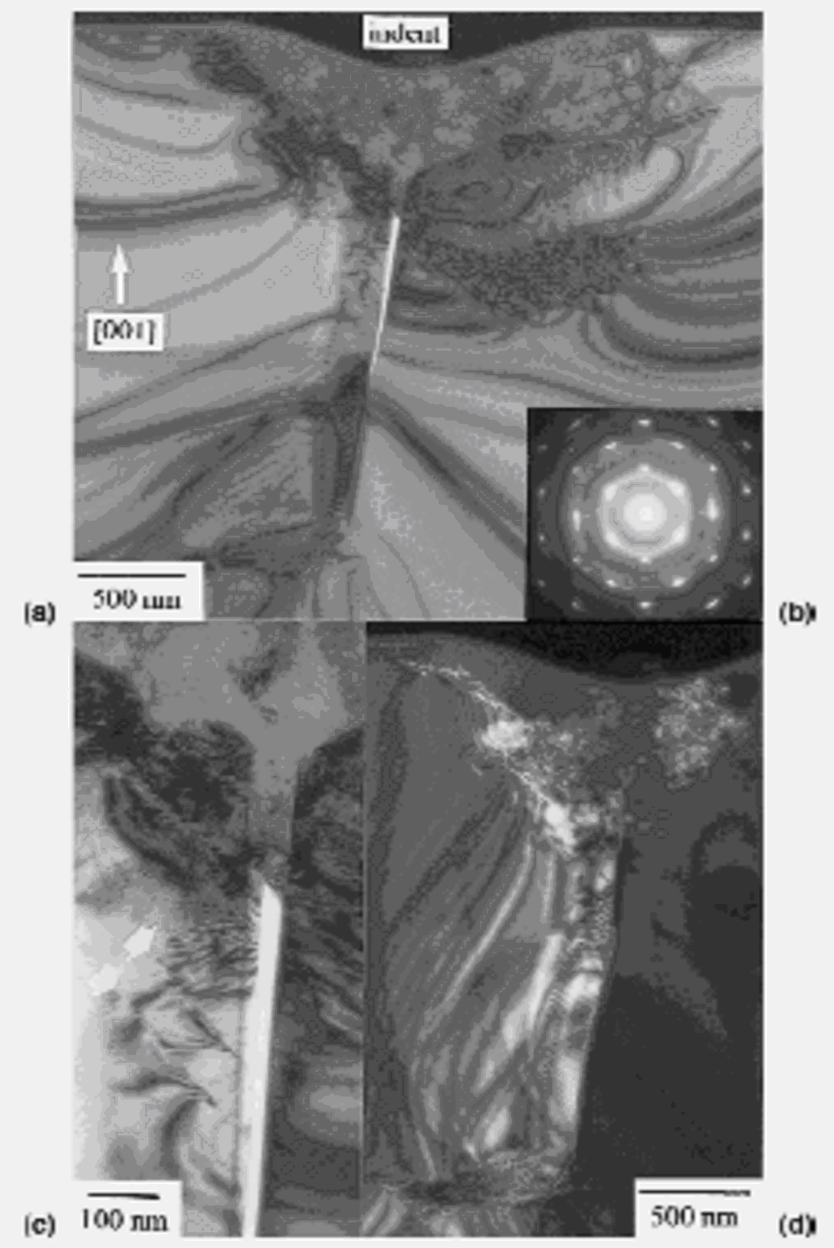

Figure 1. 18 Indent in Si: (a) bright-field image, (b) selected-area diffraction pattern from the transformed zone, (c) bright-field image showing the region around the base of the transformed zone (arrows indicate the slip bands), (d) 111 dark-field image showing a dislocation network associated with the crack [48].

maximum load. For the spherical tip of nominal radius of 5μm (calibrated to be 3.9μm), neither phase transformation nor cracking occurred for peak loads below 60 mN. The bc8 Si-III was only formed after the load was increased to 100 mN, with its periphery corresponding well to the contours of hydrostatic pressure. Therefore, the formation of the bc8 phase by hydrostatic pressure was proposed. No amorphous phase was detected in spherical nanoindentations at any loads up to 120 mN. In contrast, for the sharp tips (Vickers and Berkovich), a-Si or a mixture of bc8 structure and amorphous phase was observed within the nanoindentations. More comprehensive data are listed in Table 1- 2. These results indicate that the presence of shear stress in sharp indentation not only lowers the pressure threshold for phase transformation, but may also facilitate amorphization. Moreover, the transformed zone for Vickers indentation was found to be completely amorphized at loads higher than 100 mN, in agreement with the previous plan-view TEM results of Wu and Page. However, the authors did not point out that it is the fast one step unloading of the Vickers hardness test method which caused the amorphization [36,38].

1.4 Objectives of Study

In summary, current research on the indentation-induced phase transformations in Si indicates that the transformation that occurs during pressure release is affected by several indentation conditions, namely peak load, indentation loading/unloading rate and indenter shape. However, details of the effects of the indentation conditions (peak load,

Table 1- 2 Summary of TEM observations by Saka et al.[49].

Type of indent	Maximum load L_m (mN)	Structure[a]	Dislocations	Pop-in load L_{p-i} (mN)	Pop-out load L_{p-o} (mN)	Cracks[b]	Figure
Spherical	20	DC single	No	No	No	No	3
	45	DC single	112	40	No	No	4 (*a*)
	60	DC single	110 + 112	40	25	No	4 (*b*)
	100	BC8 (bcc)	110 + 112	40	30	H	Not shown
	120	BC8 (bcc)	110 + 112	40	45	H	5
Vickers	10	Not examined	Not examined	No	No	Not examined	—
	50	BC8 (bcc) + A	110 + 112	No	16	H	7
	100	A	110 + 112	No	50	H	Not shown
	250	A	110 + 112	No	100	H + L	8
	500	A	110 + 112	No	280	H + L	Not shown
Berkovich	10	Not examined	Not examined	No	No	Not examined	—
	50	BC8 (bcc) + A	110 + 112	No	15	H + L	Not shown
	100	BC8 (bcc) + A	110 + 112	No	40	H + L	Not shown

[a] A, amorphous Si. DC, diamond cubic.
[b] H, half-penny cracks; L, lateral cracks.

rate and indenter geometry) on the phase transformation behavior and the nature of indentation pop-out in Si, are not fully understood. Therefore, the objectives of this study are as follows: (1) establish the correlation between indentation pop-out and the phase transformations (crystalline phase formation) during unloading; (2) determine the factors affecting indentation pop-out behavior in Si and the phase transformation kinetics, namely size/load effects, indenter geometry effects, rate effects and temperature effects; (3) develop a kinetic model that can be used to describe indentation pop-out in Si.

II Experimental Techniques

2.1 Nanoindentation

Nanoindentation, also known as depth-sensing indentation or instrumented indentation testing, is a technique developed during the late 80's to early 90's. This technique allows real time monitoring of indentation displacement in the sub-micron to nanoscale range as a function of applied force. It has proven to be a powerful technique for providing information on mechanical properties, such as hardness and elastic modulus from the analysis of indentation load-displacement (P-h) curves [50,51].

In this study, nanoindentation was carried out utilizing a Nanoindenter-XP (Nano Instruments, MTS System Corp., Oak Ridge TN). The indenter assembly is shown in Figure 2. 1. The displacement resolution of the indentation head is 0.02 nm and the maximum indentation depth is 500 μm. The indenter is capable of producing a maximum load of 700 mN with a resolution of 50 nN.

Single crystal Si (100) wafers were indented with Nanoindenter-XP with six triangular pyramidal indenters having centerline-to-face angles, φ, of 35.3° (cube-corner), 45.0°, 55.0°, 65.3° (Berkovich), 75.0°, and 85.0°. A schematic of the indenter geometries is shown in Figure 2. 2, and the equivalent cone angles of the indenters are listed in Table 2- 1. Loading levels from 10 to 100 mN with rates ranging from 0.05 to 20 mN/s were used in this study. Two peak loads, 10 and 80 mN, were used for the cross-sectional TEM study. Prior to each test, the instrument and indenter tip were carefully calibrated using fused silica.

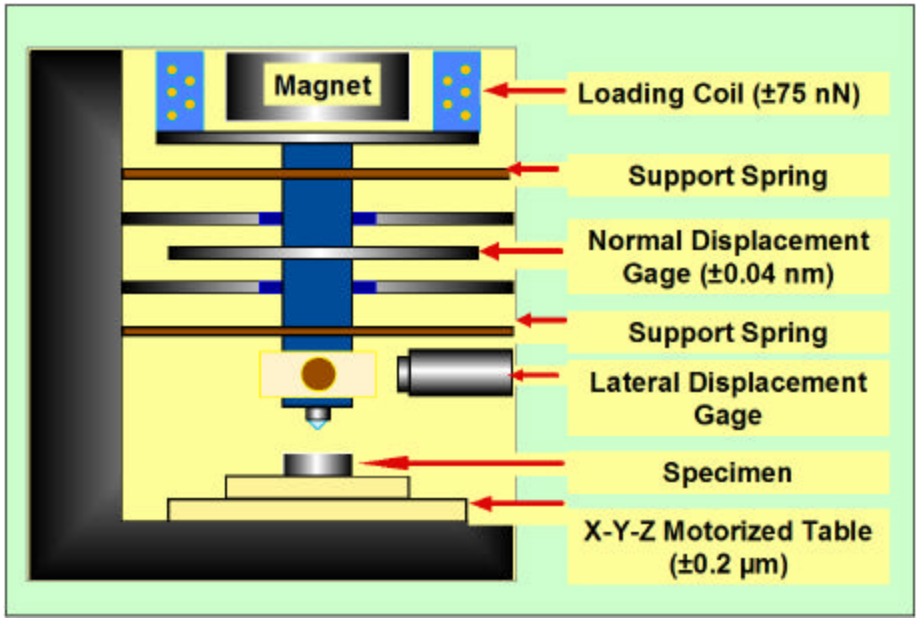

Figure 2. 1 Schematic of Nanoindenter.

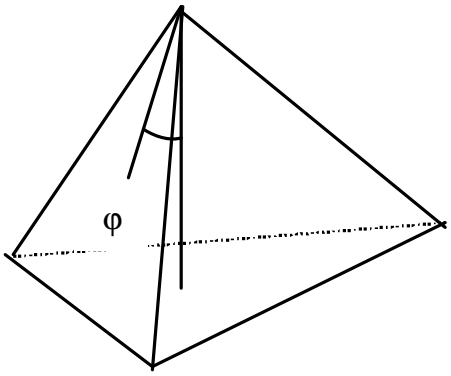

35°(Cube-corner)

45°

55°

65°(Berkovich)

75°

85°

Figure 2. 2 Geometry of Nanoindenters.

Table 2- 1 Geometry conversion data for the pyramidal indenters used in the study.

Centerline-to-face angle φ (°)	Equivalent Cone Angle (°)
35.26	42.28
45	52.13
55	61.43
65.3	70.32
75	78.23
85	86.11

2.2 Scanning Electron Microscopy

Due to the size of the nanoindentations (1μm to a few μm), scanning electron microscopy (SEM) was used to examine the appearance of the nanoindentations in the deformed surface. SEM is also a valuable way to reveal topographic features like surface cracking and extrusion. A Leo 1525 field-emission SEM with an in-lens detector (Carl Zeiess SMT Inc, Thornwood, NY) was employed for the SEM examinations in this study.

2.3 Raman Microscopy

Raman microspectroscopy is a method for identifying metastable phases of semiconductors and determining the residual stress on a surface subjected to contact loading [40,52]. It was used in this study to identify the different phases formed in the hardness impressions. A Dilor XY800 Microprobe (JY Inc., Edison, NJ) was used to identify any crystalline and amorphous phases present after unloading. The scattered light from an Innova 308c Ar+ laser (Coherent Inc., Sanra Clara, CA) operating at 5154 A was dispersed with a diffraction grating and then detected with a charged-coupled device (CCD). In addition, using an average laser spot size of approximately 1 μm, Raman spectral maps of the indents were generated by scanning the surface and using mapping software to profile the distribution of the phases.

2.4 Transmission Electron Microscopy (TEM) Characterization

Cross-sectional transmission electron microscopy (TEM) and high resolution electron microscopy (HREM) were performed using FEI/Philips Tecnai20 and CM200FEG instruments at the SHaRE User Center supported by the Basic Energy Science Office of the US Department of Energy at the Oak Ridge National Laboratory (ORNL). All observations were made at 200kV.

2.4.1 TEM Sample Preparation – Focus Ion Beam (FIB) Milling

In spite of the extraordinary advantages of TEM for investigating microstructures of various materials at the submicron scale, preparation of electron-transparent thin specimens has always been a challenging task. Preparation of TEM cross-sections at the specified location of nanoindentations is exspecially tedious and difficult. Fortunately, the newly developed focused ion beam (FIB) milling technique now makes it possible to prepare TEM cross-sections of nanoidentations with pin-point accuracy.

FIB milling stations operate in a manner similar to the SEM. A dual-beam FIB system has an electron source (with a typical accelerating voltage of 5 kV) like in a SEM, and a gallium liquid metal ion source (typically 30 kV in voltage). The electron beam is used to form images like in a SEM to choose and monitor the working site and the progress; the ion beam is focused to etch and mill materials into their desired shape and thickness.

There are two types of FIB cross-sectioning methods, namely the ‘pre-thinned’ and ‘lift-out’ methods. The “pre-thinned” technique was employed in this study. The

term “lift-out” is self-explanatory - a thin foil is directly extracted from the bulk sample and lifted out. The “pre-thinned” method requires mechanical thinning before milling.

Figure 2. 3 is a flow chart of the TEM sample preparation used in this study. To aid FIB milling, large indentations (Figure 2. 4a) were made as markers to locate the indentation array of interest. Larger indentations were also made alternatively within the array so that positions of the smaller indentation could be identified. For each indentation condition of interest, a strip was first sectioned perpendicularly to the wafer surface with a line of indentations in the edge of the strip (Figure 2. 4b). The strip was then transferred into the FIB for further thinning. A layer of platinum was deposited to protect the indentations during FIBing. FIB milling started using a coarse beam on both sides of the indentation. As milling approached the designated location, the beam size was decreased accordingly (Figure 2. 4c) until the window was thinned down to electron transparency. The strip with the indentation cross-section was then mounted on a sample holder for TEM examination.

2.4.2 High Resolution Electron Microscopy (HREM)

HREM was carried out on a Phillips FEG CM200 on samples thin enough to perform HREM. Numerous micro and nanoscale features were imaged and analyzed using FFT (Fast Fourier Transformation) simulation implemented in the imaging software licensed by Gatan, Inc.

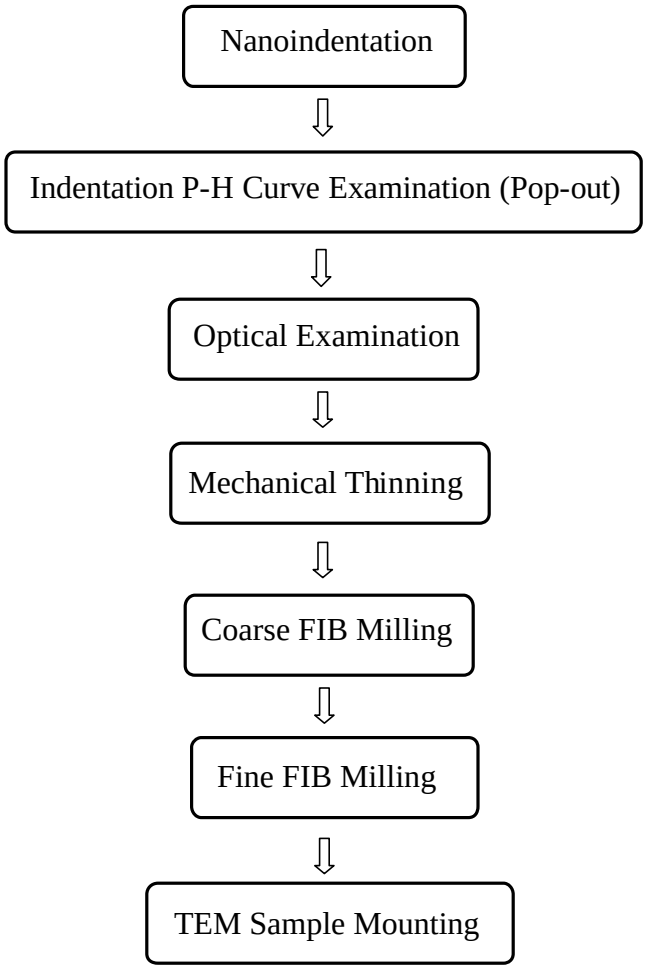

Figure 2. 3 TEM sample preparation procedure.

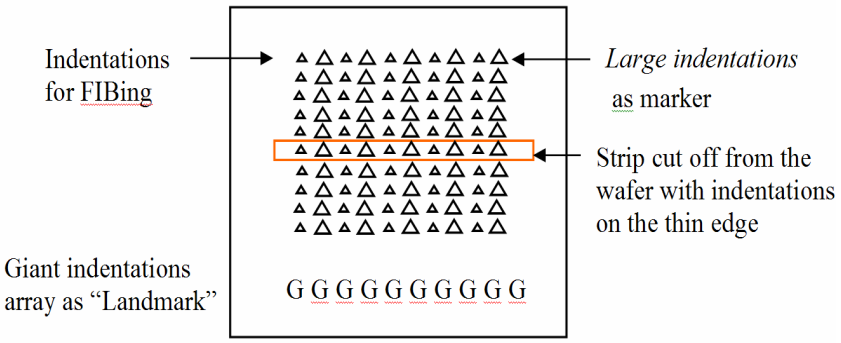

(a). Indentation arrays

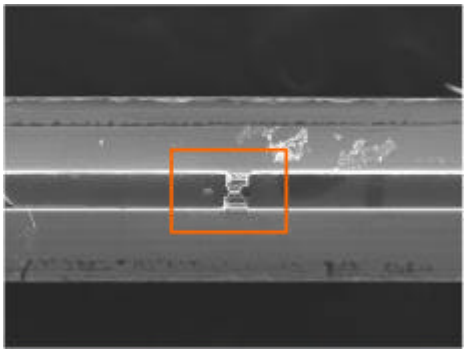

(b). The thinned edge of the strip with the FIBed indentation in the boxed

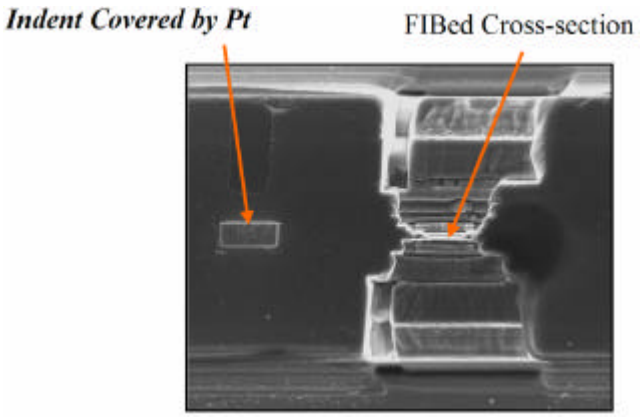

(c). Strip extracted with the FIBed indentation cross-section

Figure 2. 4 TEM cross-section preparation.

III Experimental Results and Discussions

3.1 General Study of Indentation-induced Phase Transformation in Si

In order to characterize how the imortant indentation parameters affect the phase transformations in Si, single crystal Si (100) wafers were indented using the Nanoindenter-XP with six triangular pyramidal indenters having centerline-to-face angles, Ψ, of 35.3° (cube-corner), 45.0°, 55.0°, 65.3° (Berkovich), 75.0°, and 85.0°. Indentation peak loads in the range of 10 to 80 mN and unloading rates of 0.5, 0.5 and 5 mN/s were applied. Micro-Raman spectroscopy analyses were conducted to assist in phase identification within the indentations. The size of Ar^+ laser light spot used to generate the Raman spectra was approximately 1 μm; therefore, Raman observation was limited to indentations made at peak loads of 30 mN and above. Maps constructed using Raman spectra showing phase distributions in and around the indentation were also acquired for cube-corner and Berkovich indentations. The indentations were examined under SEM for visible features of deformation, phase-transformation, and surface cracking. Cross-sectional TEM study was carried out on nanoindentation cross-sections made at 10 and 80 mN peak loads.

3.1.1 Indentation Load/Size Effects for the Berkovich Indenter

The indentation peak load determines the amount of material transformed, i.e., the size of the transformed zone. Using the Berkovich indenter with a fixed unloading rate of 5 mN/s, nanoindentation data for 10, 30, 50, and 80 mN peak loads are shown in Figure 3.

1. The low peak loads, 10 mN and 30 mN, show typical unloading curves with the "elbow" shape. The high peak loads always promote the sudden backward displacement of indenter or "pop-out". The transition between "elbow" and "pop-out" is between 30 and 50 mN peak load; above this range, pop-out will occur during unloading, and below this range, pop-out is not likely to occur during 5 mN/s unloading. For the 100 mN peak load, the pop-out displacement of more than 50 nm can be easily read from the plot.

3.1.2 Indenter Angle Effects

Angle effects were studied by indenting with six triangular pyramidal indenters having centerline-to-face angles, φ, of 35.3° (cube-corner), 45.0°, 55.0°, 65.3° (Berkovich), 75.0°, and 85.0° at peak loads of 10 to 80 mN. Micro-Raman spectroscopy analyses were conducted on the 80 mN indentation to compare the indentation pop-out behavior with the phase composition within the indentations. The 10 mN indentations, which are about 1 μm in size, were not examined by micro-Ramam due to the limitation of the Ar^+ laser light spot size (approximately 1 μm). Microstructural evaluation was carried out on nanoindentations made at peak load below (10 mN) and above (80 mN) the transition load range cross-sectional TEM observation.

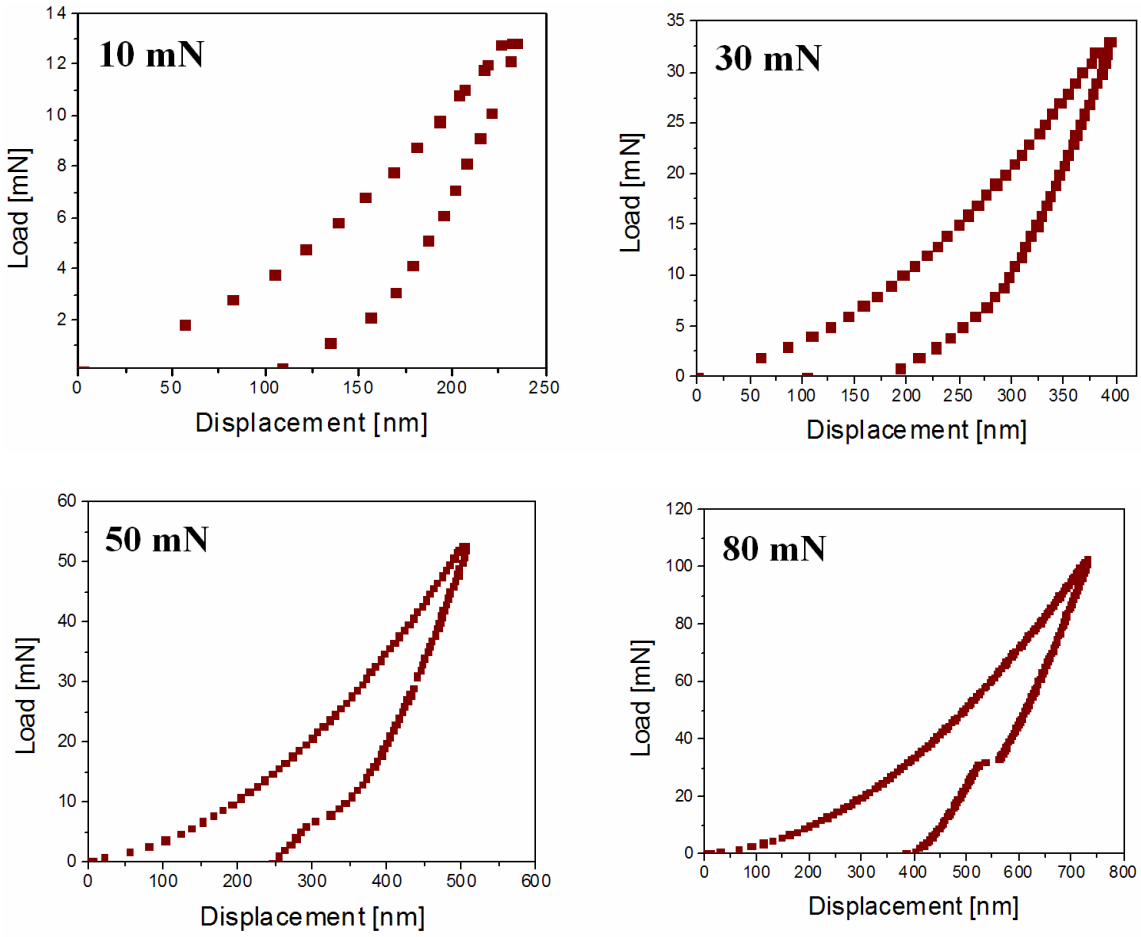

Figure 3. 1 Berkovich indentations at 10, 30, 50 and 100 mN at 5 mN/s.

3.1.2.1 Indenter Angle Effects at Low Peak Load

Typical indentation P-h curves for a 13 mN peak load for all six indenter geometries at 5 mN/s are shown in Figure 3. 2. The sharper indenters produce more residual deformation whereas the very blunt 85.0° indenter exhibits fully elastic behavior as evidenced by a fully retraceable loading and unloading curve. The slope of the unloading curves is similar for all geometries until it is about half unloaded. No pop-out appears on the P-h curve for any indenter geometry under this indenting condition. These indentations were examined by plan-view SEM and cross-sectional TEM with the exception of the fully elastic 85.0° indentation (Figure 3. 3). The topographic contrast in the SEM plan views clearly shows that the residual depth increases as the indenter angle decreases, in agreement with the indentation P-h curves (Figure 3. 2). The surface radial cracking is most pronounced for the sharp indenters but is not present for indenter angles of 65° and above. The most notable feature is that the cube-corner indenter shows extrusion of transformed material which forms a thin wispy layer on the surface.

The cross-sectional TEM images also reveal that the shape of the transformed zone is similar for all indentations. As shown schematically in Figure 3. 4, the zone appears to be triangular in shape with an apex angle of approximately 90°. However, the amount of transformed material in the zone decreases with increasing sharpness of the indenters. For the Berkovich (65°) and 75° indentations, the transformed material remains

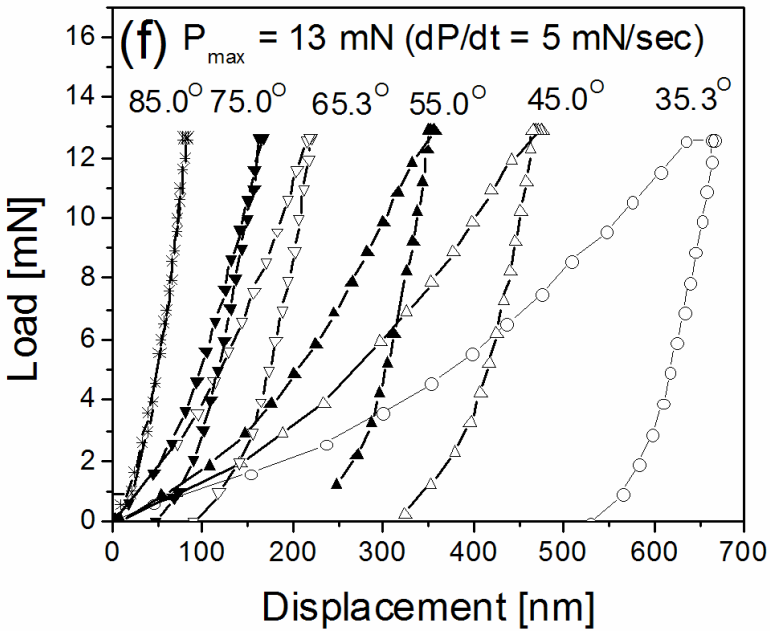

Figure 3. 2 Typical indentation P-h curves for P_{max} of 13 mN at 5 mN/s.

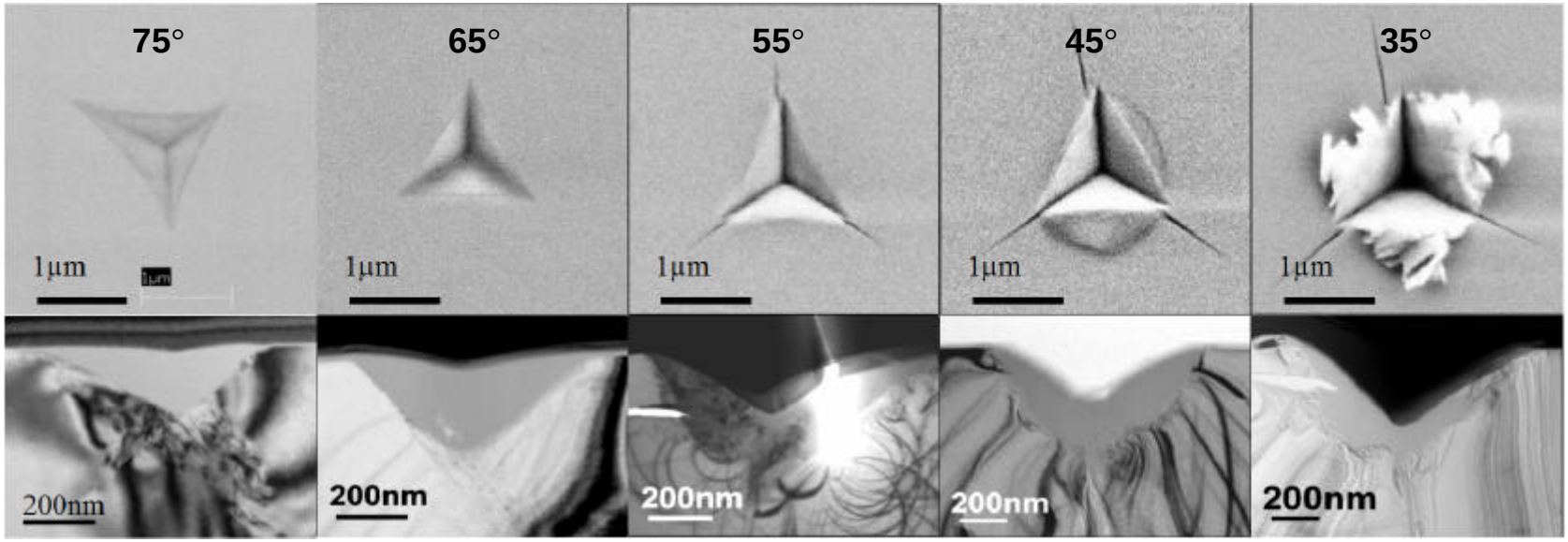

Figure 3. 3 SEM plan-view and TEM cross-sectional images of low load indentations (10 mN) made with various triangular pyramidal indenters.

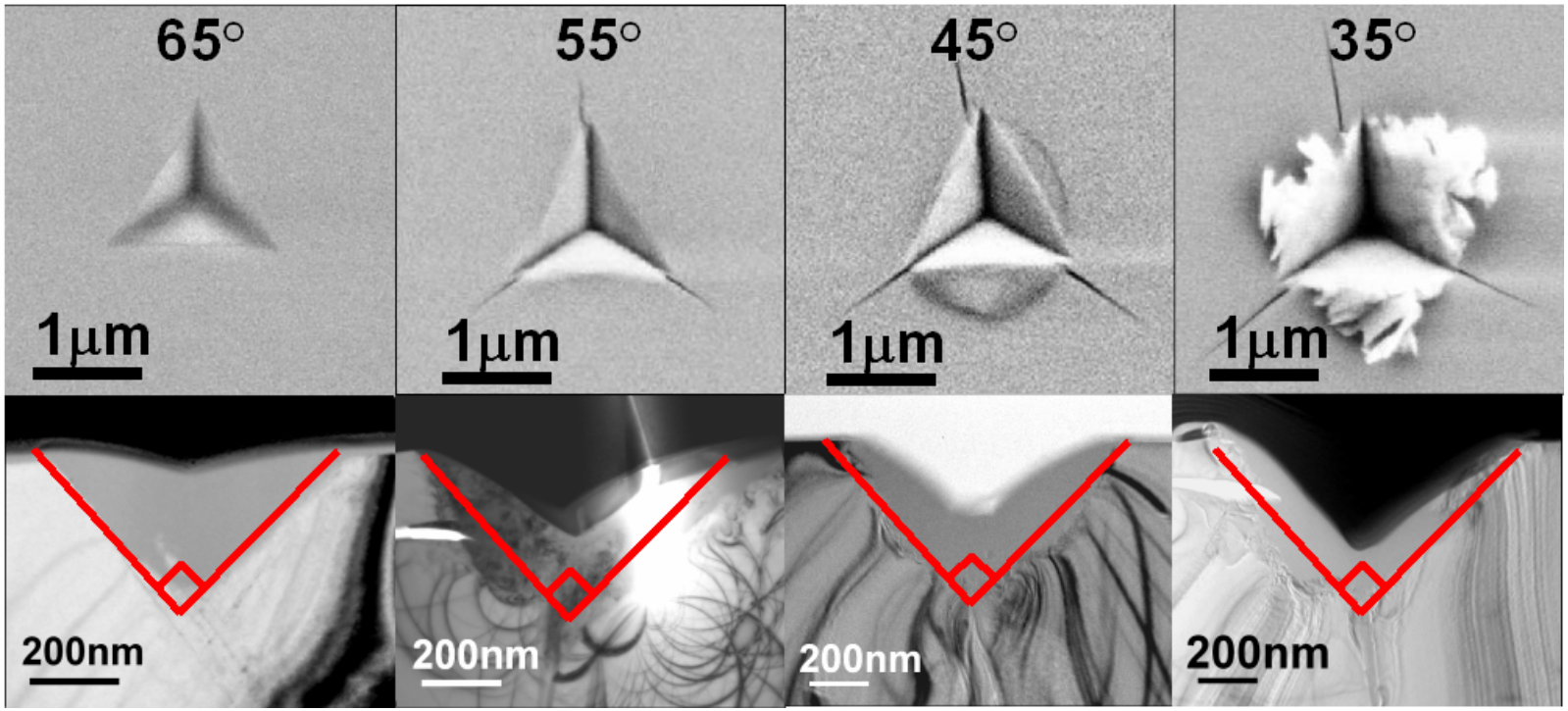

Figure 3. 4 The transformed zone shape schematic outlined approximately in the shape of an apex of 90° for 65° to 35° indentations.

entirely captured by the indenter because the transformed zone does not extend beyond the edge of contact. They also show no evidence of radial or median cracking, in both plan view and cross-section view. Cracks are observed for all the other indenter angles, and material from the transformed zone flows into the median cracks, another evidence of the ductile nature of the high-pressure phase. For the cube-corner indentation, the amount of transformed material under the hardness impression is smaller than all others, presumably due to the extrusion to the surface.

Bright field (BF), dark field (DF) imaging and selected area diffraction (SAD) were carried out on indentations of all geometries under this indenting condition to characterize the microstructure of the transformed zone and extruded materials where applicable. High resolution electron microscopy (HREM) work was also done on selected cross-sections. All the indenter geometries show a mostly amorphous transformed zone with small amount of nanocrystalline Si-I embedded. Detailed analyses of the TEM observations for individual indentation are now presented:

3.1.2.1.1 Cube-corner (35.3°) Indentation

For cube-corner indentation, a featureless thin layer of transformed material is left in the hardness impression as shown in the BF TEM image in Figure 3. 5of the indentation made at 10 mN peak load and a rate of 5 mN/s. The majority of the ductile transformed material is believed to be extruded by the very sharp tip during indentation. In Figure 3. 5, the circle outlines the position of the aperture used to obtain the SAD

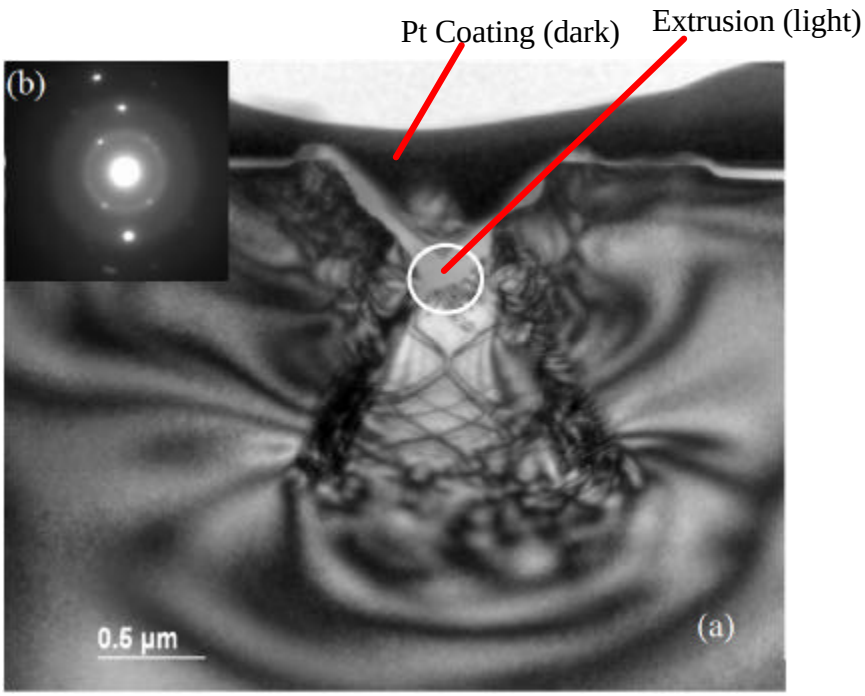

Figure 3. 5 (a) BF image of the cube-corner indentation, (b) SAD taken from bottom of the indentation cross-section. P_{max} = 10 mN, rate = 5 mN/s. Note the circle in the BF image indicates the position of the aperture where the SAD is obtained.

insert. The diffraction pattern consists of diffuse rings, which confirms the presence of a-Si and spot pattern that comes mainly from the Si-I wafer.

3.1.2.1.2 45° Indentation

No extrusion is observed for the 10 mN 45° indentation, all the transformed material is captured within the hardness impression. However, extrusion was observed to flow into the median crack at the bottom of the transformed zone as shown in Figure 3. 6. The transformed zone showed no diffraction contrast with the exception of minor crystalline features mostly populated at the apex of the V shape transformed zone and next to the amorphous and crystalline (a-c) boundary. The crystalline features and the median crack can be better viewed at higher magnification in Figure 3. 6b.

A DF TEM image of this indentation, together with the BF image at the same tilt of this cross-section is shown in Figure 3. 7, was obtained with boxed reflection in the SAD insert of the DF image. The reflection from which the DF is obtained appears to be a reflection from a phase other than Si-I. However, a careful indexing of the pattern indicated that it was simply another Si-I (220) type of reflection resulting from Si-I crystals of different orientation than the matrix. Therefore, the crystalline material in the transformed zone that were lit up by this reflection was simply crystals of Si-I.

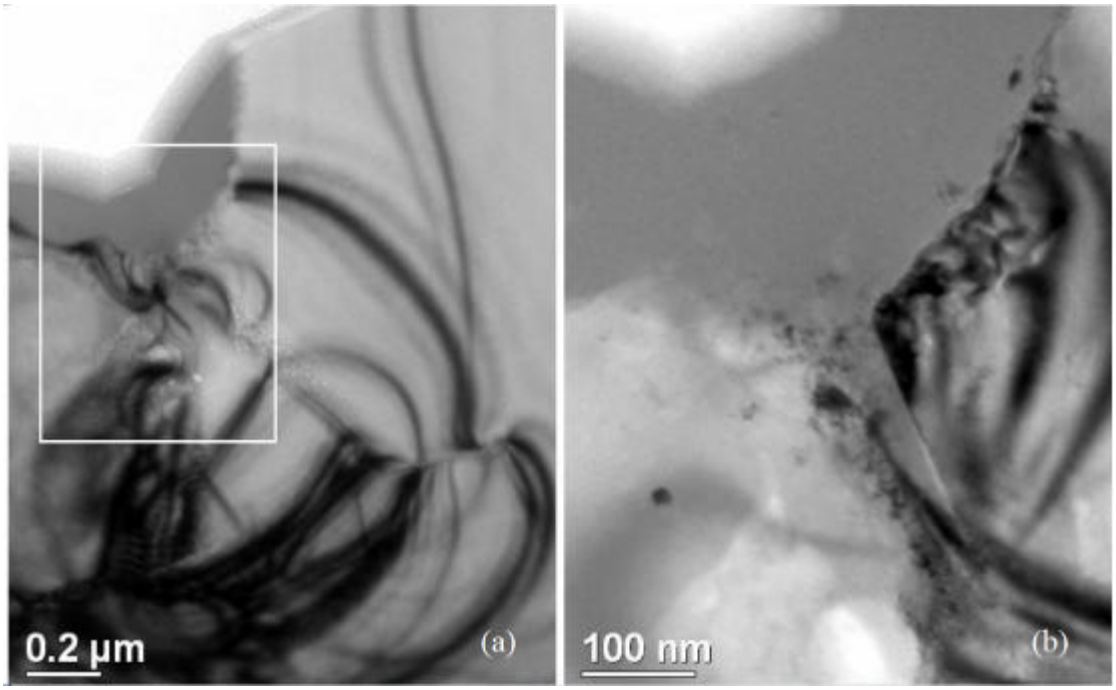

Figure 3. 6 (a) BF image of the 45° indentation made at P_{max} = 10 mN, rate = 5 mN/s, (b) Boxed region in (a).

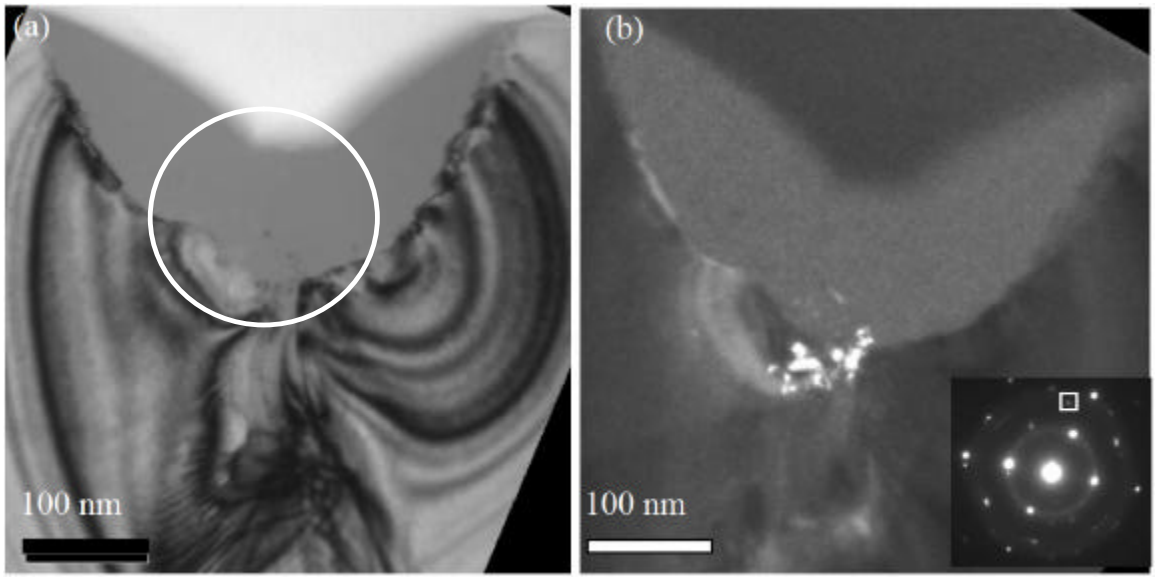

Figure 3. 7 BF (a) and DF (b) image of the 45° indentation made at Pmax = 10 mN at rate of 5 mN/s. Note that the DF image is taken with the boxed reflection in the SAD insert in (b).

3.1.2.1.3 55° Indentation

As shown in Figure 3. 8, the 10 mN 55° cross-section sample demonstrated both median crack and lateral crack that started at the a-c boundary. A FIB damage is obvious on the right side of this cross-section. The transformed zone had a mottled appearance on the BF TEM view in Figure 3. 8a. Figure 3. 8b is the SAD obtained from the circled region in Figure 3. 8a. The SAD pattern clearly resembles a pattern for a Si-I (100) zone and diffuse rings representing a-Si.

HREM was carried out on this sample to examine the locations with crystalline features in the transformed zone. Figure 3. 9 includes a set of HREM images taken in the transformed zone at regions showing crystalline material. The structures of these crystals were simulated by FFT using Digital Micrograph and the simulated SADs are inserted in each HREM image. It is clear from the simulated SADs that the crystalline material in the transformed zone is nanocrystalline Si-I. However,was suspected that the large amount of Si-I in the transformed zone is the result of FIB beam damage during sample preparation rather than phase transformation. This suspicion is due to the obvious FIB damage on the right side of the cross-section and was further supported by observations of in-situ electron beam damage observed while examining other TEM samples.

3.1.2.1.4 Berkovich (65.3°) Indentation

The bright field image of a 10 mN Berkovich indentation made at 5 mN/s is shown in Figure 3. 10a. The large transformed zone (gray) shows no diffraction contrast,

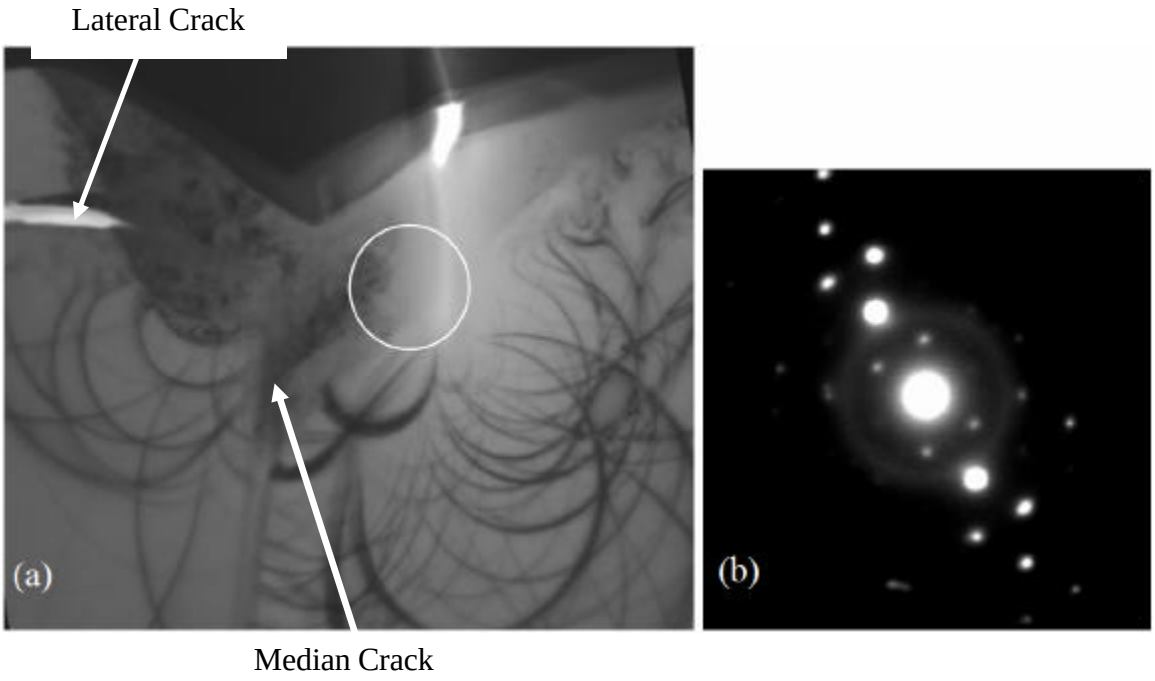

Figure 3. 8 (a) BF image of the 55° indentation made to peak load of P_{max} = 10 mN at 5 mN/s, (b) SAD insert taken from the outlined circle in (a).

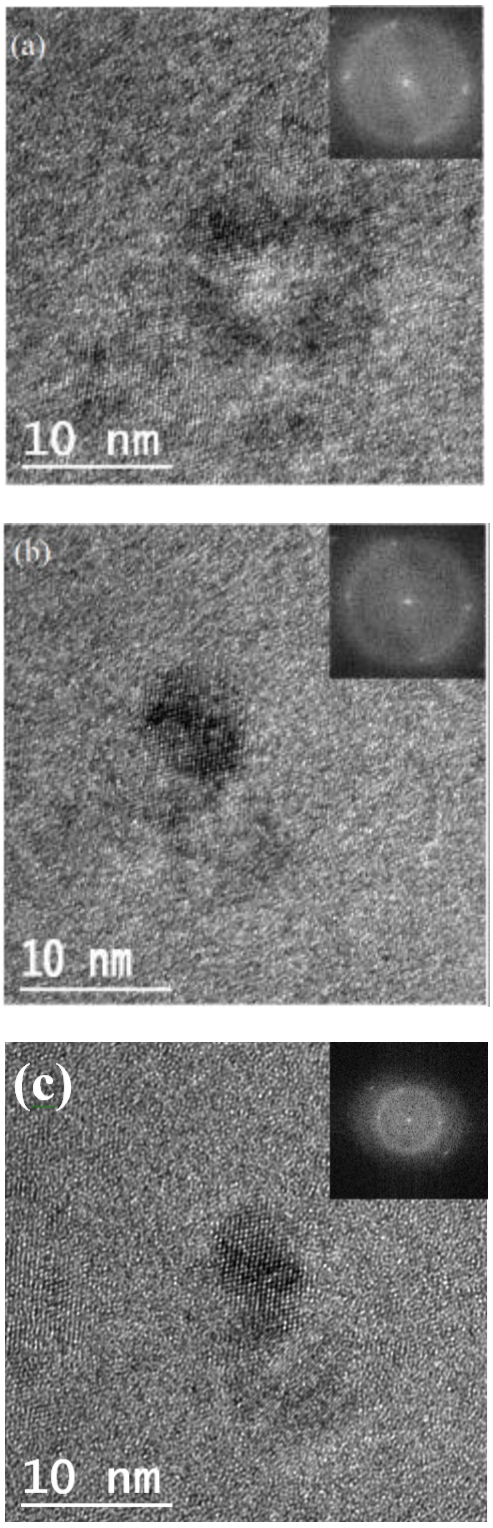

Figure 3. 9 HREM images taken in the transformed zone of the 55° indentation made at peak load of 10 mN at 5 mN/s.

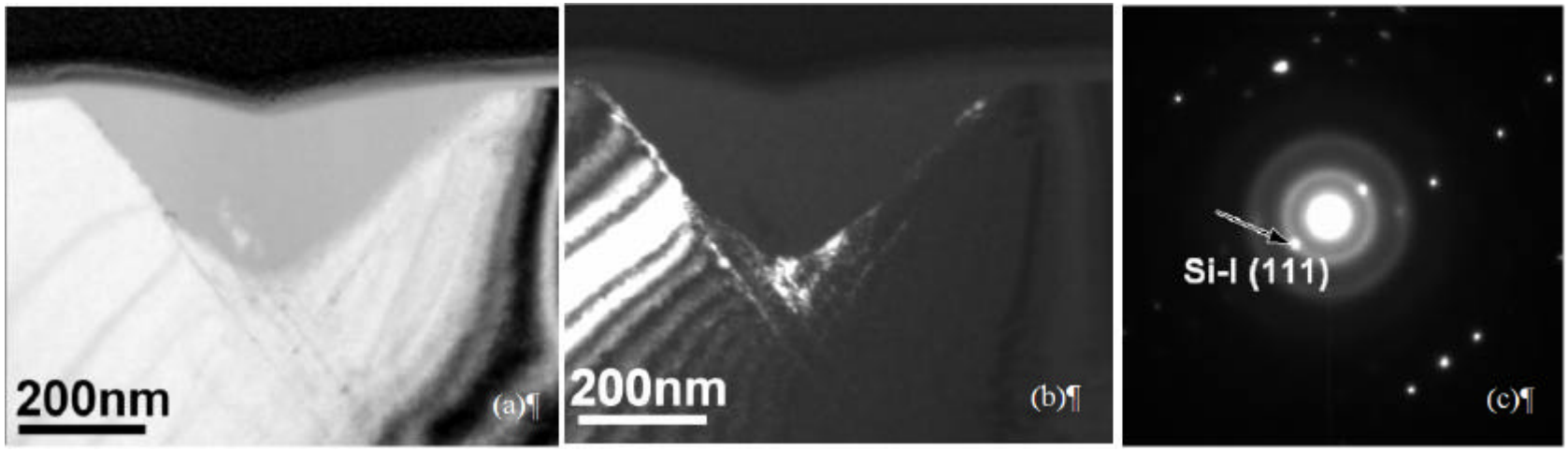

Figure 3. 10 Cross-sectional TEM of the low load (10 mN, 5 mN/s) Berkovich indent: (a) bright field image, (b) dark field image from a Si-I (111) reflection, (c) SAD from the transformed zone.

except a few bright features at the bottom of the zone. In addition, as evidenced by the diffraction contrast in the BF image, bend contours and defects are observed outside the transformed zone. Bright field and dark field images and SAD from the transformed zone (Figure 3. 10c) indicate that material in the zone is mostly amorphous. The reflections in the SAD are mainly produced by the surrounding untransformed Si-I in the (110) zone. Dislocation activity is also observed outside the transformed zone, which is further revealed by the DF image taken with a Si-I (111) reflection (Figure 3. 10b).

Complementary to the SAD and DF technique, HREM was carried out on regions near the crystalline-to-amorphous boundary and within the transformed zone at locations "a" and "b" marked in Figure 3. 11a. The spots at one-third intervals on the (111) direction in the FFT simulated SAD (insert of Figure 3. 11b) are characteristic of twinning. The microtwins are most extensive under the apex of the amorphous pocket and at the crystalline-to-amorphous boundary (Figure 3. 11b). Therefore, beside metallization at high pressure, there remains some plastic deformation on the interface. The twinning observed on a-c boundary is in agreement with the high resolution cross-sectional work of Wu et al. on Vickers indentation test in single crystal Si [37]. In these experiments the indenter was unloaded rapidly in one step. Nanocrystalline grains of Si-I with typical dimensions between 5 and 20 nm were observed by HREM within the transformed region (Figure 3. 11c). However, crystallization of a-Si under the beam growing from a-c boundary was observed during HREM. This observation gives rise to the concern that the original nanocrystals in the a-Si zone (Figure 3. 10a) and the Si-I crystals in the transformed zone

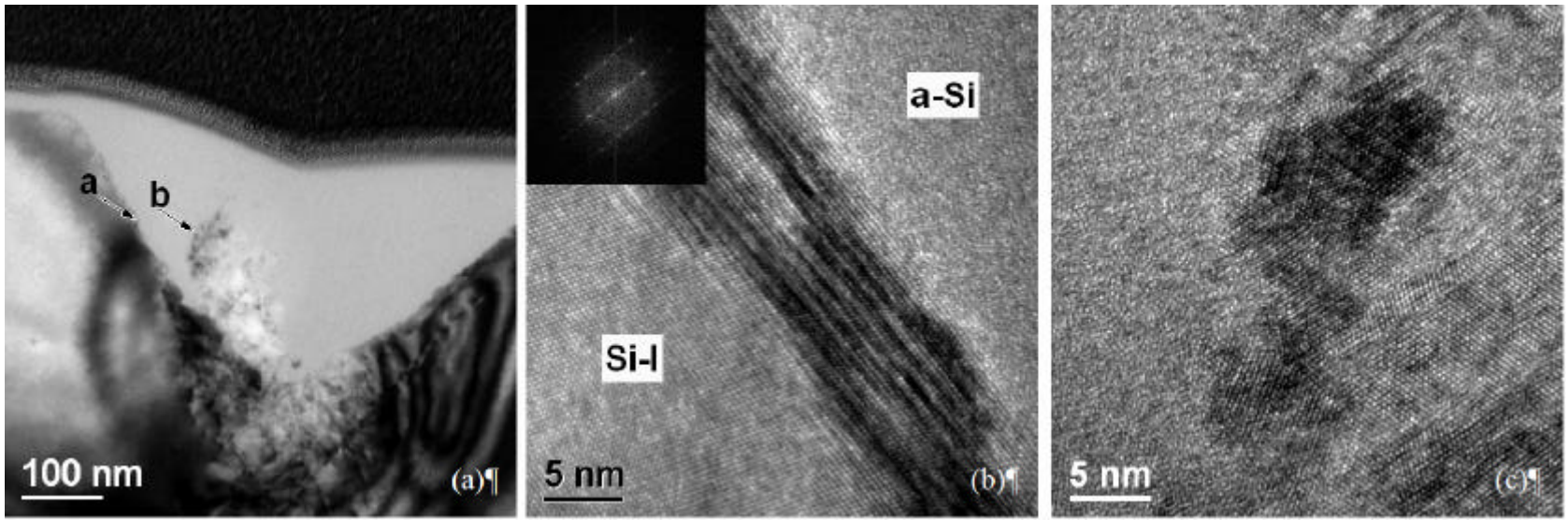

Figure 3. 11 High resolution TEM of a low-load (10 mN) Berkovich indent: (a) bright field TEM image, (b) microtwins at the crystalline-to-amorphous boundary, (c) crystallization in the amorphous transformed zone induced by the electron beam.

of other TEM cross-sections, might be artifacts caused by the ion beam during sample preparation and/or electron beam induced recrystallization.

3.1.2.1.5 75° Indentation

The blunt 75° indenter left a shallower residual imprint than all other angles and a well capped transformed zone as shown in Figure 3. 3 and Figure 3. 12. At 10 mN no cracking was observed by SEM or TEM. The BF TEM image in Figure 3. 12 of the cross-section with the SAD taken over the transformed zone indicated the transformed material is purely amorphous. No diffraction contrast was observed in the transformed zone; therefore, there was no indication of crystalline features in the zone. This could be due to careful sample preparation, or due to the less severe residual stress the blunt 75° indenter left in the material. Figure 3. 13 is a weak beam DF (WBDF) TEM image taken from a slightly different tilt from the BF position of Figure 3. 12. The improved diffraction contrast of the WBDF technique reveals that dislocation lines spread out from the bottom boundary of the transformed zone. Note that at this tilt, only the dislocation lines on the right hand side of the cross-section are revealed.

3.1.1.2 Indenter Angle Effects at High Load

Typical P-h curves at high peak load (80 mN) of various indenter geometry at the fixed 5 mN/s rate are shown in Figure 3. 14a. At this loading level, pop-out is common for the Berkovich (65.3°) and 55.0° indenters. However, for the cube-corner (35.3°)

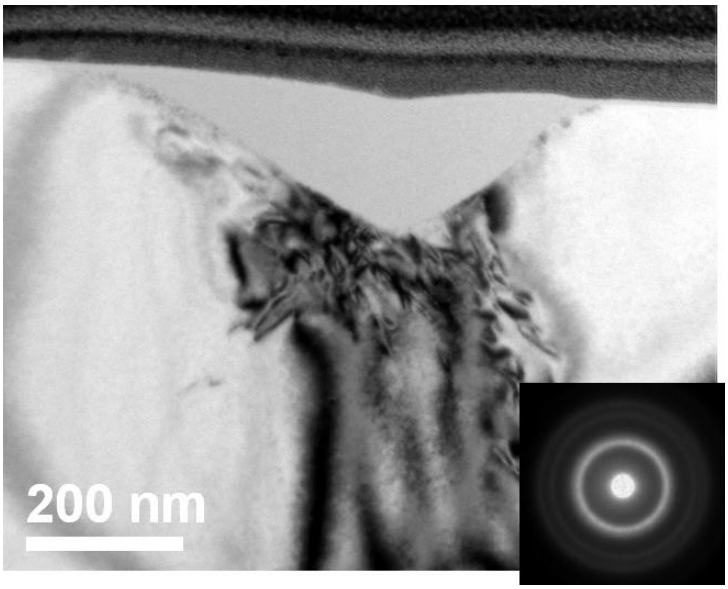

Figure 3. 12 BF image of the 75° indentation made to peak load of P_{max} = 10 mN at 5 mN/s, and SAD insert taken over the transformed zone.

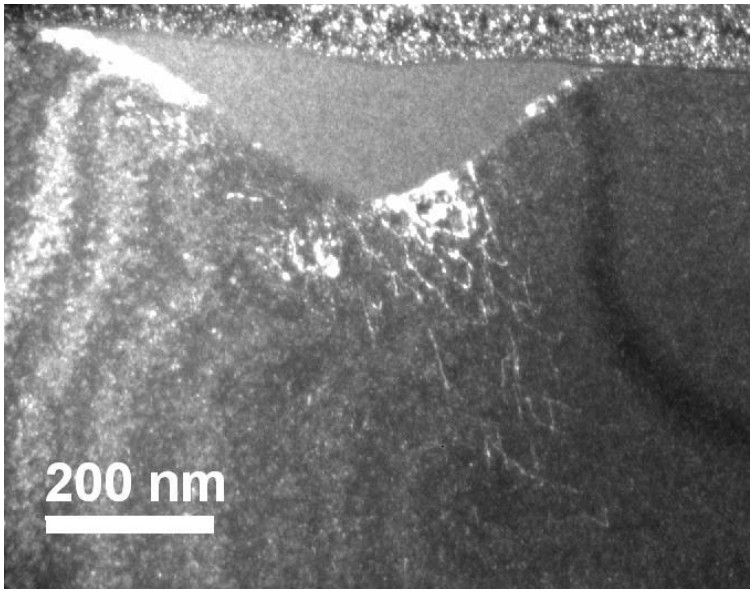

Figure 3. 13 WBDF image of the 75° indentation made to peak load of P_{max} = 10 mN at 5 mN/s that produces the diffraction contrast of the dislocations that reside outside the transformed zone.

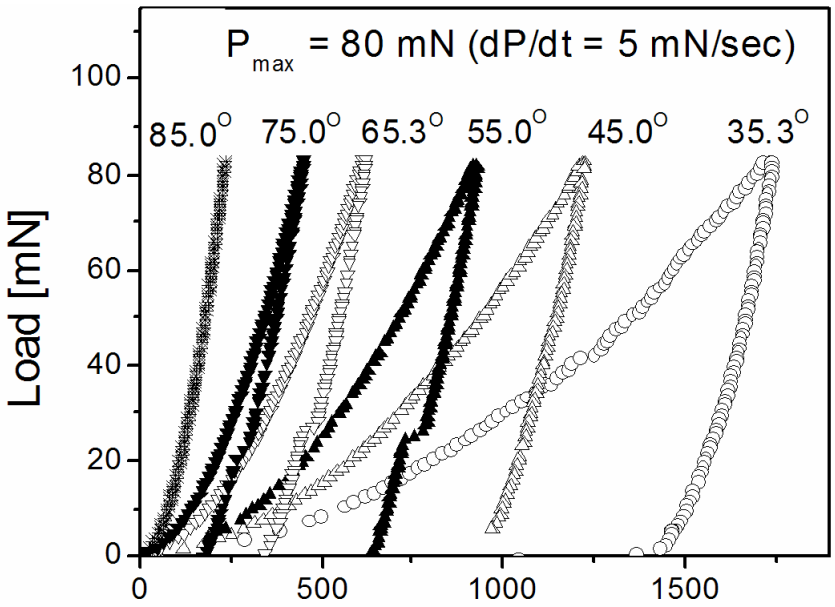

(a)

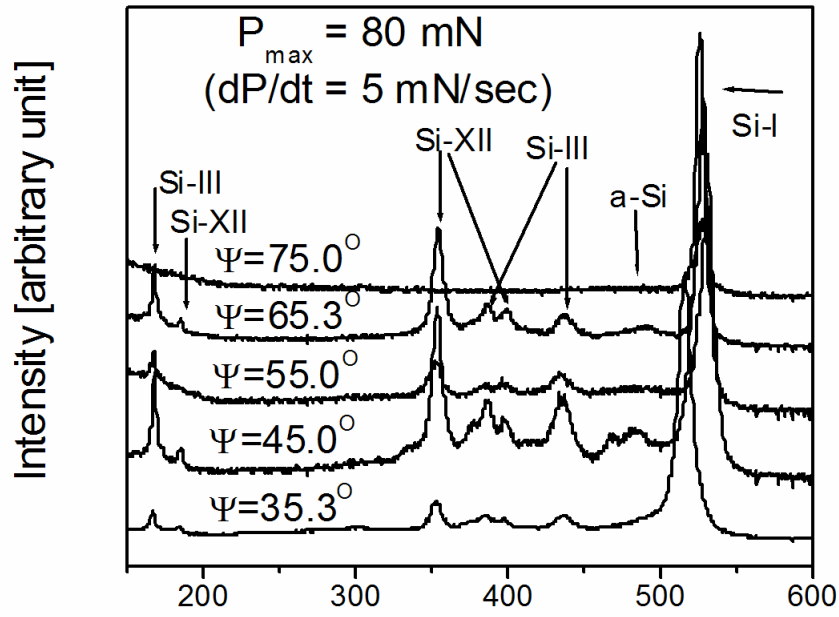

(b)

Figure 3. 14 (a) Typical P-h curves and, (b) Raman spectra, of high peak load (80 mN) indentations made with various indenters at the fixed 5 mN/s rate

and 45.0° indenters, there is no pop-out, which is a surprising observation since sharper indenters displace more material therefore should produce a greater amount of transformed material. The 75.0° indenter shows a mixed behavior of elbow and small pop-out. Again, the very blunt 85.0° indenter exhibits fully elastic behavior.

Typical micro Raman spectra for 80 mN indentations are shown in Figure 3. 14b. The spectra were obtained from the center of each indentation. The characteristic peak of Si-I at 520 cm^{-1}, which came from the pristine Si-I, is observed for all the indentations. The broader peaks at 150, 300 and 470 cm^{-1} and narrow peaks at 165, 350, 382, 395 and 430 cm^{-1} showed up for all the indenter geometries with the exception of the 75.0° indentation. These peaks are identified as amorphous Si and the metastable Si-III/Si-XII, which is in agreement with previous Raman studies [28,32,33,52].

Indention P-h curves, SEM plan-views and TEM cross-sectional views of the Berkovich and cube-corner indentations made at 80 mN are shown in Figure 3. 15. Unlike the low-load condition, where the blunt Berkovich indenter does not induce any cracking at the 5 mN/s indentation rate, both Berkovich and cube-corner indentations made at 80 mN show radial cracks, lateral cracks and median cracks as evidenced by the SEM plan-views in Figure 3. 15a and the TEM cross-sectional views in Figure 3. 15b. The Berkovich indentation exhibits a well-capped transformed zone on the cross-section, whereas the cube-corner indentation demonstrates excessive extrusion of the transformed material. Many detailed TEM observations were made and are discussed:

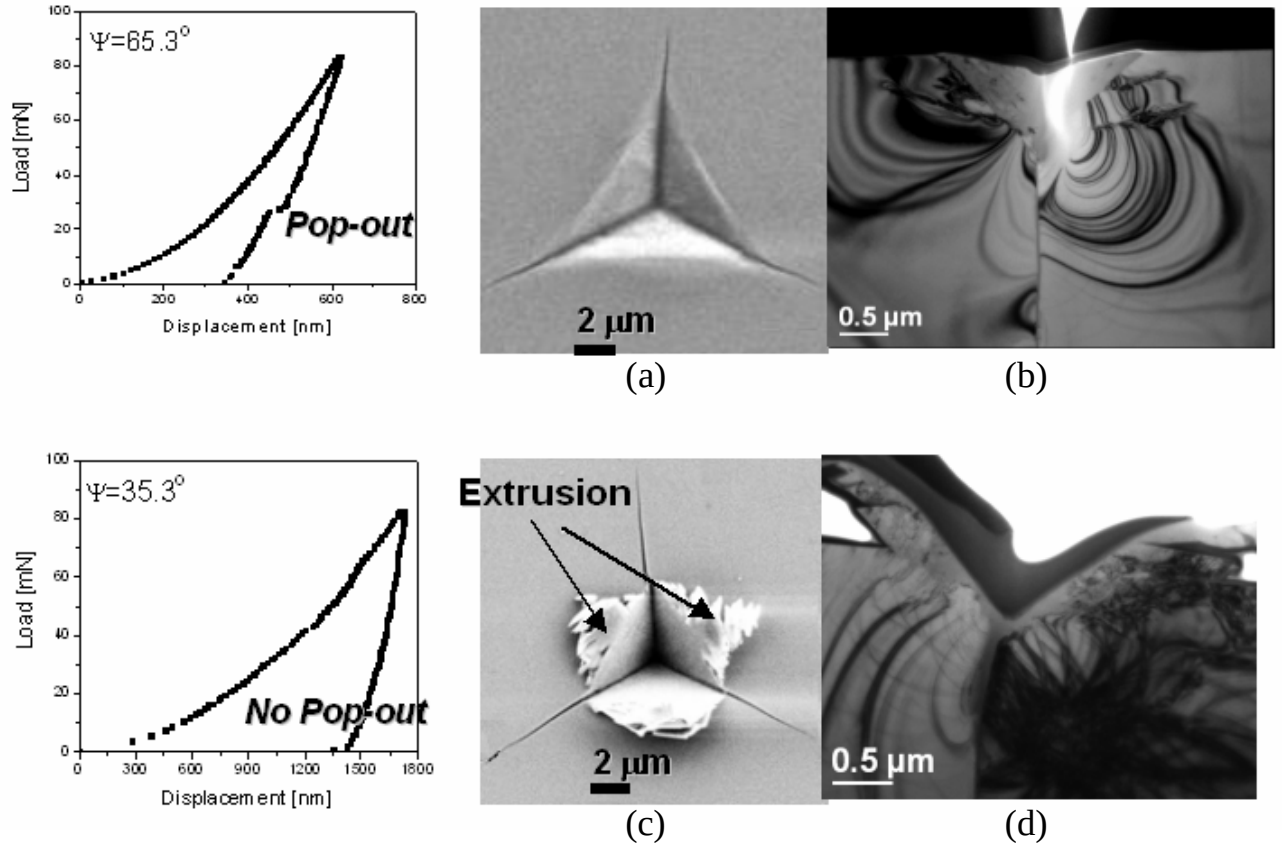

Figure 3. 15 SEM plan-view and TEM cross-sectional images of high load (80 mN) indentations (80 mN): (a) and (b) Berkovich indentation, (c) and (d) cube-corner indentation.

3.1.2.2.1 Berkovich (65.3°) Indentation

In case of the 80 mN Berkovich indentation, lateral cracking was observed starting from the boundary of transformed zone and progressing into the Si-I matrix as shown in Figure 3. 16. Dislocation loops were also observed to initiate from the a-c boundary. SAD obtained over the transformed region is shown in the insert of Figure 3. 16. Indexing the pattern confirmed the presence of both metastable Si-III and Si-XII, in agreement with similar TEM work of other groups [40,42,48,49] and previous indentation and Raman spectroscopy results for similar conditions. The structure of the Si-III and Si-XII phases is very similar to each other with the Si-XII being a slightly rhombohedral form of Si-III. Lattice parameters of these phases are listed in Table 1- 1. Due to the similarity, it is difficult to distinguish the two by simply indexing the SAD. However, rather than separating the two phases, the phase composition in the zone is of more significance for this study. Using TEM DF imaging techniques, Figure 3. 17b, Figure 3. 17c and Figure 3. 17d were obtained with the Si-I (111), Si-III/Si-XII (110) and Si-III (211)/Si-XII (11-2) and (20-1) reflections, respectively. The distributions of the corresponding phases are outlined in the DF TEM images. It is interesting to note that the metastable Si phases seem to have preferred orientation because of the limited number of reflections formed from these phases. This could be explained if the transformed phases inherit in the orientation of the initial material from which they form, which itself is related to the orientation of the undeformed Si-I.

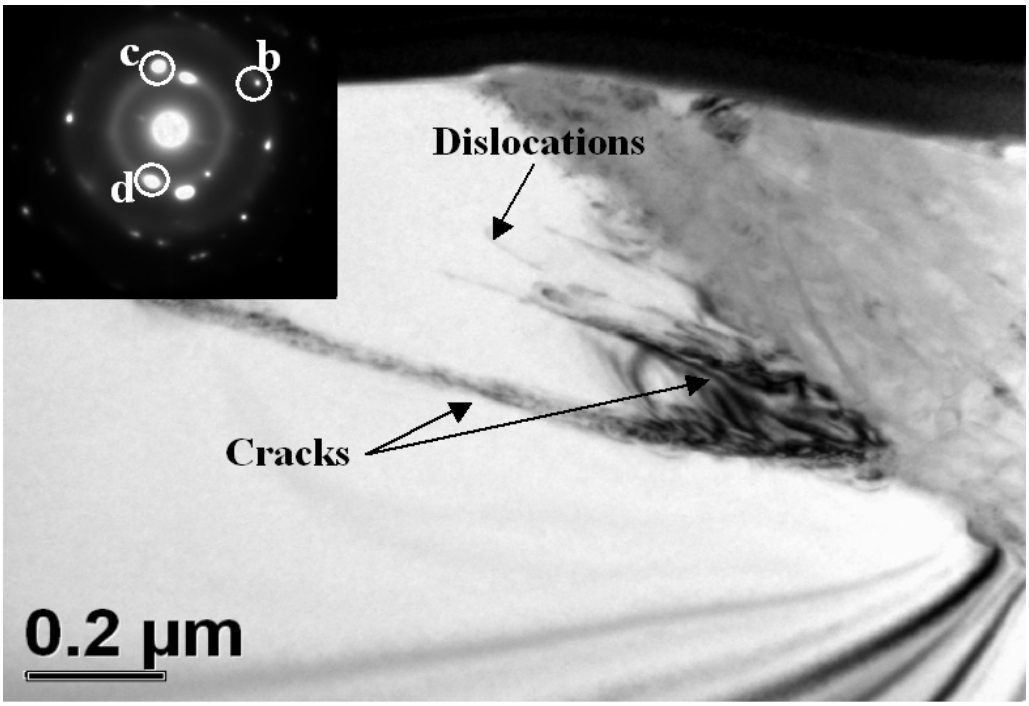

Figure 3. 16 BF TEM image of the 80 mN Berkovich with inserted SAD obtained from the transformed region.

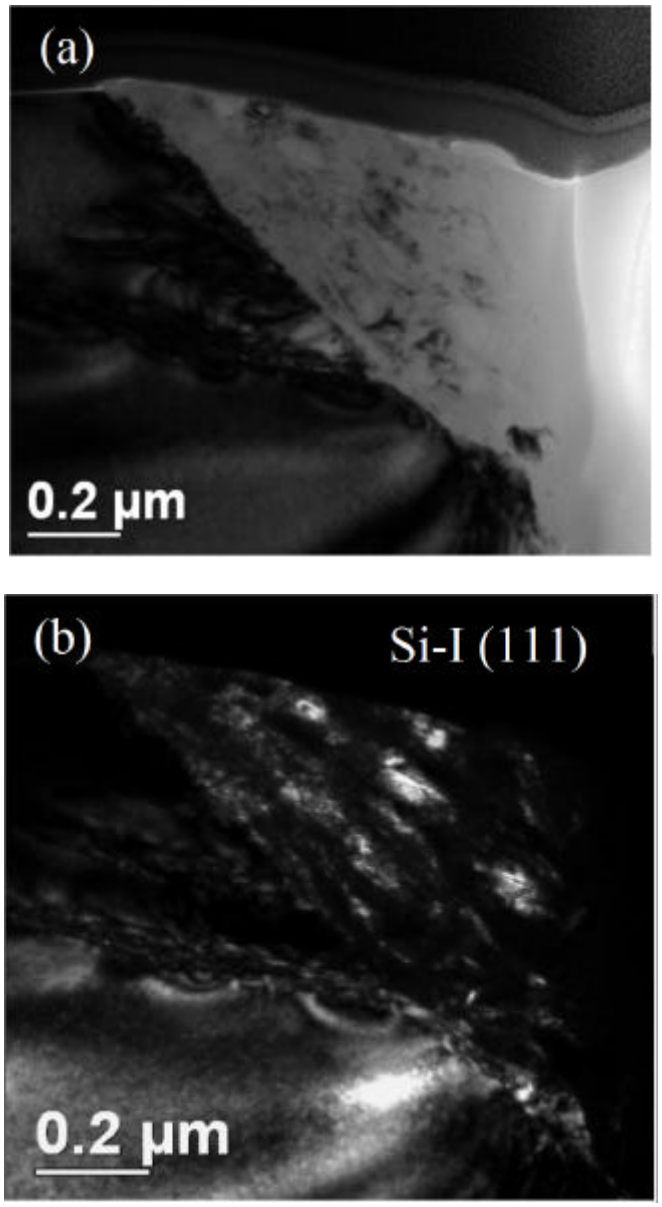

Figure 3. 17 BF TEM image (a) of the left side of the Berkovich 80 mN sample with SAD over the transformed zone inserted; (b) ~ (d) DF TEM images obtained from the labeled reflections in the SAD in Figure 3. 16.

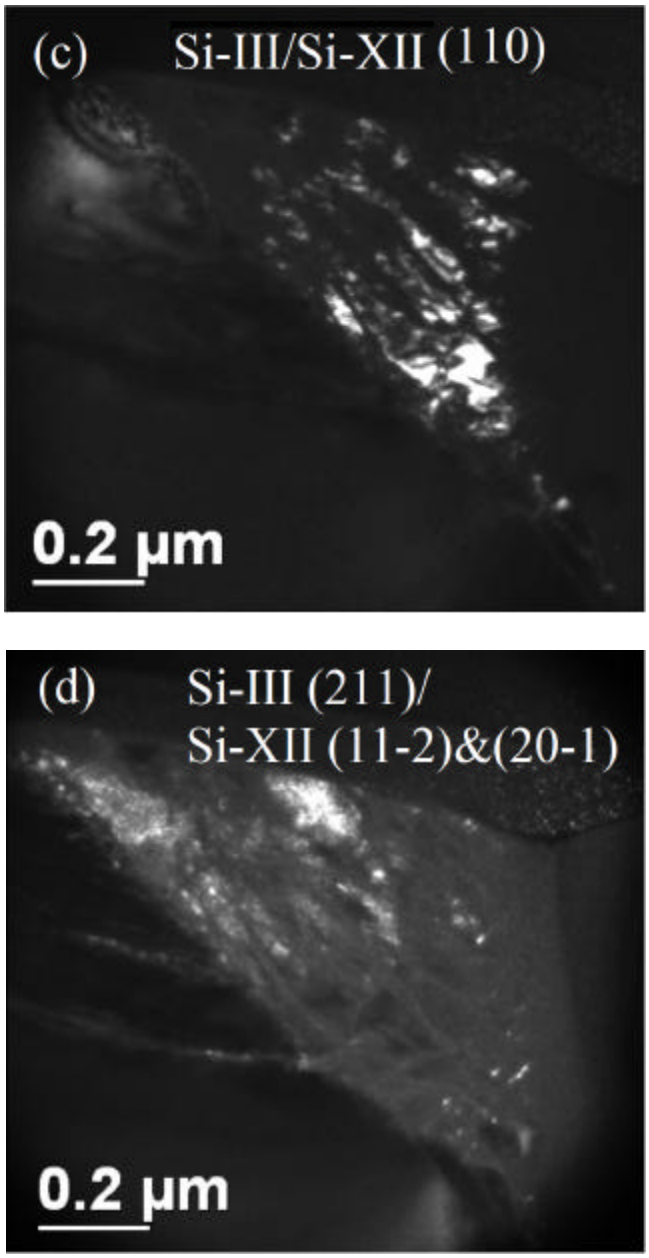

Figure 3. 17 (cont.)

3.1.2.2.2 Cube-corner (35.3°) Indentation

In contrast to the Berkovich indentation, Figure 3. 18a shows that the high-load cube-corner indentation shows extensive extrusion of the transformed material leaving very little remaining within the hardness impression. Since it is the volume change during phase transformation that gives rise to the pop-out event during unloading, the extrusion explains the absence of the pop-out event for the cube-corner indenter (Figure 3. 14a). This is a common feature for the 35.3° cube-corner indenter and is occasionally observed for the 45° indenter. Figure 3. 18 (b) to (d) show detailed TEM images and SAD of the boxed regions on the cross-section. Figure 3. 18b shows a higher magnification BF TEM image of the extruded material on the left side of the indentation together with SAD patterns. One of the SAD's (Figure 3. 18b top) is taken from the apparent extruded material; the other is taken from the wafer matrix. The circles in the BF image designate both the size of the aperture and the area from which the SADs were obtained. It is surprising to see that the SAD from the wafer matrix is about the same as the SAD from the apparent extruded material, with only a few degrees difference in orientation. In Figure 3. 18c, a DF TEM image was taken with a Si-I (111) reflection; therefore, the small crystals that lit up are nanocrystals of Si-I embedded in the transformed material. Figure 3. 18d shows that the extrusion on the right side is mostly amorphous with some small crystals of Si-I flown out (Figure 3. 18d). By comparing the left and right side of the cross-section, the crystalline "extrusion" on the left could very

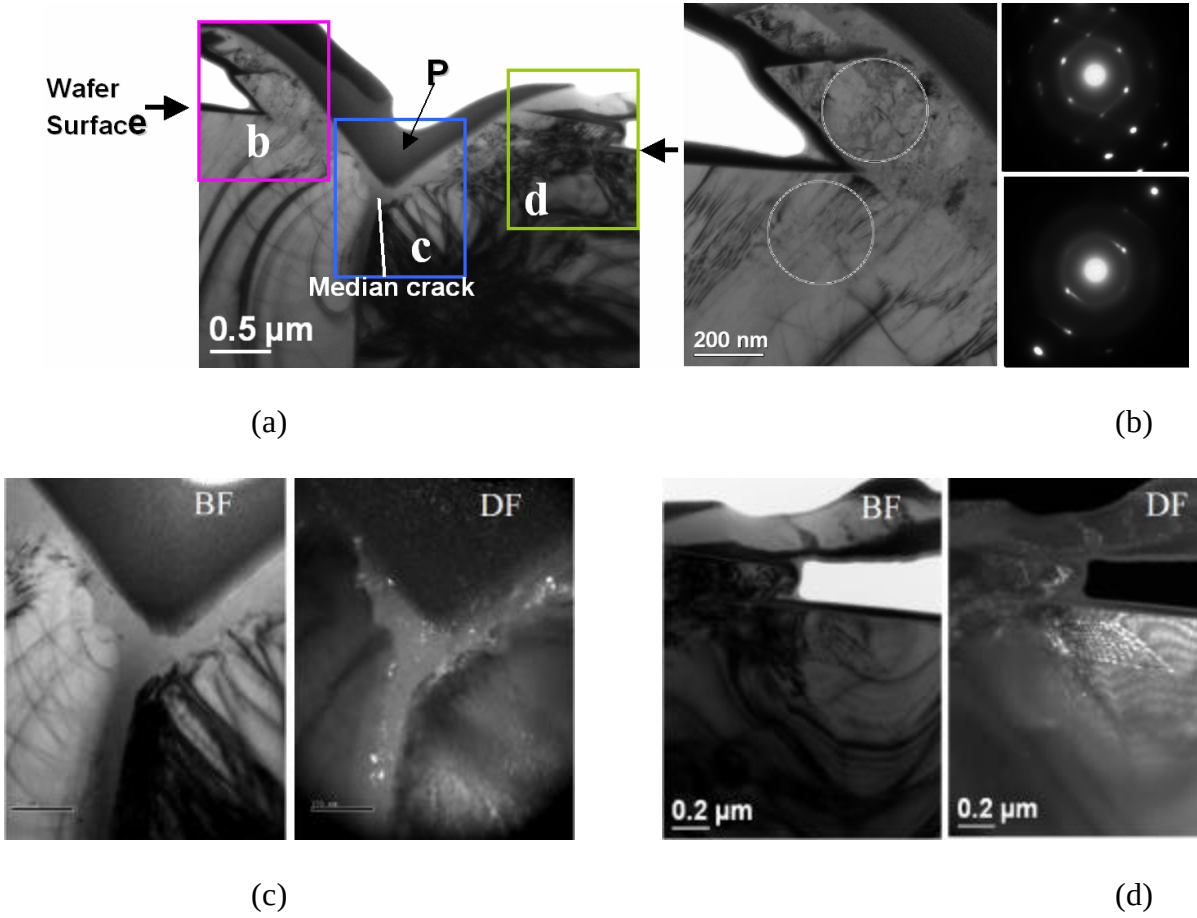

Figure 3. 18 Cube-corner indentation made at 80 mN and 5 mN/s. (a) BF TEM image serves as map for the cross-section, (b) the extrusion on the left side of the cross-section and SADs taken from the circled areas, (c) BF and DF formed by Si-I reflection of the median crack, (d) extruded material on the right side of the cross-section.

much be due to a piece of Si-I that chipped off the matrix material rather than ductile transformed material.

3.1.2.2.3 Extrusion by Sharp Indenters

In order to characterize the extrusion, micro-Ramam maps of the 35° cube-corner indentation made to 50 mN at 5mN/s were constructed using a-Si Raman peak and Si-III and Si-XII Raman peaks. With reference to the SEM plan-view of the indentation (Figure 3. 19a), the Raman maps clearly outline the a-Si phase residing around the indentation where the extrusion is observed in Figure 3. 19c, and the Si-III and Si-XII within the indentation in Figure 3. 19d.

As illustrated in Figure 3. 20, with a sharper indenter, the transformed zone will exceed the contact periphery of the indenter, resulting in ductile high pressure material being extruded out of the indentation. This leaves only a small amount of transformed material under the indenter to promote pop-out during unloading. Another explanation for the extrusion is derived from the observation on the cross-sections of indentations made at various angles, specifically that the shape of the transformed zone can be approximated as having a right angle at the bottom see Figure 3. 4. As the indenter tip approaching 90°, it leaves almost no transformed materials in the residual hardness imprint, producing the excessive extrusion observed from the cube-corner indenter indentation.

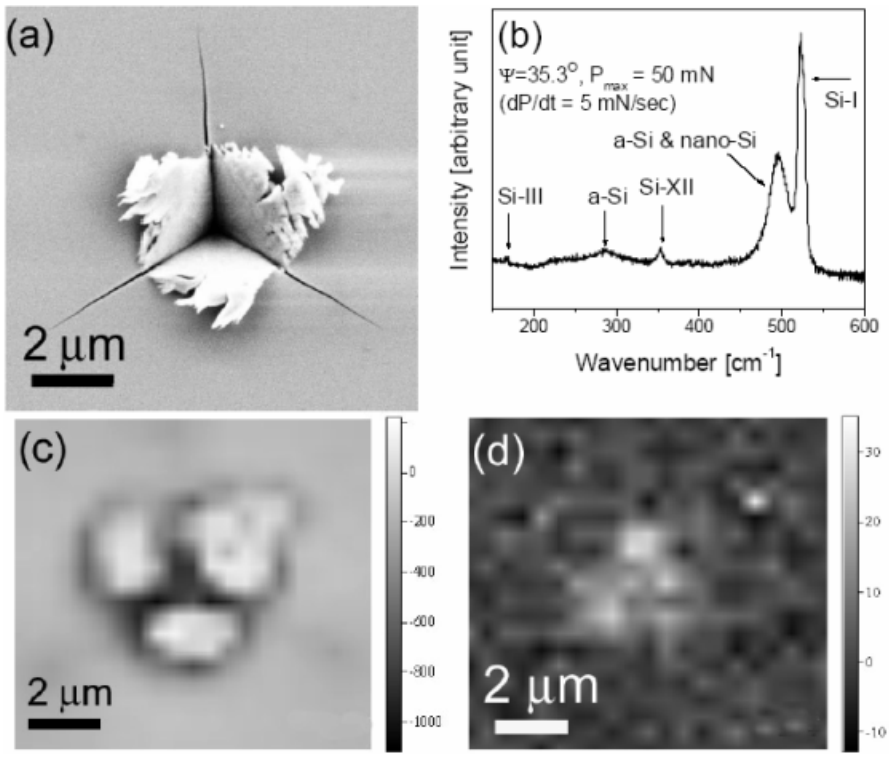

Figure 3. 19 Cube-corner (35°) indentation made at 80 mN at 5 mN/s (a). Plan-view SEM showing the extruded material, (b). Ramam spectrum indicates the presence of a-Si, Si-III and Si-XII in the indented region. Note that the Si-I peak is mostly from the pristine Si, (c). Raman map constructed using a-Si peak showing the a-Si resides at where the extrusion being observed (light area around the indentation), (d). Ramam map constructed using Si-III and Si-XII peaks showing Si-III and Si-XII mostly exist within the indentation (high lighted area in the center).

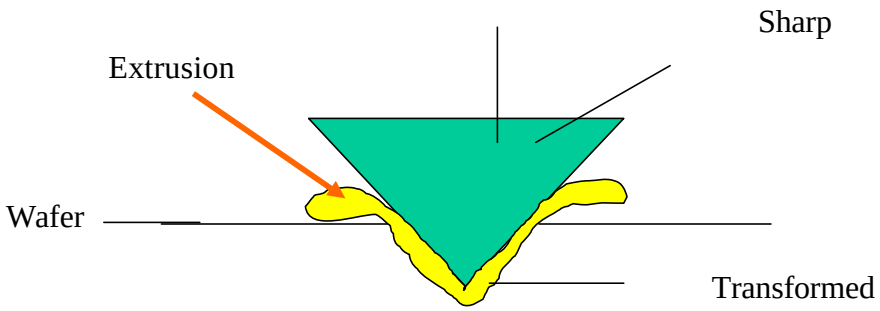

Figure 3. 20 Schematic of extrusion by cube-corner indenter.

3.1.3. Rate Effects at Low Load

The influence of loading/unloading rate on pop-out behavior was studied at peak loads near 10 mN, where pop-out is not observed at high rates. Unloading rates of 5, 0.5 and 0.05 mN/s were examined. P-h curves of indentations made to a peak load of 13 mN are shown in Figure 3. 2 (in section 3.1.2), and P-h curves of 10 mN indentations made at 0.5 and 0.05 mN/s are shown in Figure 3. 21 and Figure 3. 22, respectively. The 75.0° indentation showed no pronounced change in the unloading curves regardless of the rate applied. The 85.0° indentations demonstrated purely elastic behavior at all rates. The intermediate angles, 45.0°, 55.0° and 65.3° (Berkovich) behave similarly: no pop-out observed for the fast rate 5 mN/s, but occasionally pop-out for the moderate (0.5 mN/s) and slow (0.05 mN/s) rates. As for the sharp 35.3° (cube-corner) indenter, no pop-out was observed at all rates.

A special microstructural study was carried out through TEM on the cross-sections of indentations made with a Berkovich indenter to10 mN peak load at rates of 5 mN/s and 0.05 mN/s. The study correlates pop-out behavior to the phase(s) composition and deformation structure of indentations with and without pop-out. The indentation results shown that 5 mN/s unloading rate does not usually produce pop-out at the 10 mN peak load. The microstructure of a indentation made under this condition presented in Figure 3. 10 shows a “clean” and uniform transformed zone that is mostly amorphous with some crystalline

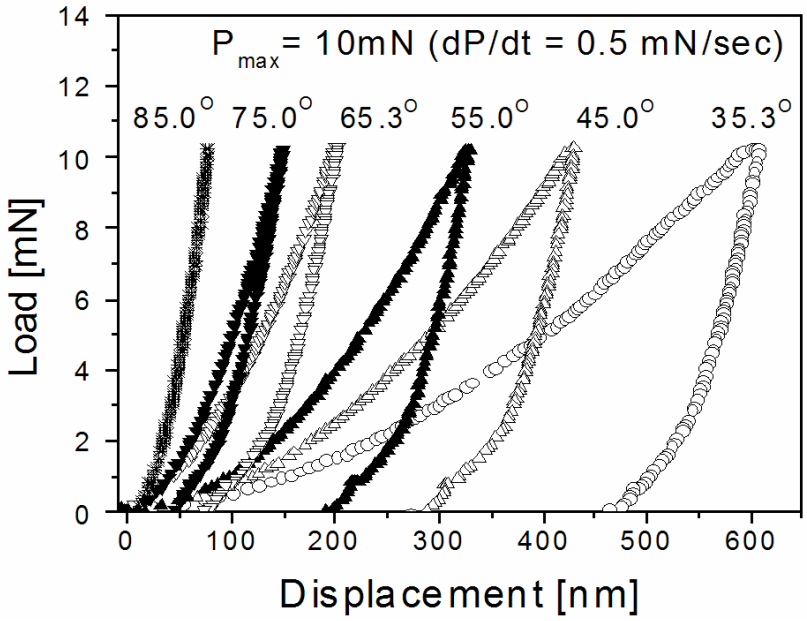

Figure 3. 21 Typical P-h curves of 10 mN peak load indentations made with varies indenters at the fixed 0.5 mN/s rate

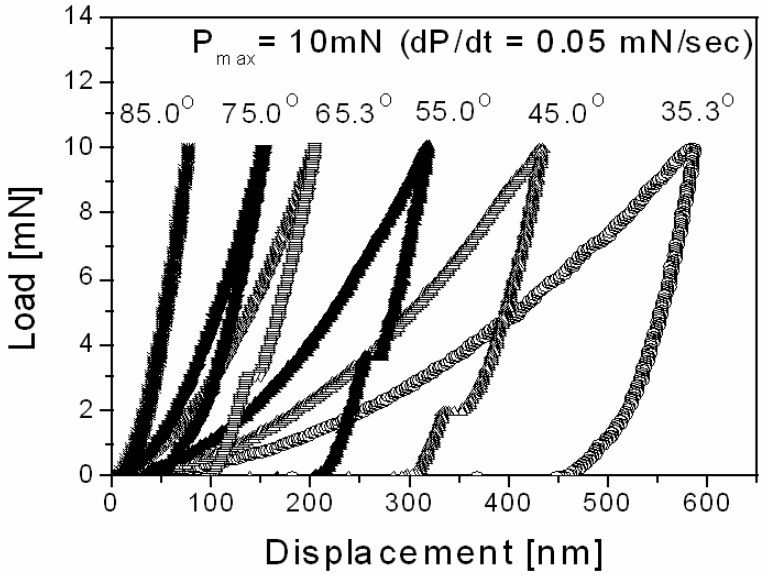

Figure 3. 22 Typical P-h curves of 10 mN peak load indentations made with varies indenters at the fixed 0.05 mN/s rate

material near the bottom of the zone and adjacent to amorphous-crystalline (a-c) interface.

On the other hand, the pop-out behavior of indentations made at 0.05 mN/s is diverse; detailed statistic showed that there is about a 50% chance for pop-out to occur at this rate. Therefore, indentations that exhibited pop-out and indentations that produced no pop-out were carefully selected by their distinguishable P-h curves. Three cross-sectional samples were examined for each case to ensure repeatability.

Cross-sectional TEM BF and DF images of the three indentations with no pop-out are shown in Figure 3. 23. The SADs from which the DF TEM images were acquired are inserted. TEM observation on all three samples showed no crystalline phase except Si-I was present in the transformed zone. The zone is largely composed of a- Si and a small amount of nanocrystalline Si-I. Most of the Si-I nanocrystals apparently had grown into the zone from the a-c boundary in an epitactic manner with a few nanocrystals scattered in the zone. It should be noted that due to the beam artifacts on the FIB sections, the origin of this Si-I material in the transformed zone is uncertain.

Included in Figure 3. 24 are BF and DF TEM images of the indentations that did show pop-out during unloading. The diffraction contrast of the material indicates that the transformed zone is predominantly crystalline. The inserted SAD patterns taken from the transformed region show weak diffuse amorphous rings and reflections of Si-I in all three samples and Si-III/Si-XII in samples #1 and #3. The DF image taken with a Si-III/Si-XII reflection shows the Si-III/Si-XII crystals of the orientation exist throughout the zone.

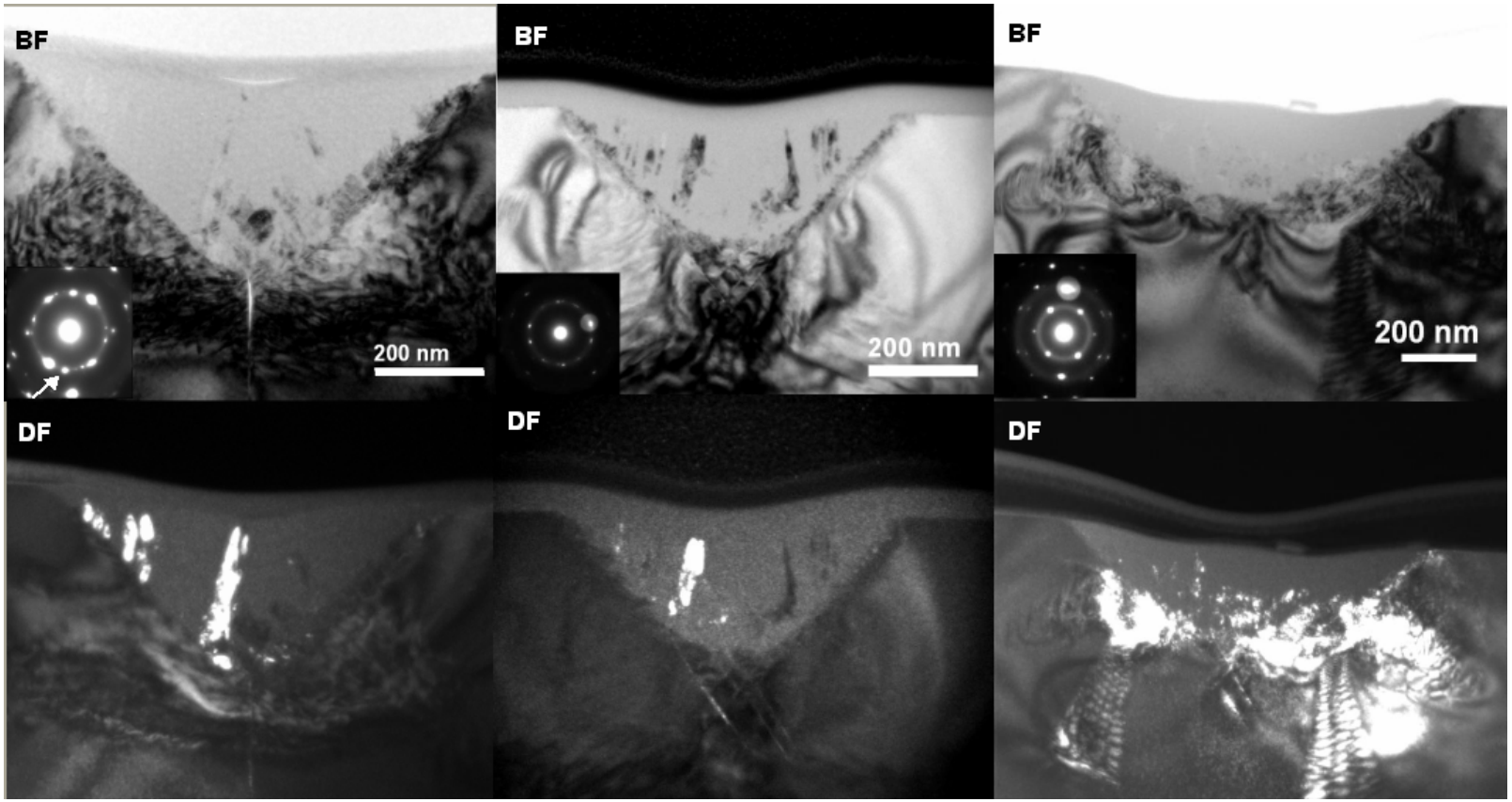

Sample #1 Sample #2 Sample #3

Figure 3. 23 BF, DF and SAD of the 10 mN Berkovich indentation made at 0.05 mN/s did not show pop-out.

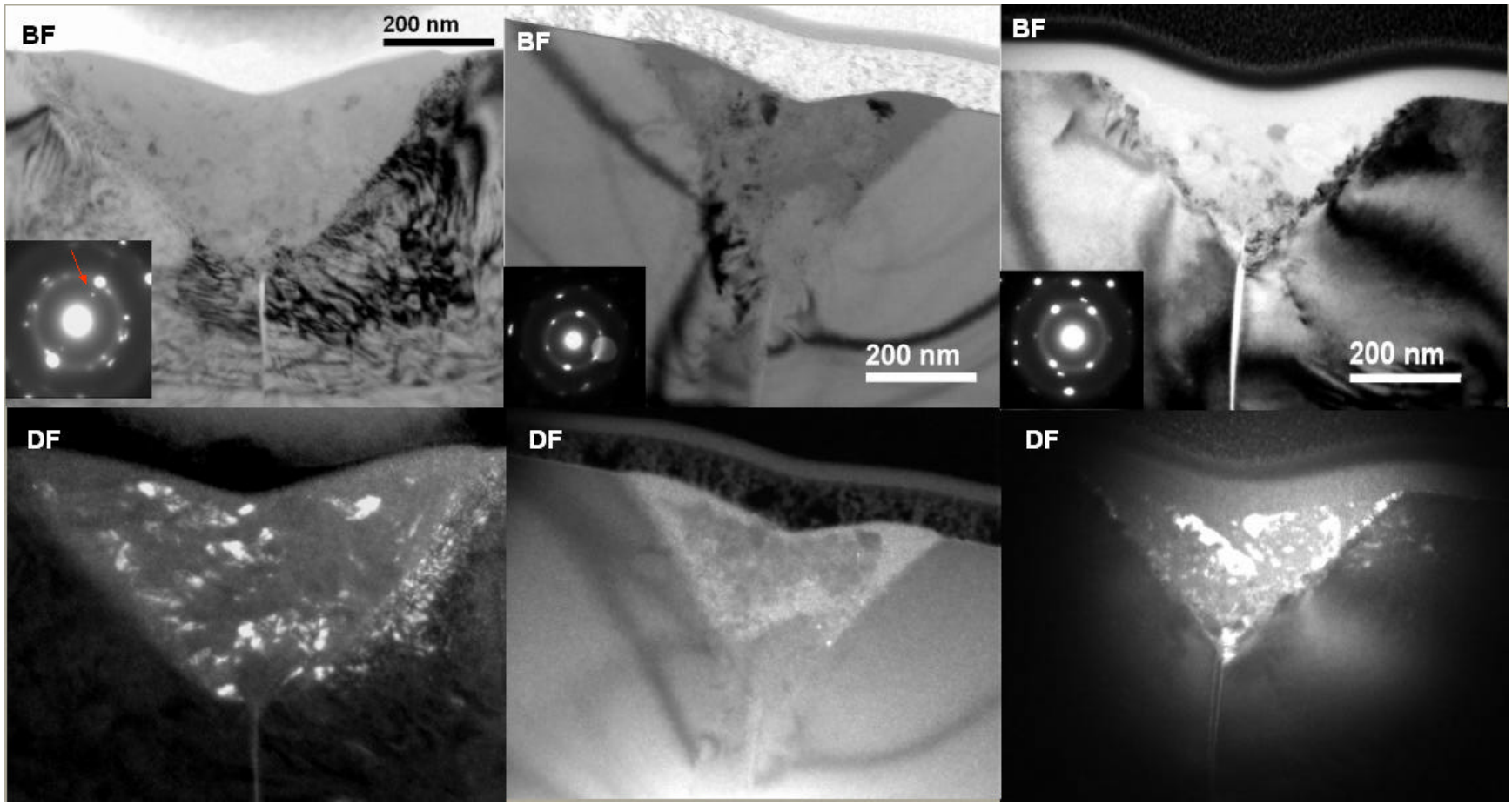

Sample #1 Sample #2 Sample #3

Figure 3. 24 BF, DF and SAD of the 10 mN Berkovich indentation made at 0.05 mN/s show pop-out.

The Si-III/Si-XII crystals also show some preferred orientation, similar to the 80 mN Berkovich indentation examined, since the reflections are a primary spot pattern instead of diffuse rings. Observation on sample #2 under this condition indicated a transformed zone of mixed crystalline Si-I and a-Si. SAD taken over the transformed zone gives a clear pattern of Si-I and very diffuse rings of Si-I. No Si-III/Si-XII was detected by the TEM observation for this sample. With the aperture imposed on the diffuse ring, the DF TEM image of sample #2 in Figure 3. 24 was formed to outline the a-Si in the transformed zone. It is seen that a-Si is residing at the outer boundary of the transformed zone. Some Si-I nanocrystals are also lit up through out the zone in this DF image due to two of the Si-I (111) type of reflections creeping in the aperture.

It is worth mentioned that sample #3 demonstrated a transformed zone containing Si-III/Si-XII during the initial TEM observation, however, the Si-III/Si-XII reflections disappeared after a couple of hours exposure under the electron beam. This serves another supporting evidence on beam damage of the cross-sections.

In summary, all three samples exhibiting pop-out demonstrate a transformed zone that is mostly crystalline, with two of the three showing a mixture of primary Si-I and Si-III/Si-XII and small amount of a-Si, and the third showing polycrystalline Si-I and a-Si.

Figure 3. 25 provides a comprehensive comparison of the indentation P-h curves, TEM BF and DF images, and SAD for fast unloading (5 mN/s), slow unloading (0.05 mN/s) without pop-out and slow unloading with pop-out. The correlation between pop-out and crystalline phase formation is confirmed through this observation.

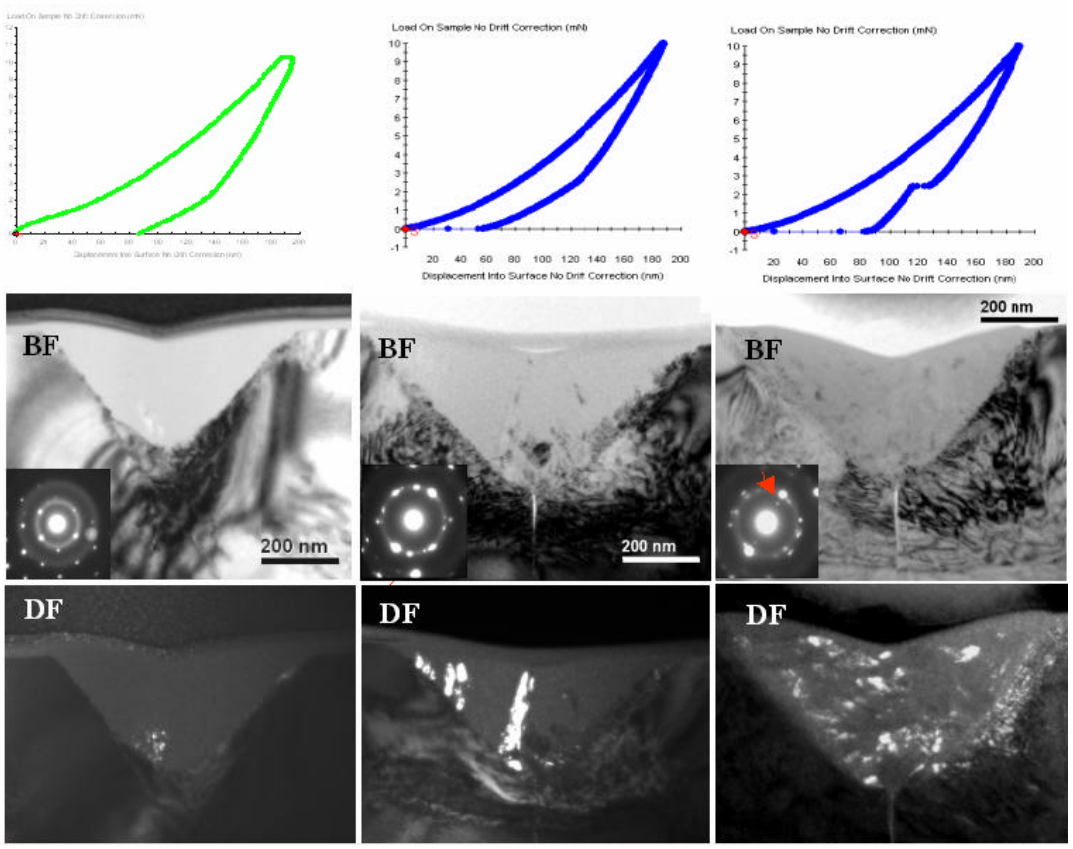

Figure 3. 25 Indentation P-h curve, BF and DF TEM images for (a) 10 mN Berkovich indentation made at 5 mN/s, (b) 10 mN Berkovich indentation made at 0.05 mN/s that did not show pop-out, (c) 10 mN Berkovich indentation made at 0.05 mN/s that did show pop-out.

3.2 A Kinetic Study of Indentation Pop-out Using the Berkovich Indenter

3.2.1 Systematic Indentation Pop-out Study using the Berkovich Indenter

In this study, single crystal Si (100) wafers were indented using the Berkovich (65.3°) indenter to peak loads of 10, 30, 50, 80 and100 mN to systematically characterize the kinetics of indentation pop-out. Indentation unloading rates of 0.05, 0.5, 2, 5 and 20 mN/s were used at all peak loads, with the exception of the 10 mN indents, which were only indented up to 5 mN/s. The unloading portion of the P-h curves was carefully examined for pop-out behavior. Examination results, such as the pop-out occurrence and pop-out load, were recorded. Under each condition, one hundred indentations were made to ensure statistically accurate results of mean pop-out load under each indentation condition.

Table 3- 1 summarizes the nanoindentation test conditions, the mean pop-out load with standard deviation, number of tests and number of pop-outs observed under each indentation condition. A plot of the mean pop-out load versus peak load for all conditions is shown in Figure 3. 26. A plot of the mean pop-out load versus unloading rate for all conditions is shown in Figure 3. 27. From this statistical evaluation, it is obvious that with the Berkovich indenter, the load at which pop-out takes place is directly related to the peak load and unloading rate. For a given peak load, the faster the unloading rate, the lower pop-out load will be. This suggests that the mechanism for pop-out is time dependent and therefore possibly thermally activated. One such process that could explain this behavior is thermally activated nucleation and growth of Si-XII/III from the pressurized Si-II that exists at peak load. The process we envision is one in which

Table 3- 1 Summary of results of systematic Indentation test with the Berkovich indenter.

Pmax (mN)	dP/dt (mN/s)	Avg. Ppop-out	Std Div.	# of Test	# of Pop-out
100	20	28.7	9.1	100	97
	5	36.6	10.2	100	100
	2	46.7	12.3	100	100
	0.5	50.2	11.0	100	100
	0.05	53.2	10.1	100	100
80	20	22.2	6.7	99	97
	5	30.0	5.0	100	97
	2	35.9	6.3	100	100
	0.5	42.5	6.3	100	100
	0.05	43.3	6.8	98	98
50	20	2.7	5.3	100	24
	5	10.0	5.5	100	83
	2	13.6	5.1	100	97
	0.5	16.9	4.6	100	100
	0.05	18.6	4.6	100	100
30	20	0.6	2.0	100	8
	5	2.8	3.5	100	46
	2	4.4	3.9	100	67
	0.5	6.8	3.6	100	89
	0.05	8.6	2.5	100	99
10	5	0.1	0.4	100	5
	2	0.1	0.5	100	6
	0.5	0.3	0.7	100	17
	0.05	0.8	1.0	100	45

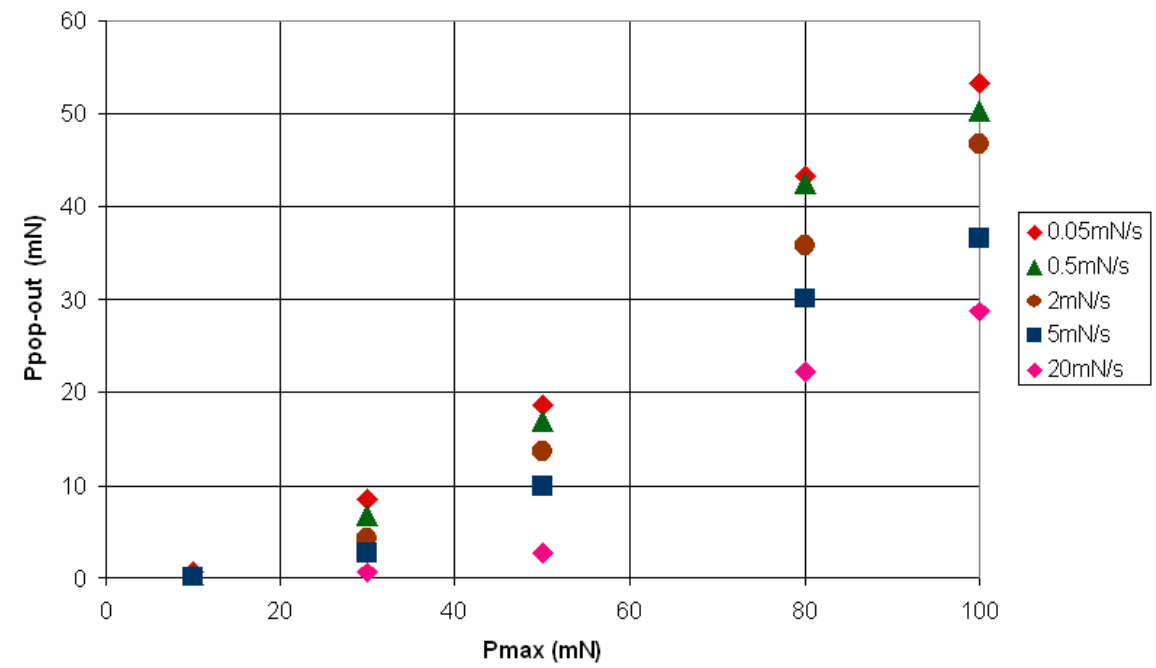

Figure 3. 26 Maximum pop-out load vs. indentation peak load.

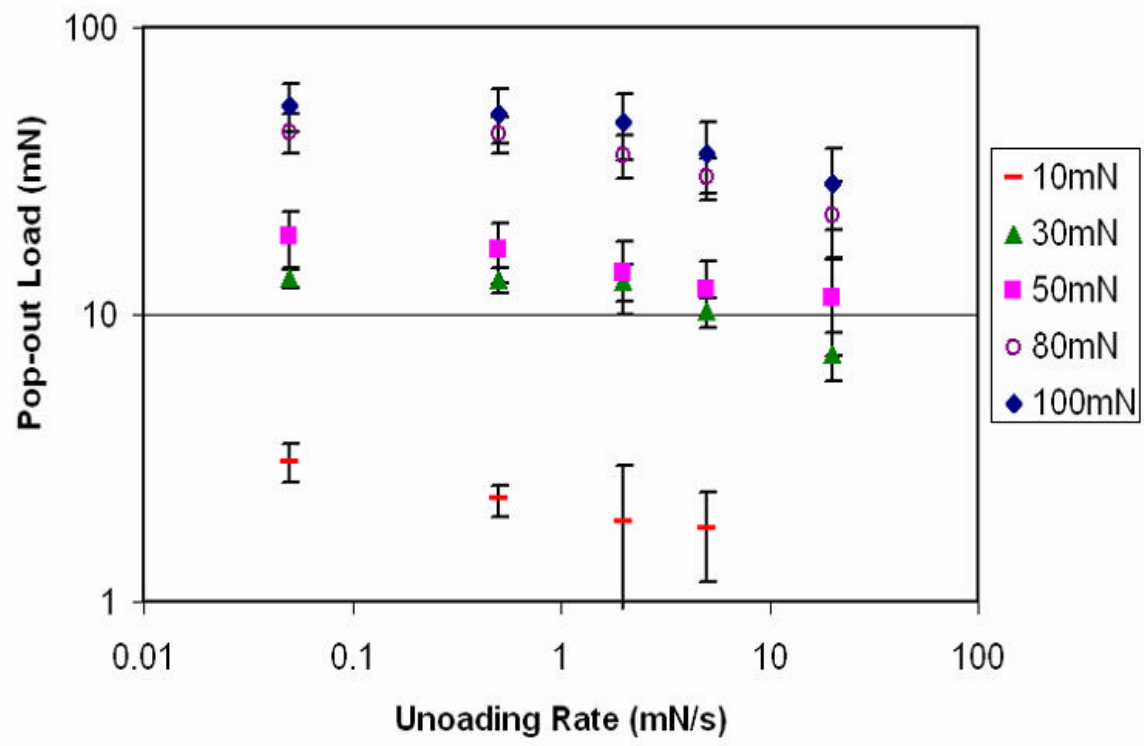

Figure 3. 27 Mean Pop-out load as vs. indentation unloading rate.

nucleation is that rate controlling step. After one critical nucleus is formed, the growth process is very rapid; therefore completion of phase transformation takes a very short period of time. As a result, pop-out is a very sudden event, taking place over a very short period of time. For low peak loads, pop-out rarely occurs unless the unloading rate is very slow (0.05 mN/s) (see both in Table 3- 1 and Figure 3. 27). This is not surprising since the 10 mN peak load produces a very small transformed zone for the nucleation of the new phase, and therefore, a much smaller nucleation rate. Thus, pop-out (phase transformation) does not take place during the low load indentation unless enough time (slow rate) is provided.

3.3.2 Temperature Effects on Indentation Pop-out using the Berkovich Indenter

To examine temperature effects on pop-out, the Si (100) wafer was also indented using the Berkovich indenter at 45°C in addition to the room temperature tests (T=25°C). The 45°C indentations were made in a conventional Nanoindenter XP, with temperature of the indentation chamber being controlled by a electrical heating lamp and fan. Indentation tests were not started until the temperature had been stabilized for over 24 hrs. The temperature sensitivity of the indentation system was carefully calibrated as a function of test temperature to ensure indenter performance.

Table 3- 2 shows the mean pop-out load for 25°C and 45°C 100 mN peak load data. By comparing the mean pop-out load between the two test temperatures, it is clear that increasing the temperature leads to a higher pop-out load for a given unloading rate, which compensates to pop-out in a shorter period of time. Thus, increasing temperature

Table 3- 2 Mean pop-load for various unloading rate at 25°C and 45°C.

	Pop-out Load (mN)			
Temperature (°C)	0.5 mN/s	2 mN/s	5 mN/s	20 mN/s
25	50.2	46.7	36.6	28.7
45	53.8	50.3	45.7	35.9

increases the rate at which pop-out occurs, as would be expected in a kinetic process controlled by nucleation and growth.

3.2.3 Step Unload Indentation Using the Berkovich Indenter

In addition to the conventional constant loading/unloading rate ($\dot{P}$) tests, step unload tests were also conducted to examine the time dependence of pop-out. The step unload amount during these tests was set at certain percentage of the peak load, ranging from 25% to 90%. The peak loads selected for study were 10, 30 and 100 mN. After the step unloading, the indenter was then held on the surface for 30 minutes duration, and displacement was monitored to identify time-delayed pop-out. Regardless of peak load, the one step unload took less than a second. Figure 3. 28 illustrates the loading history during the step unload test. Pop-out was identified as a sudden decrease of displacement indicating that the surface is suddenly lifted up by the reverse transformation. In general, less waiting time was required for pop-out to occur as the percentage unload increases and/or peak load increases. Pop-out was observe to occur instantaneously when the amount of the unload was large.

The 10 mN peak load tests yielded no pop-out during the 30 min holding period for all percentage step unload indentations. The waiting time for pop-out in step unload indentation tests from 30 mN and 100 mN peak loads are plotted in Figure 3. 29 and Figure 3. 30 respectively. For step unloads from 30 mN, it was not until the load was reduced to 50% or more that when pop-out started to occur during holding. At 75% step

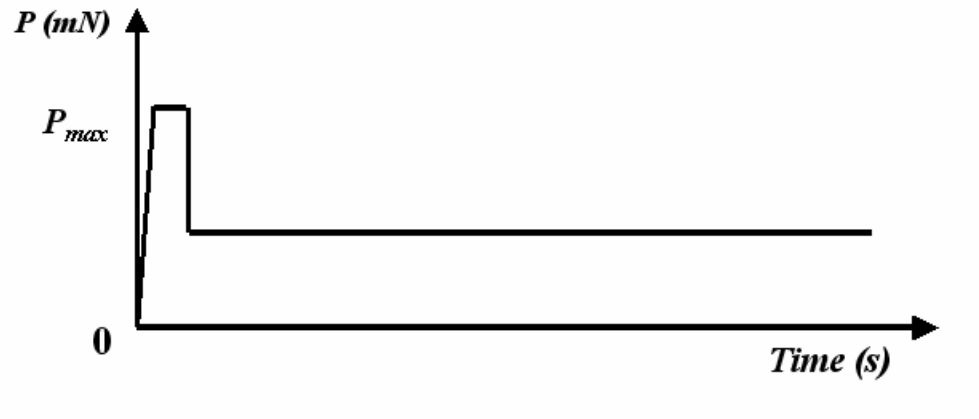

Figure 3. 28 Schematic of the loading history during step unload indentation.

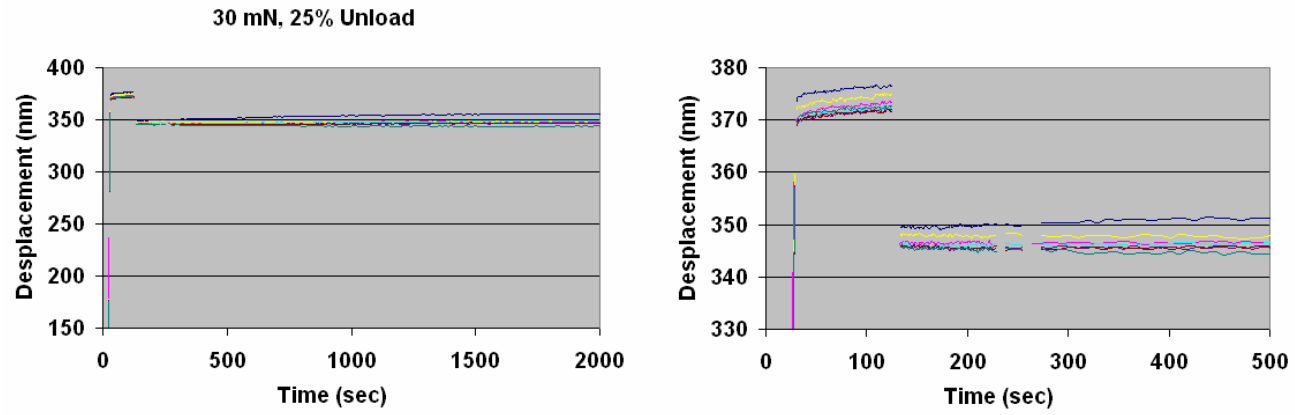

(a)

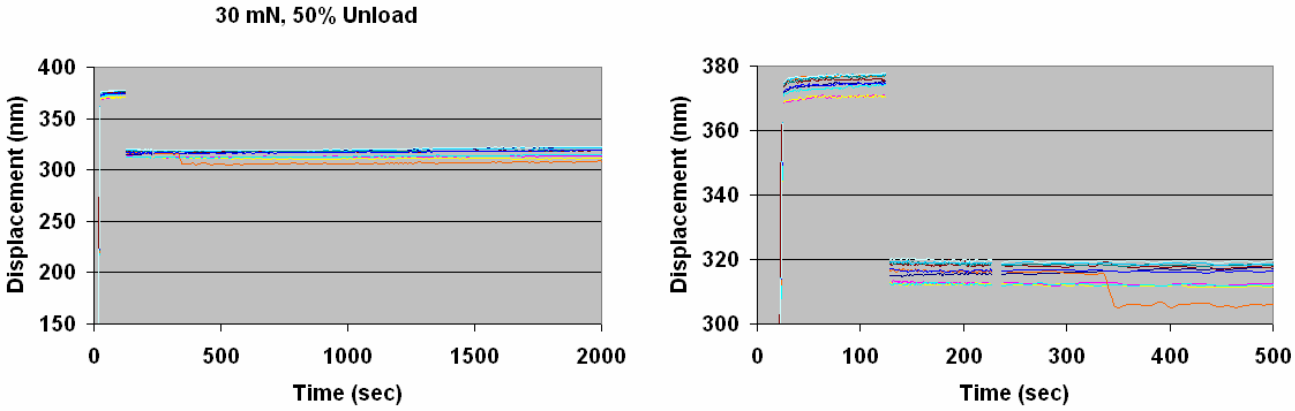

(b)

Figure 3. 29 Displacement change over waiting time during step unload tests from 30 mN peak loads at various percentage unload: (a) 25%, (b) 50%, (c) 75% and (d) 90%. The figures on the right are detail of the behavior over the first 500 seconds.

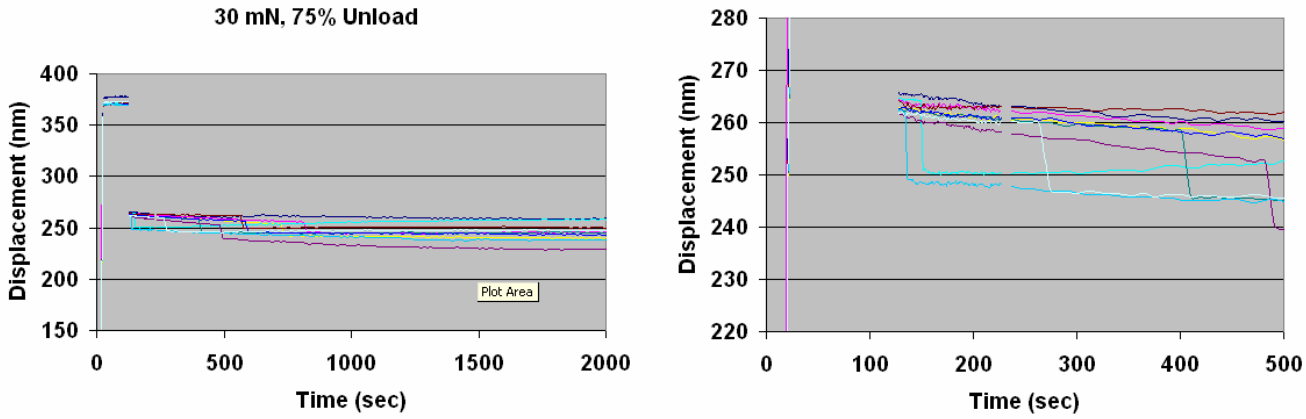

(c)

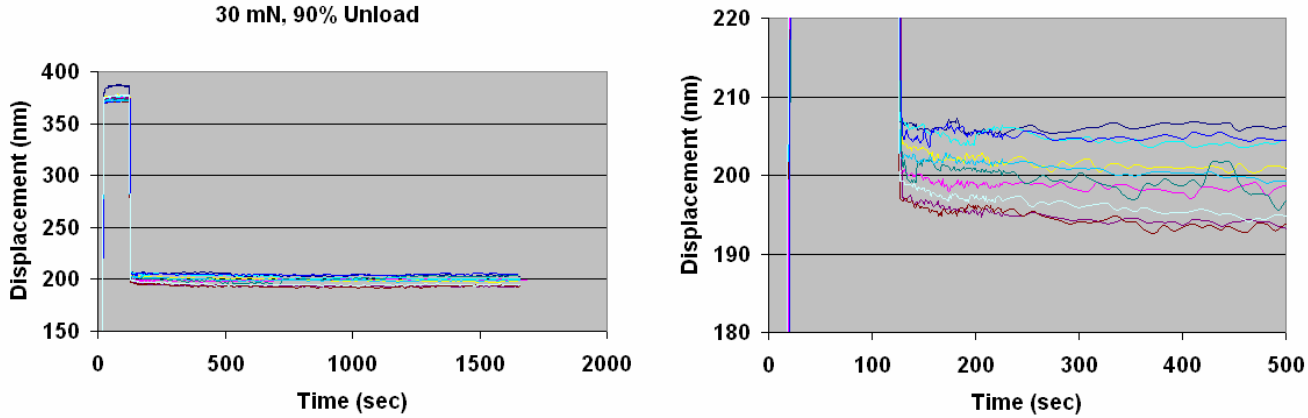

(d)

Figure 3. 29 (Cont.)

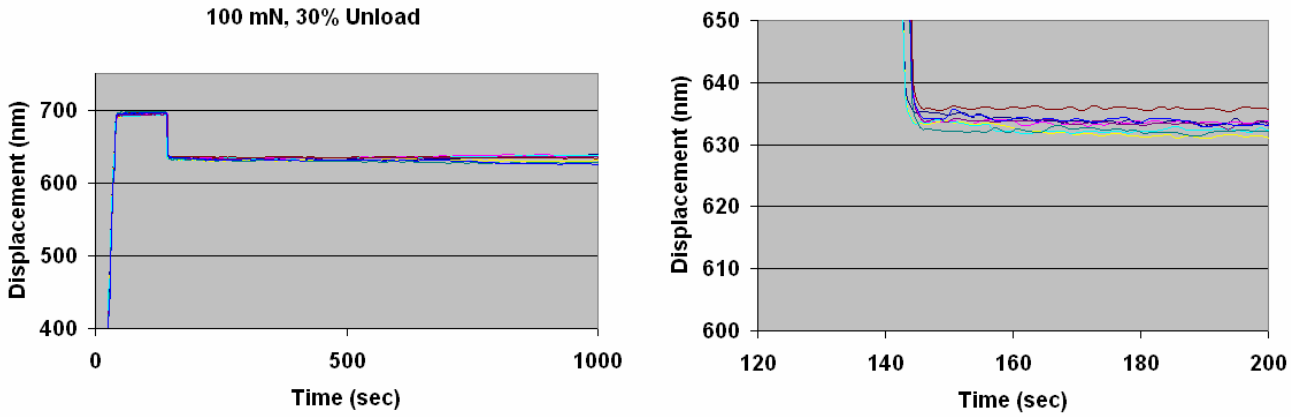

(a)

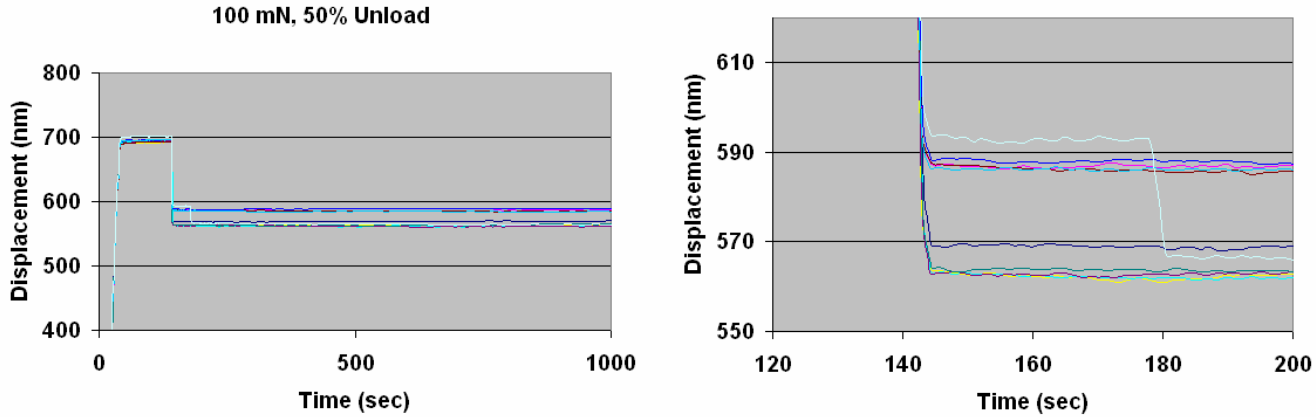

(b)

Figure 3. 30 Displacement change over waiting time during step unload test from 100 mN peak loads at various percentage unload: (a) 30%, (b) 50%, (c) 75% and (d) 85%. The figures on the right are detail of the behavior over the first 200 seconds.

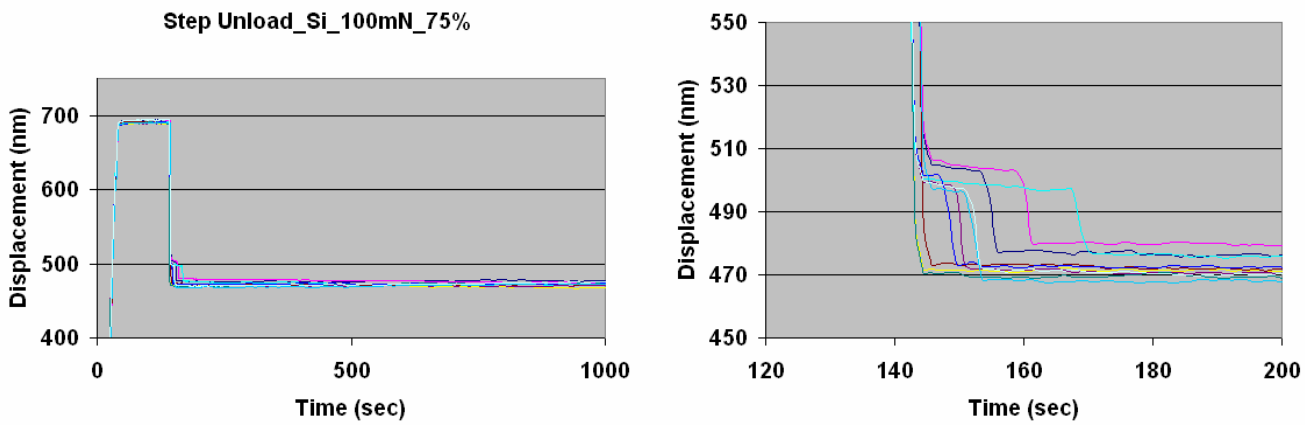

(c)

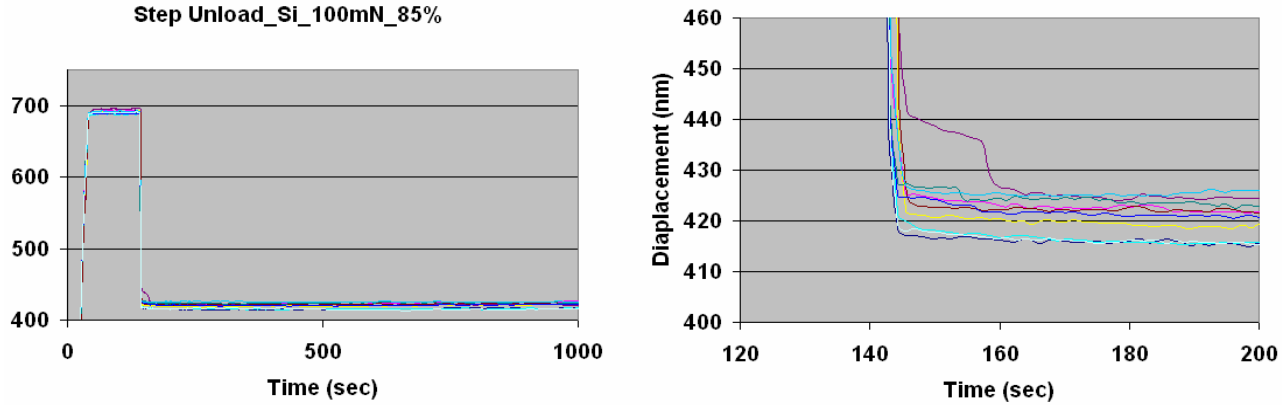

(d)

Figure 3. 30 (Cont.)

unload, most of the tests indicated pop-out during holding after various waiting times. After 90% step unload from 30 mN, all indentations demonstrated instantaneous pop-out. For the 100 mN peak load test, the same trends were observed except that the required percentage unload needed for pop-out was less than that of the 30 mN tests.

Table 3- 3 and Table 3- 4 summarizing the step unload observations for peak loads of 30 mN and 100 mN, respectively. The percentage of pop-out and the number of instantaneous pop-outs are listed in the tables. It is clear from the data that pop-out is a time-dependent phenomena that depends on the peak load achieved and the amount of step unloading. Shorter pop-out times are produced by a higher peak load and greater percentage step unload.

Table 3- 3 Summary of the 30 mN peak load step unload tests.

% Unloaded	# of Tests	# of Pop-outs	% of Pop-out	# of Instantaneous Pop-out
25%	7	0	0	0
40%	8	0	0	0
50%	20	2	10%	0
60%	20	1	5%	0
65%	10	1	10%	0
70%	20	14	70%	0
75%	10	9	90%	0
80%	10	9	90%	0
85%	10	7	70%	2
90%	20	20	100%	20

Table 3- 4 Summary of the 100 mN peak load step unload tests.

% Unloaded	# of Tests	# of Pop-outs	% of Pop-out	# of Instantaneous Pop-out
30%	20	6	30%	0
40%	20	9	45%	0
50%	20	13	65%	6
60%	19	14	74%	8
75%	20	20	100%	9
85%	10	10	100%	9

IV Indentation Pop-out Modeling

The experimental results presented here demonstrate the pop-out tends to take place at large indentation loads, slow unloading rates, and intermediate indenter angles. A mechanistically-based model is now developed based on the assumption that pop-out corresponds to homogeneous nucleation of the low pressure crystalline form from the high pressure phase. The goal is to qualitatively predict all the experimentally observed behaviors and give a quantitative estimate of how the pop-out load should vary with the major experimental variables.

4.1 Indentation Pop-out Model

4.1.1 Proposed Mechanism

The proposed mechanism for modeling pop-out is illustrated in Figure 4. 1. When the indenter penetrates the surface, the material under the indenter tip transforms into Si-II (β-Sn). Upon unloading at a slow unloading rate, the phase Si-II will transform to crystalline Si-XII (r8)/Si-III (bc8) by nucleation and growth process, whereas at fast unloading rate, the material will go amorphous according to the structural frustration argument. We assume that nucleation of the new phase is homogenous, but noted heterogeneous is likely. However, the level of complication of heterogeneous nucleation is beyond capability of our modeling effort.

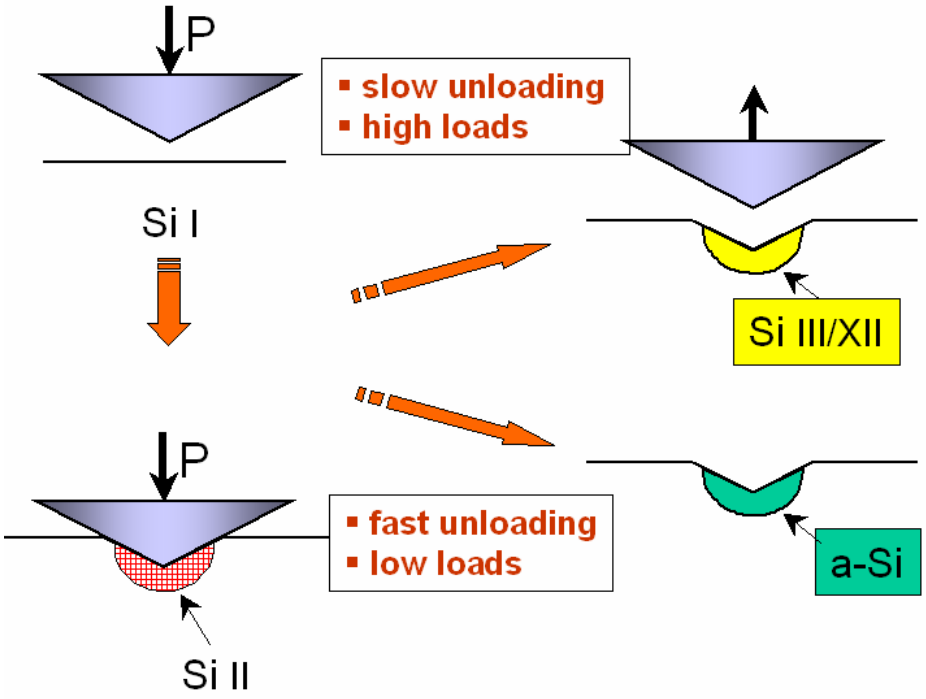

Figure 4. 1 Proposed mechanism for modeling indentation pop-out in Si.

When a nucleus of Si-XII forms homogenously within the transformed zone made of Si-II (or a-Si) and reaches the critical size, transformation from high pressure phase (Si-II or a-Si) to the low pressure crystalline form will be triggered. For the small volume of material in the transformed zone rapid transformation into the new phase(s) will be achieved when one nucleus reaches the critical size. Figure 4. 2 is an illustration of nucleation within the transformed zone.

According to homogenous nucleation theory, the radius of the critical nucleus, r^*, is determined by the volumetric change of free energy ΔG and the surface energy γ, according to the simple relationship:

$$r^* = -\frac{2g}{VG_v} \tag{4.1}$$

The total free energy change for the critical nucleus is,

$$VG^* = \frac{16p}{3} \cdot \frac{g^3}{(VG_v)^2} \tag{4.2}$$

The nucleation rate is then

$$\dot{N} = N_{sites} \cdot R \cdot \exp(\frac{-\Delta G^*}{kT}) \tag{4.3}$$

where N_{sites} = number of nucleation sites $= \frac{V}{\Omega}$, V is the volume of the transformed zone, Ω is the atomic volume (determined by atomic weight and density), and R is the rate of attachment.

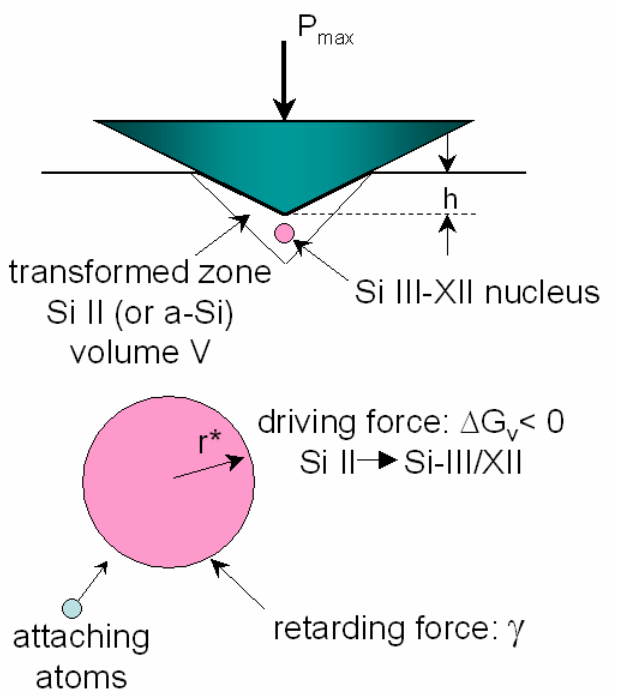

Figure 4. 2 Illustration of critical nucleation within the transformed zone.

In order to calculate nucleation rate, it is necessary to determine the volume of the transformed zone (V), the critical free energy (VG^*) and the rate of attachment (R).

4.1.2 Volume of the Transformed Zone

From the TEM cross-sectional observations, the size of the transformed zone is largely determined by the indenter geometry. Based on the observation of TEM cross-sections for the various indenter angles shown in Figure 3. 4 in section 3.1.2.1, the transformed zone can be approximated by a cone with an apex of 90°. The amount of material in the zone thus depends on the angle of the indenter. With this assumption, the volume of the transformed zone can be calculated for various indenters using the geometries in Figure 4. 3 as

$$V = \frac{1}{3} p a^2 (l - h) \tag{4.4}$$

where

a: contact diameter, $a = \sqrt{\frac{P_{\max}}{p H}}$

h: depth of plastic penetration, $h = a \cos j$

l: depth of the transformed zone, $l = a$

or using the definition of hardness $H = \frac{P_{\max}}{p a^2}$

$$V = \frac{p}{3} \cdot \left(\frac{P_{\max}}{p H} \right)^{\frac{3}{2}} \cdot (1 - \cot j) \tag{4.5}$$

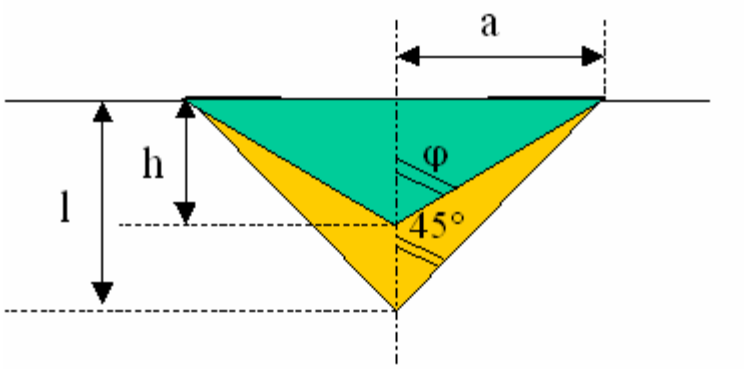

Figure 4. 3 Schematic of the geometry of transformed zone relative to the indenter tip angle.

4.1.3 Critical Free Energy

At the pressure at which the high pressure phase (assuming Si-II) and the low pressure phase (assuming Si-XII) are in equilibrium, the free energy of the two phases are equal. This is illustrated in Figure 4. 4, which shows that at the equilibrium pressure

$$G_{Si\text{-}XII} = Gs_{i\text{-}II,} \tag{4.6}$$

Since

$$G=H - TS = E+pV-TS \tag{4.7}$$

we may write the equilibrium condition as follows

$$Es_{i\text{-}II} + p_e Vs_{i\text{-}II} - TSs_{i\text{-}II} = E_{Si\text{-}XII} + p_e V_{Si\text{-}XII} - TS_{Si\text{-}XII} \tag{4.8}$$

Re-arranging yields:

$$(E_{Si\text{-}XII} - Es_{i\text{-}II}) + p_e(V_{Si\text{-}XII} - Vs_{i\text{-}II}) - T(S_{Si\text{-}XII} - Ss_{i\text{-}II}) = 0 \tag{4.9}$$

or in terms of changes in the thermodynamic quantities

$$\Delta G = \Delta E + p_e\Delta V - T\Delta S = 0 \tag{4.10}$$

This then shows that at the equilibrium pressure

$$\Delta E - T\Delta S = - p_e\Delta V \tag{4.11}$$

An important assumption is now made that ΔE and ΔS are not strong functions of pressure; therefore ($\Delta E - T\Delta S$) can be regarded as the same for p and p_e, and

$$\Delta G\ (p=p) = (p- p_e)\Delta V \tag{4.12}$$

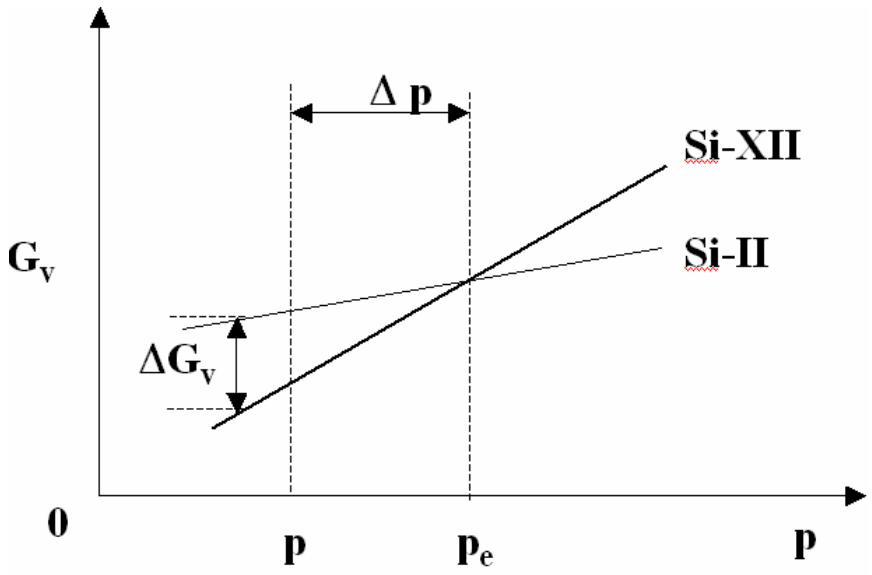

Figure 4. 4 Volume free energy as a function of pressure for Si-II and Si-XII system.

where ΔV is the volume change at equilibrium pressure.

When the transformation of Si-II to Si-XII takes place at a pressure below the equilibrium pressure $p_{e,}$ and the free energy change is negative, ΔG < 0. The volumetric change in Gibbs free energy at p is then

$$\Delta G_v = (p - p_e) \cdot f_v = -\Delta p \cdot f_v \tag{4.13}$$

where f_v is the change in volume $f_v = \frac{(V_{Si-XII} - V_{Si-II})}{V_{Si-II}}$. Using the volume-pressure data in Figure 1. 2, f_v for Si-II to Si-XII transformation can be estimated

$$f_v = \frac{V_{Si-XII} - V_{Si-II}}{V_{Si-II}} \approx \frac{0.93 - 0.72}{0.72} \approx 15\%. \tag{4.14}$$

Using this in combnation with equation 4.2, the critical free energy for nucleation is

$$\Delta G^* = \frac{16p}{3} \cdot \frac{g^3}{(\Delta G_v)^2} = \frac{16p}{3} \cdot \frac{g^3}{(f_v \Delta p)^2} \tag{4.15}$$

4.1.4 Rate of Attachment

Consider that the atoms around a nucleus form a shell like schematically shown in Figure 4. 5. As the atoms vibrate to attach and detach from the nucleus, the net rate of attachment is equal to the number of atoms around the nucleus times the rate times the probability of successful attachment, that is

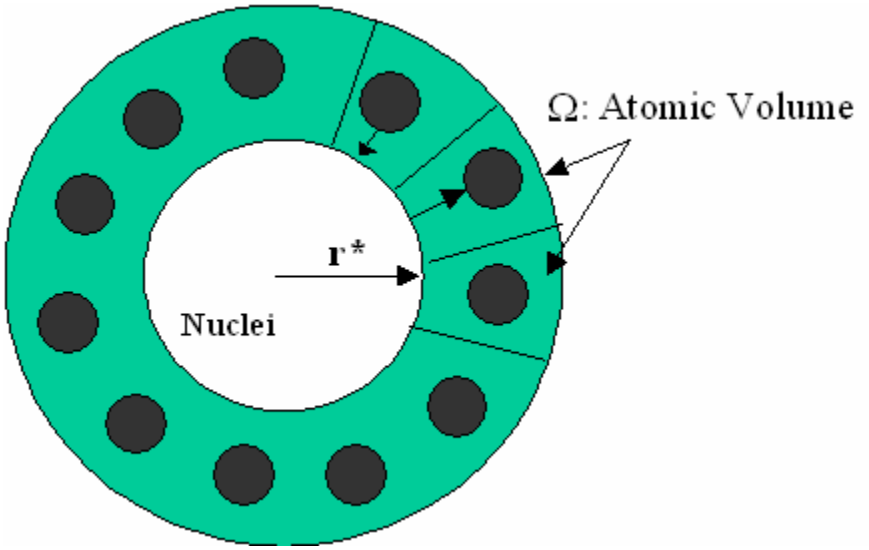

Figure 4. 5 Illustration of atoms attaching to the critical nucleus.

R = # atoms around nuclei × attachment attempt rate × probability of success (4.16)

Assuming the atoms surround a nucleus with radius r^* in a shell covering the nucleus, the number of atoms around the nucleus can be estimated using the volume of the shell divided by the volume of an atom, or

$$\text{\# atoms around nuclei} = \frac{V_{Shell}}{V_{atom}} = \frac{4p\,r^{*2}\Omega^{\frac{1}{3}}}{\Omega} = \frac{4p\,r^{*2}}{\Omega^{\frac{2}{3}}}.$$

To complete the evaluation of equation 4.16, we note that the attachment rate in one spatial dimension is approximately1/6ν, where ν is atomic vibration frequency, approximately ~10^{13}/sec, and the probability of success is equal to $e^{-\frac{Q}{kT}}$, where Q is the activation energy associated with the jump, a parameter that is usually similar to the activation energy for self diffusion.

Therefore, rate of attachment is

$$\mathrm{R} = \frac{4p\,r^{*2}}{\Omega^{\frac{2}{3}}} \cdot \frac{1}{6} n \cdot e^{-\frac{Q}{kT}} \tag{4.17}$$

Substituting $r^* = -\frac{2g}{\Delta G_v}$ and $\Delta G_v = -\Delta p \cdot f_v$ into the above equation, gives a rate of attachment

$$\mathrm{R} = \frac{8p}{3} \cdot \frac{n}{\Omega^{\frac{2}{3}}} \left(\frac{g}{f_v} \right)^2 \cdot \frac{1}{\Delta p^2} \cdot \exp\left(-\frac{Q}{kT}\right) \tag{4.18}$$

4.1.5 Nucleation Rate

Substituting the number of sites N_s, the critical free energy VG^* and rate of attachment R into equation 4.1 gives for the nucleation rate

$$\dot{N} = \frac{V}{\Omega} \cdot \frac{8p}{3} \cdot \frac{n}{\Omega^{\frac{2}{3}}} \left(\frac{g}{f_v} \right)^2 \cdot \frac{1}{\Delta p^2} \cdot \exp(-\frac{Q}{kT}) \cdot \exp\left[-\frac{16p}{3kT} \frac{g^3}{f_v^{\,2} \Delta p^2} \right] \tag{4.19}$$

Letting

$$A_1 = \frac{16p}{3kT} \cdot \frac{g^3}{f_v^{\,2}} \tag{4.20}$$

and

$$A_2 = \frac{8p}{3} \cdot \frac{n}{\Omega^{\frac{5}{3}}} \cdot \frac{g^2}{f_v^{\,2}} \cdot \exp\left(-\frac{Q}{kT} \right) \tag{4.21}$$

and using the volume of the transformed zone from equation 4.2, the nucleation rate can be written as

$$\dot{N} = V \cdot \frac{A_2}{\Delta p^2} \exp\left(-\frac{A_1}{\Delta p^2} \right) \tag{4.22}$$

Defining another material constant A_3

$$A_3 = \frac{p}{3} \cdot \left(\frac{1}{p H} \right)^{\frac{3}{2}} \cdot (1 - \cot j) \tag{4.23}$$

the transformed volume is

$$V = = \frac{p}{3} \cdot \left(\frac{P_{\max}}{p H} \right)^{\frac{3}{2}} \cdot (1 - \cot j) = \frac{p}{3} \cdot \left(\frac{1}{p H} \right)^{\frac{3}{2}} \cdot (1 - \cot j) \cdot P_{\max}^{\frac{3}{2}} = A_3 \cdot P_{\max}^{\frac{3}{2}} \tag{4.24}$$

With A_1, A_2, A_3 determined by either material properties and or indentation test conditions, the nucleation rate becomes a function of maximum indentation load P_{max} and the amount of underpressurization Δp below the equilibrium pressure p_e. according to:

$$\dot{N} = A_3 \cdot P_{\max}^{\frac{3}{2}} \cdot \frac{A_2}{\Delta p^2} \exp\left(-\frac{A_1}{\Delta p^2} \right) \tag{4.25}$$

This is the basic equation from which all subsequent analyses proceed.

4.1.6 Pop-out at Underpressurization Δp

At this point another important assumption is made. We assume that pop-out occurs only if the time needed to unload is greater than the time needed to produce one nucleus. Mathematically, this implies that

$$\dot{N} \cong \frac{1}{t_{unload}} = \frac{1}{\frac{P_{\max}}{\dot{P}}} = \frac{\dot{P}}{P_{\max}} \tag{4.26}$$

Therefore, pop-out only happens if $\dot{N} \geq \frac{\dot{P}}{P_{\max}}$,

Combining equations 4.25 and 4.26, the nucleation rate at which pop-out will take place becomes

$$\dot{N} = A_3 \cdot P_{\max}^{\frac{3}{2}} \cdot \frac{A_2}{\Delta p^2} \exp\left(-\frac{A_1}{\Delta p^2} \right) = \frac{\dot{P}}{P_{\max}} \tag{4.27}$$

or for a given loading rate $\dot{P}$

$$\dot{P} = A_2 A_3 \cdot \frac{P_{\max}^{\frac{5}{2}}}{\Delta p^2} \exp\left(-\frac{A_1}{\Delta p^2} \right) \tag{4.28}$$

Equation 4.28 can be used to solve the amount of under pressure Δp needed to induce pop-out for a given A_1, A_2, A_3, P_{max} and $\dot{P}$.

Note that Δp is a pressure term, while the indentation experimental observation yields only the load at which pop-out takes place. To apply this model using the experimental observations, it is thus necessary to relate the amount of underpressurization Δp to the corresponding pop-out load $P_{pop\text{-}out}$. In order to do this, proportional loading is assumed as shown schematically in Figure 4. 6.

According to the proportionality assumption,

$$p = a\,P \tag{4.29}$$

and the pop-out pressure and pop-out load have the following relationship

$$p_{pop-out} = a\,P_{pop-out} \tag{4.30}$$

The pressure at pop-out is

$$p_{pop-out} = p_e - \Delta p \tag{4.31}$$

Therefore, the pop-out load is

$$P_{pop-out} = \frac{p_e - \Delta p}{a} \tag{4.32}$$

At peak load, the proportionality assumption implies that

$$p_{max} = a\,P_{max} = H \tag{4.33}$$

which leads to a proportionality factor α

$$a = \frac{p_{max}}{P_{max}} = \frac{H}{P_{max}} \tag{4.34}$$

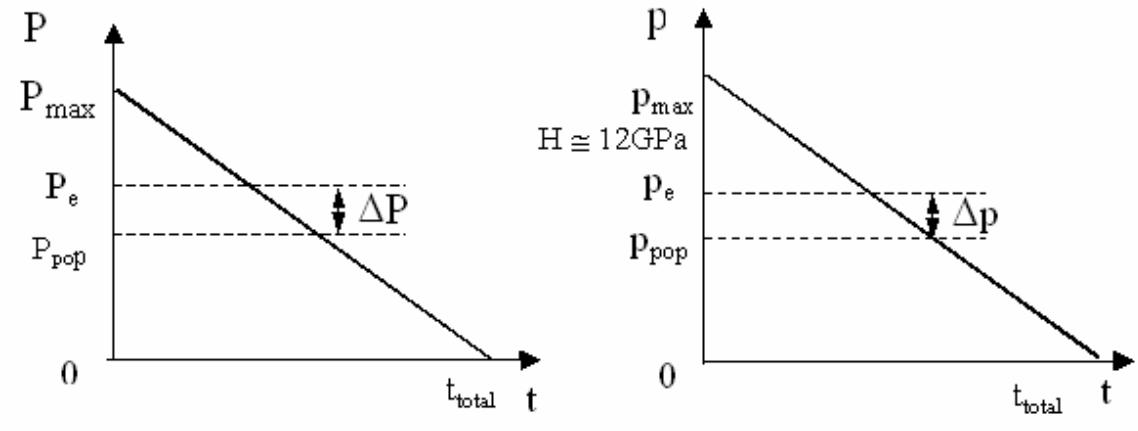

Figure 4. 6 Schematic of proportionality assumption for (a) load and (b) pressure as a function of time during indentation.

Consequently, the pop-out load can be related to the amount of under pressurization as follows:

$$P_{pop-out} = \left(\frac{p_e - \Delta p}{H} \right) \cdot P_{\max} \tag{4.35}$$

or

$$\Delta p = p_e - H \cdot \frac{P_{pop-out}}{P_{\max}} \tag{4.36}$$

4.2 Interfacial Energy and Activation Energy

4.2.1 Estimating Interfacial Energy and Activation Energy γ and Q

Although values of interfacial energy γ and activation energy Q are required to calculate pop-out load, they are essentially unknown for the transformation from high-pressure Si to the lower pressure forms. Some experimental measurements reported γ and Q for Si in various forms. Messmer and Bilello reported the surface energy γ_c for crystalline (111) Si is 1.14±0.14J/m^2 on the {111} direction, and 1.90±0.14J/m^2 on the {110} direction [53]. The interfacial energy between crystalline and liquid Si studied through bulk nucleation in laser melting experiments was determined to be 0.34±0.02J/m^2 by Stiffler et al. [54], and the interfacial energy between crystalline and a-Si determined by Bernstein et al. is in the range of 0.39 to 0.54 J/m^2, with a mean of 0.49 J/m^2 and a standard deviation of 0.05 J/m^2 [55]. The activation energy for diffusion has also been measured by various researchers, and the values for self-diffusion in Si fall into the range from 4 to 5 eV [56,57]. With these values reported in the literature, it is not clear what

values should be used for the pressure induced phase transformations. As a result, the values of γ and Q are determined by fitting the experimental pop-out data and then testing whether the resulting γ and Q are physically reasonable.

First, the 25°C indentation data at 0.5 mN/s loading/unloading rate were used to estimate values of γ and Q. We assumed that the equilibrium pressure is 12GPa, as observed in diamond anvil experiments, and that no pop-out occurs for P_{max} = 5 mN. Using equation 4.36

$$\Delta p = p_e - H \cdot \frac{P_{pop-out}}{P_{\max}}$$

for two sets of calculations at 0.5mN/s: (1) P_{max} =100 mN, $P_{pop\text{-}out}$ = 50.3 mN (refer to Table 3- 1), (2) P_{max} =5 mN, $P_{pop\text{-}out}$ = 0 mN, to solve for A_1 and A_2 yields

$$A_1 = 4.2622 \times 10^{19}\, Pa^2$$
$$A_2 = 3.8364 \times 10^{38}\, Pa^2 / m^3 / s$$

The other constants assumed in the calculations are:

k is the Boltzmann's constant, k=1.38X10^{-23}J/atom-°K

temperature is 25°C (298°K)

f_v is approximately 15%

atomic vibration frequency ν, 10^{13}/s

atomic volume for Si-II under pressure Ω, 1.42X10^{-29}m^3 [14]

Equation 4.20 can then be used to determine γ from A_1, and equation 4.21 to give Q from A_2. The resulting values are

γ = 0.1323 Pa^2 and Q= 1.321 eV

4.2.2 Sensitivity of the Estimated Interfacial Energy and Activation Energy γ and Q to the Equilibrium Pressure p_e

In the above estimation, the equilibrium pressure p_e was assumed to be 12GPa, the hardness of Si-I. Noting that the transformation pressure for the various possible crystalline forms in Si has been reported in the range roughly from 11.5 to 8GPa, Table 4- 1 lists the estimated interfacial energy and activation energy γ and Q using this model for various p_e values ranging from 12 to 8 GPa. It is clear that changing the equilibrium pressure does not produce dramatic changes in the estimated values of γ and Q.

4.2.3 Sensitivity of the Estimated Interfacial Energy and Activation Energy γ and Q vs. Unloading Rate

The values of interfacial energy and activation energy γ and Q were also estimated using data from indentation tests at all of the unloading rates. The estimations are summarized in Table 4- 2. Similar to varying the equilibrium pressure, the interfacial energy γ and the activation energy Q estimated by fitting indentation data at different unloading rates yield comparable values for γ and Q.

Based on these analyses, the values of γ and Q are not sensitive to the data used to provide the experimental fits. We thus proceed assuming $\gamma = 0.1323$ Pa^2, Q= 1.321 eV, the values from the 0.5 mN/s fit.

Table 4- 1 Estimated interfacial energy and activation energy γ and Q for various p_e.

p_e (GPa)	Gamma (J/m^2)	Q (eV)
12	0.1325	1.300
11	0.1159	1.312
10	0.0989	1.324
9	0.0810	1.334
8	0.0618	1.339

Table 4- 2 Estimated interfacial energy and activation energy γ and Q using data of various loading rates.

Unloading Rate (mN/s)	Gamma (J/m^2)	Q (eV)
0.05	0.12611747	1.367
0.5	0.13252195	1.300
2	0.14028333	1.253
5	0.16511443	1.182
20	0.18863875	1.081

4.3 Model Evaluation

4.3.1 Modeling the Influences of Indentation Rate and Peak Load

With the fixed γ and Q values from the 0.5 mN/s unloading data, the model was used to predict the behavior for all of the peak loads and loading/unloading rates. The predicted pop-out loads are compared with the experimental indentation data (see Figure 3. 26), in Figure 4. 7 and

Figure 4. 8, these figures show that the model generally follows the same trend as the experimental results. The pop-out load shows a linear relation with the varying peak load. In addition to qualitatively prediction of the trend, the model also does a reasonable job of making quantitative predictions, as evident by the comparison.

4.3.2 Modeling Temperature Effects

The same γ and Q values from the 0.5 mN/s fit were used to calculate A_1 and A_2 using equation 4.4 and 4.5 with varying temperature. Figure 4. 9 shows the model prediction on pop-out loads in the temperatures range from 0° to 100° and the experimental results from 25°C and 45°C indentation tests (data tabulated in Table 3- 2) of the 100 mN peak load indentation tests at rates of 0.5, 2, 5 and 20 mN/s. From the predictions, it is clear that: (1) the rate has a stronger effect on pop-out load at low temperature, as vthe temperature approaches 100°C, the rate effects tend to diminish; (2) as the temperature increases, the pop-out load increases, indicating a smaller driving

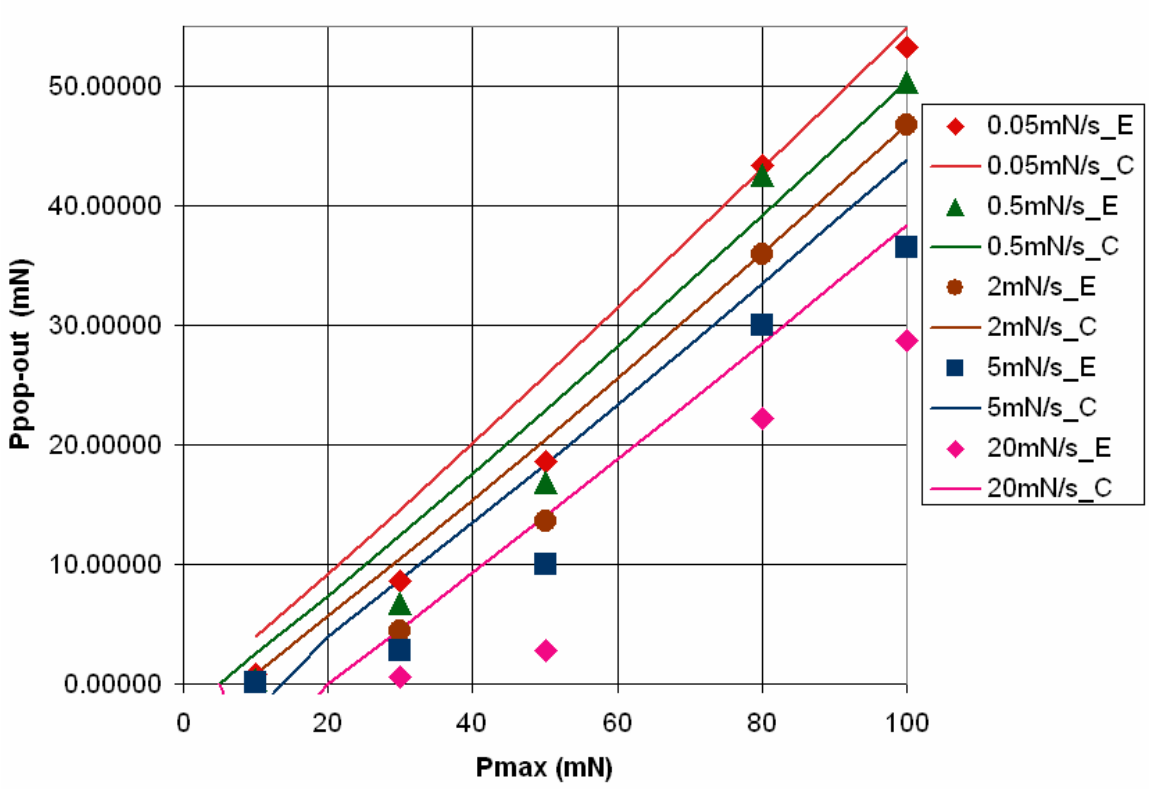

Figure 4. 7 Comparison the predicted pop-out load vs. peak load (P_{max}) using the mechanistically-based model and experimental indentation data.

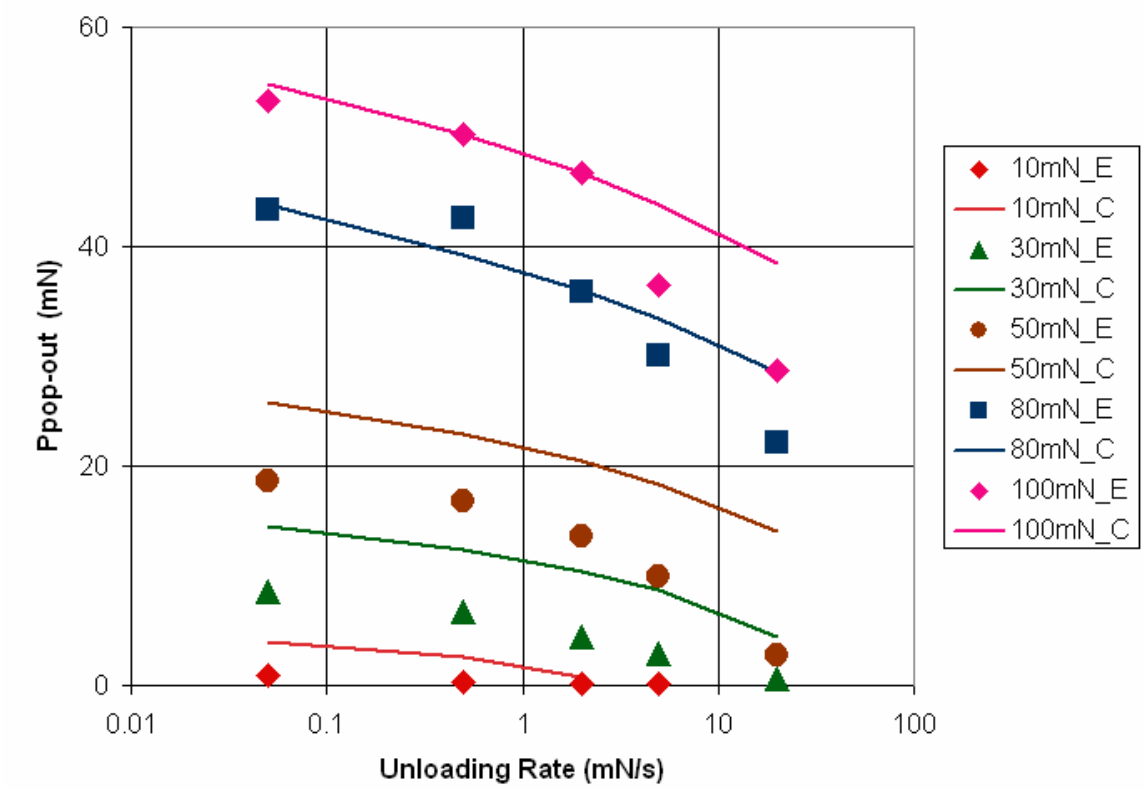

Figure 4. 8 Model predictions for pop-out vs. loading/unloading rate ($\dot{P}$) using the mechanistically-based model and experimental indentation data.

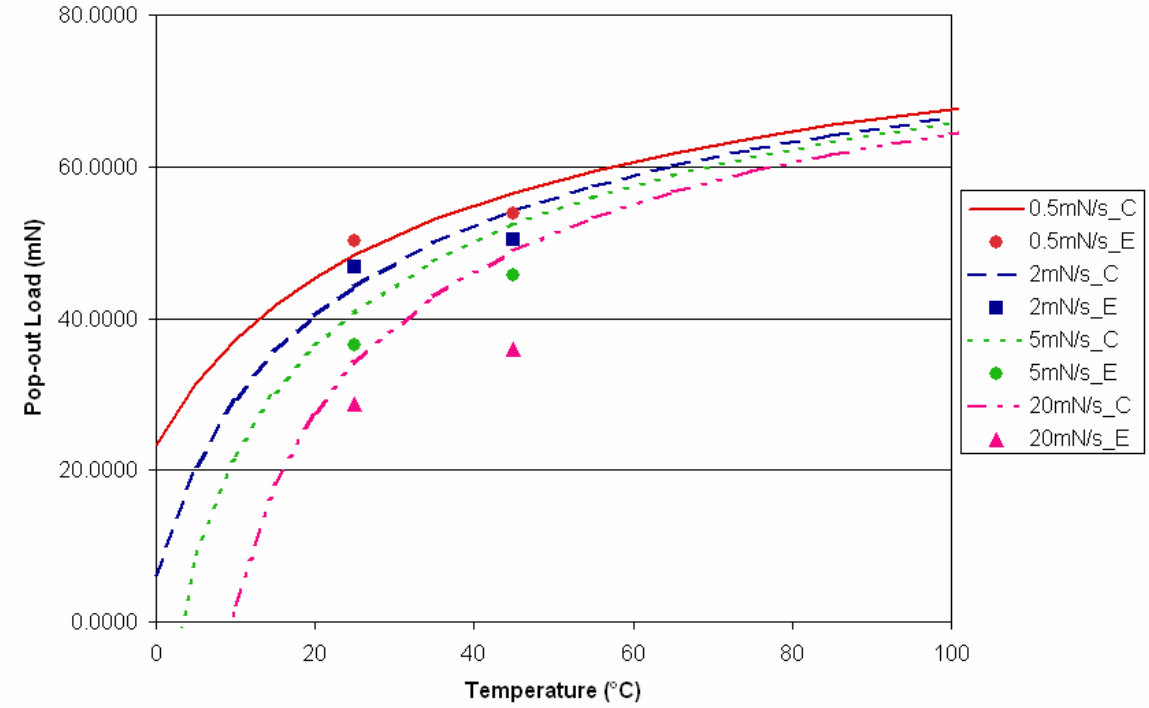

Figure 4. 9 Model predictions for pop-out loads as a function of temperature and the experimental indentation data at 25°C and 45°C.

force is needed for pop-out to occur. The experimental results from the 25°C and 45°C indentation tests are consistent with the trends predicted by the model.

4.3.3 Modeling the Step Unload Tests

The step unload tests were also used to test the model. The amount of underpressurization Δp was calculated using equation. 4.36 for all the applied percentage unloadings. The conversion from load to pressure are listed in Table 4- 3. The nucleation rates for each step unload were then calculated using equation 4.7

$$\dot{N} = A_3 \cdot P_{\max}^{\frac{3}{2}} \cdot \frac{A_2}{\Delta p^2} \exp\left(-\frac{A_1}{\Delta p^2} \right) \tag{4.36}$$

with the γ and Q values from the 0.5 mN/s data fit.

Nucleation rates for all the popped-out indentations from 100 mN and 30 mN peak load tests are plotted against the amount of unload in pressure underpressurization in Figure 4. 10. The numbers on the top of the plot designate the numbers of indentations that popped-out instantaneously following the step unload. The dashed line and solid line represent model predictions for the 100 mN and 30 mN peak loads. The two curves start out flat but then rapidly take off at approximately the underpressurization at which most of the instantaneous pop-outs were experimentally observed. The curves are shifted to the right hand side of the experimental data; however, the general trends are correct. Within the assumptions made in developing the model, it thus appears to give reasonable predictions.

Table 4- 3Amount of underpressurization Δp corresponding to unload percentage from 100 mN and 30 mN peak loads.

Unload Step Percentage	Underpressurization Δp (Pa)	
	100 mN Peak Load	30 mN Peak Load
35%	6.0E+08	Not Tested
40%	1.8E+09	Not Tested
50%	3.0E+09	3.0E+09
60%	4.2E+09	4.2E+09
65%	Not Tested	4.8E+09
70%	6.0E+09	5.4E+09
75%	Not Tested	6.0E+09
80%	7.2E+09	6.6E+09
85%	Not Tested	7.2E+09
90%	Not Tested	8.0E+09

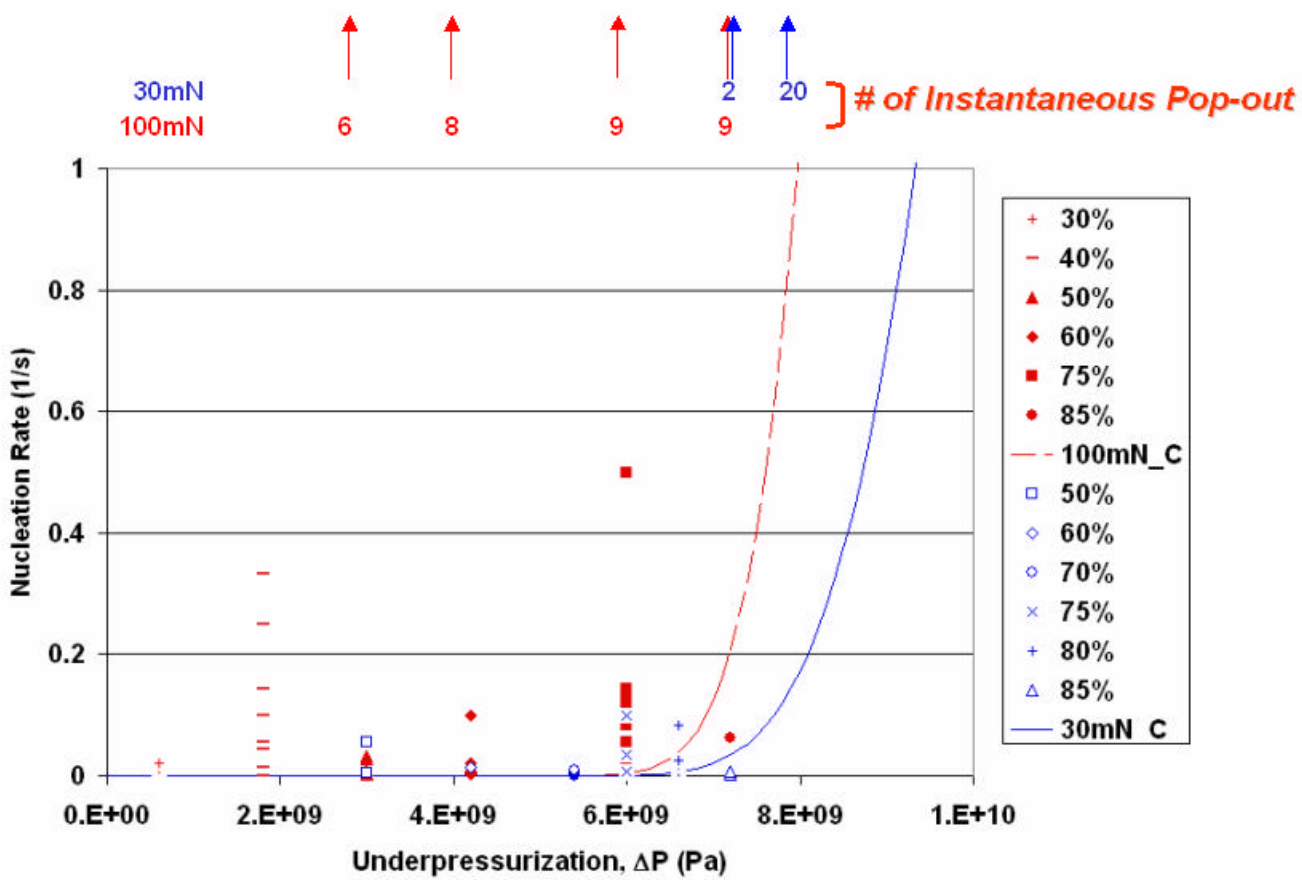

Figure 4. 10 Nucleation rates for 100 mN and 30 mN peak loads at different percentage step unload. The dots represent data point of all the pop-out indentations from the step unload tests and dashed and solid lines represent predictions using the model for 100 mN and 30 mN peak load. The number on the plot designated the number of indentations that pop-out instantaneously followed the step unload.

4.3.4 Modeling the Indenter Angle Effect

Although indenter angle effects on the pop-out behavior of Si have not been explored by systematic indentation tests, the model was applied to predict the pop-out behavior as a function of indenter angle. This modeling only involves a comparison among the 45°, 55° and 65° (Berkovich) indenters because the 35° cube-corner showed extensive extrusion of transformed material. Figure 4. 11 depicts the model prediction of the pop-out load as a function of peak load from 5 mN to 100 mN at 0.5 mN/s. The pop-out loads decrease slightly as the indenter angle gets sharper. According to equation 4.5.

$$V = \frac{p}{3} \cdot \left(\frac{P_{\max}}{pH} \right)^{\frac{3}{2}} \cdot (1 - \cot j) \qquad (4.5)$$

When φ gets smaller, the volume of the transformed zone decreases, leading to a smaller nucleation rate for a given peak load and rate; therefore, the lower pop-out load.

Prediction of the model for a peak load of 10 mN at rates spanning 3 orders of magnitudes (5, 0.5 and 0.05 mN/s) are tabulated in Table 4- 4. Comparing the predicted pop-out loads for indenters of various angles and the experimental results at 10 mN peak load for rates of 5 mN/s (Figure 3. 2), 5 mN/s (Figure 3. 21) and 5 mN/s (Figure 3. 22), it is seen that the model predictions are generally very good.

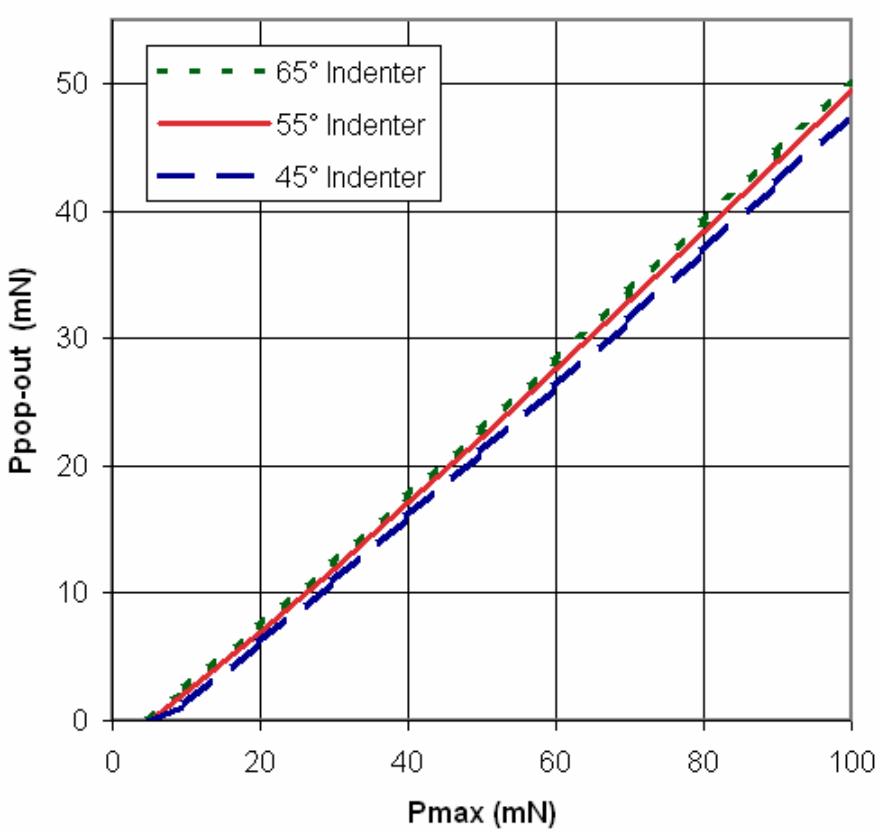

Figure 4. 11 Model prediction of the indenter angle effects on pop-out loads for peak loads ranging from 5 mN to 100 mN.

Table 4- 4 Model prediction of indenter angle effects at 10 mN peak load.

	Pop-out Load (mN)		
$\dot{P}$ (mN/s)	5	0.5	0.05
75°	0	2.72	4.04
65°	0	2.53	3.95
55°	0	2.20	3.79
45°	0	1.32	3.41

V Conclusions

Nanoindentation testing using pyramidal indenters with centerline-to-face angles varying from 35.3° to 85° has demonstrated the effects of indenter geometry, indentation peak load and loading/unloading rate, on the indentation-induced pop-out behavior (crystalline phase formation during unloading) in Si. A transition load range, from 30 to 50 mN, is defined based on the indentation study. Above the transition load, pop-out will occur regardless of unloading rate with the exception of the very sharp indenter (35° cube-corner). Unloading rates have pronounced effects on the pop-out behavior mainly at peak loads lower than the transition load range; fast unloading rates do not produce pop-out while slow rates do.

Cracking and extrusion in Si are more prevalent for indenters with sharp centerline-to-face angles. The extrusion is commonly observed for the 35° indenter at all peak loads and occasionally occurs for the 45° indenter and is believed to occur during loading with sharp indenter tips when the transformed zone exceeds the contact periphery. The indenter can no longer cap the ductile metallic transformed material, therefore, the transformed material will be extruded out. The extrusion results in smaller amount of transformed material left in the indentation to produce pop-out during pressure releasing, which explains the absence of pop-out by the sharp indenter, even at high loads.

Cross-sectional TEM studies of indentations made under various conditions, including six indenter angles, peak loads above and below the transition load range, and unloading rates ranging over several orders of magnitudes, indicate that pop-out correlates with crystalline phase formation (Si-III/Si-XII and Si-I). Indentation with no

pop-out is dominated by amorphous Si and limited amo unt of Si-I nanocrystals. Evidence of damage of the cross-sectional TEM samples by the FIB and/or the electron beam was discovered, which confuses the origin of the Si-I nanocrystals observed in the transformed zone, e.g. whether or not they were formed during unloading or by simply post-indentation damage by beam damage.

Pop-out event is highly rate and temperature dependent based on the systematic indentation study with Berkovich indenter at various peak loads and unloading rates. Temperature effects are also reflected by the comparison of indentation pop-out loads acquired from 25°C and 45°C. During unloading from the same peak load (100 mN), the load at which pop-out occurs increases with increasing temperature. Step unloading tests further prove that the phase transformation during pressure release is a highly kinetic process. To produce pop-out, it is necessary to bring the materials to a moderate peak load and/or give enough time for the transformation process to nucleate and overcome the kinetic barriers.

With the assumption of pop-out corresponds to crystalline Si-III/Si-XII phase(s) nucleating during unloading from high pressure Si-II phase, a mechanistically-based kinetic model has been developed to describe pop-out behavior in Si. By comparing the experimental results of the systematic indentation pop-out study and step unload indentation tests using Berkovich indenter, the model describes well the general pop-out behavior in Si, e.g. whether or not pop-out will occur under a given indentation condition.

REFERENCES

1 J. F. Cannon, J. Phys. Chem. Ref. Data **3,** 781-824 (1974).

2 S. I. L. Hu J. Z. , Solid State Communications **51,** 263 (1984).

3 J. Jamieson, Science **139,** 762-764 (1963).

4 L. D. M. Hu J. Z. , C. S. Meoni, I. L. Spain Phys. Rev. B. **34,** 4679-4684 (1986).

5 A. P. J. Olijnyk H., Phys. Stat. Sol. (b) **211,** 413-420 (1999).

6 A. G. J. Crain J., Maclean J. R., Politz R. O., Hatton P. D., Pawley G. S., Physical Review B **50,** 13043-13046 (1994).

7 M. J. R. Piltz R. O., Clark S. J., Ackland G. J., HattonP.D., Crain J., Physical Review B **52,** 4072-4085 (1995).

8 R. A. Mujica A., Munoz A., Needs R. J., Review of Modern Physics **75,** 863-912 (2003).

9 C. M. L. Yin M.T., Phys. Rev. B. **26,** 5668 (1982).

10 K. J. S. Wentorf R. H. Jr., Science **25,** 338 (1963).

11 R. S. H. Kasper J.S., Acta crystallographica **17,** 752 (1964).

12 M. R. M. Biswas R., Needs R. J., Nielsen O. H., Phys. Rev. B.**,** 3210 (1984).

13 C. M. Pfrommer B.G., Louie S. G., Cohen M. L., Phys. Rev. B. **56,** 6662 (1997).

14 R. Hull**,** 104-107 (1999).

15 W. M. Deb SK, Somayazulu M, McMillan PF., Nnature **414,** 528-531 (2004).

16 D. D. Durandurdu M, Phys. Rev. B. **67,** 212101 (2003).

17 M. Y. V. Gridneva I. V.., Trefilov V. I. , Phys. Stat. Sol. (a) **9,** 177-182 (1972).

18 T. D. Gerk AP, Nature **271,** 732-733 (1978).

19 D. H. Minomura S, J. Appl. Chem. Solids. **23,** 451-456 (1962).

20 R. A. Gupta MC, J. Appl. Phys. **51,** 1072-1075 (1980).

21 Gilman J., JMR **7,** 535-538 (1992).

22 H. R. Pethica JB, Oliver WC, Philos. Mag A. **48,** 593-606 (1983).

23 O. W. C. Pharr G. M., R. F. Cook, P.D. Kirchner, M. C. Kroll, T. R. Dinger, D. R. Clarke, JMR **7,** 961-972 (1992).

24 O. W. C. Pharr G. M., D.S. Harding, JMR **6,** 1129-1130 (1991).

25 O. W. C. Pharr G. M., D. R. Clarke, Journal of electronic materials **19,** 881-887 (1990).

26 O. W. C. Pharr G. M., D. R. Clarke, Scripta Metallurgica **23,** 1949-1952 (1989).

27 D. v. H. Mann A. B., J. B. Pethica, P. Bowes,T. P. Weihs, J. Mater. Res. **15,** 1754-1758 (2000).

28 Y. G. G. Kailer A., K. G. Nickel, J. Appl. Phys. **81,** 3057-3063 (1997).

29 D. v. H. Mann A. B., J. B. Pethica, P. Bowes,T. P. Weihs, Phylosophical Magzine A **82,** 1921-1929 (2002).

30 Y. G. Domnich V., S. Dub, Applied physics letters **76,** 2214-2216 (2000).

31 Y. G. Domnich V., in *Experiental Methods in the Physical Science* (2001).

32 Y. G. Domnich V., Demensional Novel Electronic Materials**,** 291-302 (2001).

33 F. C. Buscher H Zi.J., Ludwig W., Zhang K., Xie X., Applied physics letters**,** 200 (1996).

34 R. D. HillMJ, J. Mater. Sci. **9,** 1569-1576 (1974).

35 M. C. K. Clarke D. R., P. D. Krichner, R. F. Cool, Physics Review Letter **60,** 2156-2159 (1988).

36 X. Y. B. Wu Y. Q., JMR **14,** 682 (1999).

37 Y. X. Y. Wu Y. Q., Xu Y. B., Acta Mater **47,** 2431 (1999).

38 W. C. O. Page T. F., C. J. Mchargue, J. Mater. Res. **7,** 450 (1992).

39 M. J. Callahan D. L., JMR **7,** 1614-1617 (1992).

40 D. V. Ge D., Gogotsi Y., J. of applied physics **93,** 2418-2423 (2003).

41 J. S. W. Bradby J. E., J. Wong-Leung, MSwain M. V., Munroe P., Applied physics letters **77,** 3749-3751 (2000).

42 J. S. W. Bradby J. E., J. Wong-Leung, M. V. Swain, P. Munroe, J. Mater. Res. **16,** 1500-1507 (2001).

43 L. C. Z. Zarudi I., Tribology international **32,** 701-712 (2000).

44 L. C. Z. Zarudi I., , Zuo J., Vodenitcharova T., JMR **19,** 332-337 (2004).

45 Z. I. Zhang L. C, International journal of mechanical sciences **43,** 1985-1996 (2001).

46 L. C. Z. Zarudi I., M. V. Swain, Applied physics letters **82,** 1027-1029 (2003).

47 L. C. Z. Zarudi I., Applied physics letters **82,** 874-876 (2003).

48 J. M. M.-A. Lloyd S. J., W. J. Clegg, J. Mater. Res. **16,** 3347-3350 (2001).

49 A. S. Saka H., M, Suganuma, Suprija, Philosophical Magazine A **82,** 1971-1981 (2002).

50 P. G. M. Oliver W. C., J. Mater. Res. **19,** 3-20 (2004).

51 P. G. M. Oliver W. C., J. Mater. Res. **7,** 1564-1583 (1992).

52 Y. G. G. Kailer A., K. G. Nickel, J. of Raman Spectroscopy **30,** 393-346 (1999).

53 B. J. C. Messmer C., j. Appl. pHYS. **52,** 4623-4629 (1981).

54 T. M. O. Stiffler S. R., Peercy, Phys. Rev. Letters **60,** 2519-2522 (1988).

55 A. M. J. Bernstein N., Kaxiras E., Phys. Rev. B. **58,** 4579-4583 (1998).

56 E. E. H. Bracht H. , r. Clark-Phelps, Physical Review letters **81,** 393-397 (1998).

57 G. P. B. Ural Ant, Plummer J. D., Physical review lettters **83,** 3454-3457 (1999).

VITA

Songqing Wen was born in China in 1971. She was raised in Shenyang, China. After graduated from Shenyang No. 4 High School, Shenyang, China in 1989, she attended Shenyang Polytechnic University and completed her undergraduate study in the Department of Materials Science and Engineering in 1993. She worked as a materials engineer for five years before coming to the University of Tennessee, Knoxville in 1998, where she first worked as visiting scholar and later received an M.S. degree in Materials Science and Engineering in 2001. In 2002, she started to pursue a doctorate in materials science and engineering. She received a Ph.D degree under the guidance of Professor George Pharr in 2006.